SYNTHESIS OF DUAL OFFSET GREGORIAN REFLECTOR ANTENNAS WITH VERY LOW CROSS POLARIZATION UNDER PRACTICAL CONSTRAINTS FOR MASS PRODUCTION

by

Marco A.B. Terada

Dissertation submitted to the Graduate Faculty of
Virginia Polytechnic Institute and State University
in partial fulfillment of the requirements for the degree of
Doctor of Philosophy in Electrical Engineering

APPROVED:

Dr. Warren L. Stutzman, Chairman

Dr. William A. Davis

Dr. Timothy Pratt

Dr. Ahmad Safaai-Jazi

Dr. Max Gunzburger

June, 1995
Blacksburg, Virginia

SYNTHESIS OF DUAL OFFSET GREGORIAN REFLECTOR ANTENNAS WITH VERY LOW CROSS POLARIZATION UNDER PRACTICAL CONSTRAINTS FOR MASS PRODUCTION

by

Marco A.B. Terada

Dr. Warren L. Stutzman, Chairman
Department of Electrical Engineering
Virginia Polytechnic Institute and State University

(ABSTRACT)

This dissertation starts with a complete survey of the depolarization characteristics of axisymmetric and offset reflector antennas. Single and dual reflector configurations are considered. Cross polarization (XPOL) and beam squint are examined in detail. Although many of the phenomena are known, they are interpreted and explained in new ways and presented in a single coherent treatment.

It is shown that single offset reflector antennas are limited in performance by high XPOL. A cost effective way to improve the performance of an existing offset prime-focus reflector is to add a subreflector, forming a dual offset reflector system with very low cross polarization (e.g., -35 dB). The motivation to use a specified main reflector often arises from a desire to use an existing mold which is usually very expensive. Within this context, procedures to upgrade existing reflector configurations are developed and presented.

In addition, the influence of XPOL effects caused by low-cost, conventional feeds is analyzed in detail. A model for predicting the total system XPOL due to the reflectors and feed is discussed. Various techniques to reduce feed XPOL effects are introduced. Also, practical manufacturing constraints for large scale production are imposed on low-cost dual offset Gregorian reflector antennas. In particular, a design for adequate clearance between the bottom of the main reflector and feed axis is addressed. These constraints are not taken into account by other design procedures and are not addressed in the open literature.

All innovative design algorithms developed in this dissertation were implemented as numerical codes referred to as DORA (Dual Offset Reflector Antenna Synthesis Package). DORA is a complete suite of codes for the synthesis of non-conventional, low-cost dual offset Gregorian reflector antennas with very low cross polarization. Several practical examples are discussed, including a performance assessment of the largest steerable reflector in the world, the Green Bank Radio Telescope located in Green Bank, West Virginia.

Finally, an overview of the various analytical and numerical methods employed in the analysis of reflector antennas is presented in the appendices. The philosophical differences between the methods are highlighted. In particular, the physical optics approach and the Jacobi-Bessel series expansion method are described in detail. The combination of these two formulations results in one of the most accurate and efficient numerical tools in the analysis of reflector antennas. This is shown with the developed code PRAC, Parabolic Reflector Analysis Code. The effectiveness of PRAC is confirmed through extensive comparisons with measured data and results obtained from the literature and with the commercial code GRASP7. Most of the reflector antenna configurations obtained from the procedures developed in this dissertation are analyzed with PRAC and/or GRASP7.

Acknowledgment

Although only six names appear on the cover of this work, many other people have also contributed for its development. An attempt to list all of them would certainly leave a few forgotten.

Therefore, I prefer to thank in a general way everyone who made this work possible, including students, faculty and staff.

In particular, I would like to thank my family for the understanding and support.

Contents

List of Tables

List of Figures

Chapter 1

Introduction

Polarization is a basic characteristic of an electromagnetic wave and describes the motion of the electric field vector at a fixed point in space as a function of time. The polarization of an antenna is the polarization of its radiated wave when operating in the transmitting mode. Generally, the polarization of any antenna system can be decomposed into two orthogonal components in the far-field, referred to as co-polarization and cross polarization, respectively. In the particular case of reflector antenna systems, the co-polarization is usually taken to be the one presented by the feed antenna employed to illuminate the reflector(s). As a consequence, the cross polarization is orthogonal to the feed antenna main polarization. This agrees with Ludwig's third definition of cross polarization [1] and is the one employed in the present study. Cross polarization level (XPOL) is defined quantitatively as the ratio of the peak in the cross-polarized radiation pattern to the peak value of the co-polarized pattern (i.e., the main beam peak), usually expressed in dB.

Reflector antennas have been used in many applications requiring high gain at UHF frequencies and above. Through the past few decades designs have evolved through several forms for the purpose of improving electrical performance and/or

simplifying the mechanical structure; see Fig. 1.1. Performance parameters that are of prime interest are aperture efficiency, sidelobe level, and, more recently, cross polarization level. The most basic form is the single axisymmetric parabolic reflector shown in Fig. 1.1(a), which is still in widespread use primarily at low frequencies and for low-cost applications. Large reflectors frequently use an axisymmetric dual reflector system with a parabolic main reflector as shown in Fig. 1.1(b). The subreflectors are hyperbolic (Cassegrain system) or elliptical (Gregorian system). These systems offer a shorter transmission line (or waveguide) run to the feed antenna. They are often used for earth terminal antennas in satellite communication networks because of the inherent low noise due to limited noise introduced by spillover beyond the subreflector that is directed to cold sky rather than hot earth in the single reflector case.

Axisymmetric single and dual reflectors suffer from aperture blockage due to the presence of feed/subreflector and supporting mechanical structures in front of the main reflector aperture. This problem is solved by using an offset system with a main reflector that is a section of a parent reflector, normally a paraboloid of revolution, as shown in Figs. 1.1(c) and 1.1(d). The offset configuration allows even a relatively large electronics package to be placed near the feed horn without loss of performance.

One of the largest markets for offset reflector antennas is for satellite communication earth terminals and, in particular, for Very Small Aperture Terminals (VSATs). VSAT systems are used for large retail chains such as Walmart and Kmart, banks, and car dealers such as GM and Chrysler. The VSAT market is expected to grow at a rate of 20% per year [2]. Currently VSAT systems use C-band and Ku-band frequencies, with Ku-band being the most popular choice. Recently Ka-band has been pioneered by the experimental Advanced Communications Technology Satellite

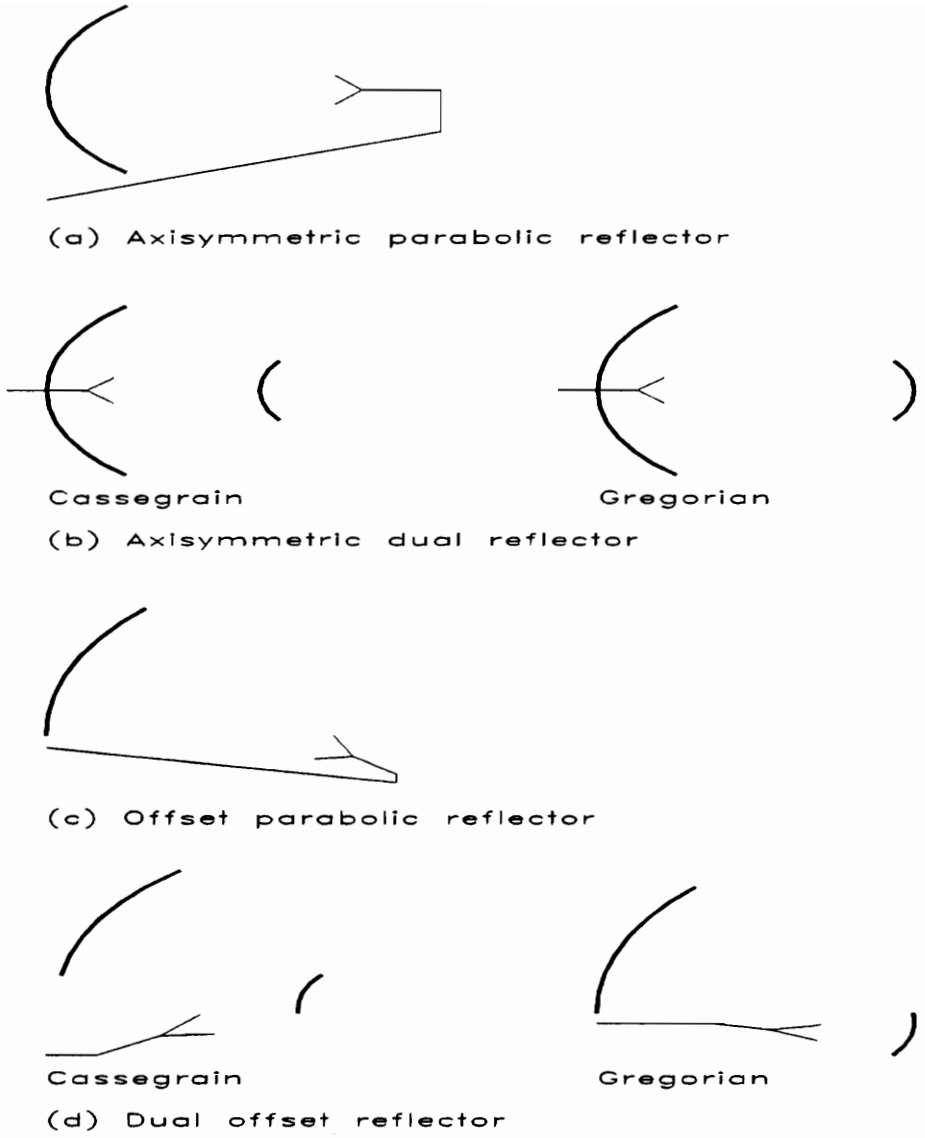

Figure 1.1. The evolution of reflector antenna systems. The main reflectors are parabolic. In addition, cases (b) and (d) also have forms that use non-parabolic ("shaped") main reflectors.

(ACTS). VSAT systems will experience even larger growth when operational Ka-band satellites become available. However, the inherently asymmetric geometry of the offset, single parabolic reflector leads to high cross polarization level (XPOL) [3, 4]. Increased XPOL degrades the isolation between orthogonally polarized channels in frequency re-use systems.

There are a few procedures available to reduce XPOL in single offset reflectors [5, 6]. However, they require the design and manufacturing of special feeds [5], lenses [6] and/or shaped reflectors [6]. This can lead to costly design and production, especially for wideband systems. A cost effective way to improve the performance of an existing offset prime-focus reflector is to add a subreflector, forming a dual reflector system with very low cross polarization. In recent years dual offset reflector systems have been used to achieve low cross polarization [3]. The Green Bank Radio Telescope, for example, can be operated as a single offset system or as a dual offset Gregorian configuration optimized for low XPOL [7, 8].

Both axisymmetric and offset dual reflector systems of Figs. 1.1(b) and 1.1(d) can be shaped to increase aperture efficiency. The axisymmetric, dual shaped reflector was introduced in the 1960's [9] and is popular for large earth station antennas. The offset, dual shaped reflector has a demonstrated aperture efficiency of 84.9% [10] and will gain popularity in the future.

This dissertation focuses on the use of sophisticated low cross-polarized reflector antenna systems applied to low-cost applications. In particular, we consider single and dual offset systems with a parabolic main reflector. This permits the use of the same main reflector in both single and dual reflector configurations, greatly reducing cost. The motivation to use a specified main reflector often arises from a desire to use an existing mold which is usually very expensive. In the present work,

this problem is referred to as reflector system upgrading. Methods for upgrading existing prime-focus reflector systems in a general and systematic way have not been published.

Since the proposed problem is based on a practical setting, cross polarization effects of conventional, low-cost feeds are accounted for in the analysis. The influence of feed XPOL on the total reflector system XPOL is investigated in detail. Many applications impose limitations on system XPOL. For example, the EUTELSAT specification for VSAT communications is -35 dB within the -1 dB contour of the main beam [11]. In the present work, an effort is made to achieve -35 dB XPOL over a broad pattern region (i.e., main beam and near-in sidelobes), thus satisfying the EUTELSAT requirement. Single offset reflectors illuminated by conventional feeds usually present a XPOL level much higher than -35 dB [4].

In addition, we investigate practical manufacturing constraints for the mass production of low-cost dual offset Gregorian reflector antennas. In particular, the problem of obtaining clearance between the feed axis and the bottom of the main reflector is analyzed in detail. This allows access to the feed antenna with a straight section of waveguide, thus reducing the complexity and cost of the manufacturing process. The Gregorian configuration is selected based on the fact that our analysis includes the use of just fully offset paraboloids as main reflectors (i.e., the bottom of the reflector just touches its axis of symmetry). These reflectors are widely employed in commercial applications. A Cassegrain configuration is more appropriate for main reflectors that are not just fully offset; see Section 3.2 for further information. However, this is not a restriction since all derivations presented in this work are valid for main reflectors with any degree of offset. An example of a dual offset Gregorian configuration employing a main reflector that is not just fully offset is the Green Bank Telescope [7, 8]. The Gregorian configuration permits the main reflector to be

used as a prime-focus offset system without the need of removing the subreflector. This is not possible with a Cassegrain configuration [7]. The Green Bank Telescope Reflector Antenna is discussed in detail in Section 5.5.

Chapter 2 presents a complete survey of the various depolarization properties of single and dual reflector antennas. Although many of the results are known, they are interpreted in new ways and presented in a single coherent treatment. An in-depth understanding of the cross polarization behavior of offset reflector antennas is essential for achieving effective designs, as it will be shown throughout the dissertation.

The motivation, requirements, and design methodology to upgrade reflector systems are discussed in Chapter 3. The influence of feed XPOL on system XPOL is addressed in Chapter 4, including a simple prediction model and a new technique to reduce XPOL effects of a certain class of feed antennas. Chapter 5 introduces original procedures for reducing system XPOL while enforcing practical constraints for low-cost production of dual offset Gregorian reflector antennas.

The problem of shaping subreflectors for system XPOL reduction is addressed in Chapter 6. The shaping algorithm is based on the gradient method, which has never been used in the fashion described in this work. Chapter 7 presents two original ideas that can be used as future dissertation topics. The major conclusions derived from this work are summarized in Chapter 8 and all references are listed in Chapter 9.

A compendium of various methods for the analysis of reflector antennas is presented in a historical fashion in Appendix A (Chapter 10). In particular, the physical optics approximation [12] and the analytically sophisticated Jacobi-Bessel series expansion method [13, 14] are discussed in detail. These formulations were implemented numerically by the author in the Parabolic Reflector Analysis Code,

PRAC, which is described in Appendix B (Chapter 11). The accuracy of PRAC is confirmed by extensive comparisons with measured data and results available in the literature or obtained from other codes. Most of the reflector antenna configurations obtained from the procedures developed in this dissertation are analyzed with PRAC and/or the commercial code GRASP7 (General Reflector Antenna Synthesis Package) [15].

Finally, the Mizugutch condition [16] is derived in Appendix C (Chapter 12). Enforcement of this condition assures minimum XPOL in dual offset reflector antennas illuminated by a purely polarized feed. The Mizugutch condition is used as the starting point in most of the procedures developed in this dissertation for the synthesis of dual offset reflector antennas.

Chapter 2

Depolarization Properties of Reflector Antennas

2.1 Introduction

This chapter combines results from a computational study with previously reported properties of single axisymmetric and offset parabolic reflectors into a complete explanation of cross polarization (XPOL) and beam squint phenomena of reflector antennas. Both linearly polarized (LP) and circularly polarized (CP) feeds are examined. This permits a comparison between the polarization and beam pointing characteristics of most single parabolic reflector configurations. Emphasis is given to explaining the absence of XPOL and the mechanism for generating beam squint in offset parabolic reflectors illuminated by a CP feed. Although many of the phenomena are known, they are explained in new ways and presented in a single coherent treatment. An in-depth understanding of the XPOL behavior of offset reflector antennas is necessary for achieving effective reflector antenna designs. In addition, the

behavior of gain, sidelobe level and XPOL as a function of feed pointing angle is investigated in detail. Finally, the results for polarization and beam squint characteristics of prime-focus offset parabolic reflector antennas are extended to dual offset configurations.

2.2 The Study Configuration

2.2.1 Single Paraboloid Geometry

The geometry for a general offset parabolic reflector is shown in Fig. 2.1 and the associated symbols are defined in Table 2.1. In this chapter, with the exception of Section 2.3.3, the feed pointing angle ψ_f is fixed such that

$$\psi_f = \psi_B \tag{2.1}$$

where ψ_B is the angle which bisects the angle that subtends the reflector; see Table 2.1 for further information. An axisymmetric parabolic reflector is a special case where

$$D = D_p \tag{2.2}$$
$$H = 0$$

which leads to

$$\psi_f = \psi_B = 0^\circ \tag{2.3}$$

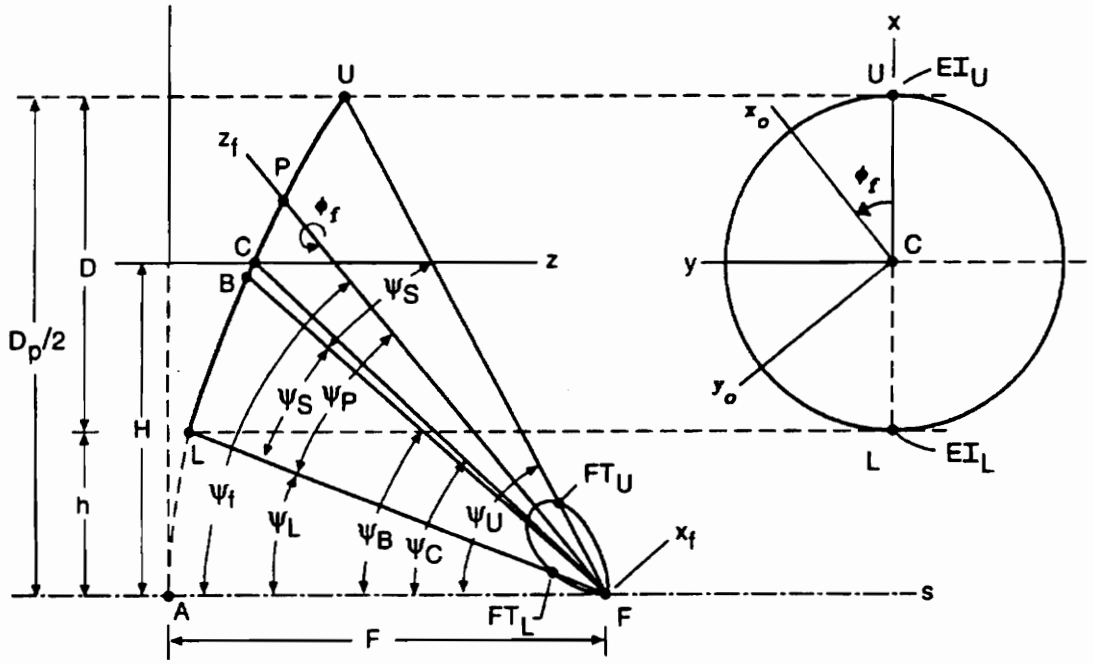

Figure 2.1. Geometry for the offset parabolic reflector. See Table 2.1 for definitions of parameters.

Table 2.1.

Definitions of Symbols

D = Diameter of the projected circular aperture of the parabolic main reflector.

D_p = Diameter of the projected circular aperture of the parent paraboloid.

h = Offset distance = Distance from the axis of symmetry (s) to the lower reflector edge.

H = Offset of reflector center = Distance from axis of symmetry (s) to center of reflector = $D/2 + h$.

F = Paraboloid focal length.

F/D_p = "F/D" of parent paraboloid.

ψ_f = Angle of feed antenna pattern peak relative to reflector axis of symmetry (s); the feed is directed toward point P.

ψ_B = Value of ψ_f which bisects the reflector subtended angle; i.e. feed is aimed at point B ($\psi_f = \psi_B$) and $\psi_B = \psi_S + \psi_L$.

ψ_C = Value of ψ_f when the feed is aimed at the reflector point C corresponding to the aperture center.

ψ_E = Value of ψ_f that yields an equal edge illumination.

ψ_P = Angle from lower edge of dish to feed pointing direction; $\psi_f = \psi_L + \psi_P$.

ψ_S = Half of the angle subtended by the reflector as viewed from the focal point.

Table 2.1. **(cont.)**

Point A = Apex of parent reflector.

Point B = Point on main reflector which bisects subtended angle viewed from focal point.

Point C = Point on main reflector which projects to the center of the projected aperture.

Point P = Point on main reflector corresponding to the ray arising from the peak of the feed pattern; P is in the xz-plane.

Point F = Focal point.

FT = Feed edge taper; FT ≥ 0.

SPL = Spherical spreading loss; SPL ≥ 0.

EI = Edge illumination; EI = -(FT + SPL).

Coordinate system $\{x,y,z\}$ = Reflector coordinate system

Coordinate system $\{x_f,y_f,z_f\}$ = Feed coordinate system

Coordinate system $\{x_o,y_o,z_o\}$ = Output coordinate system; the far-field patterns are expressed in this coordinate system. The x_o-axis is aligned with the projection of the feed polarization in the aperture.

Angle ϕ_f = Rotation of feed (clockwise when looking at it) and output coordinate system (counter-clockwise). For $\phi_f = 0°$, the LP feed is x_f-polarized.

For the just fully offset case

$$D = D_p/2 \tag{2.4}$$
$$H = D/2$$

and the feed pointing angle ψ_f is given by [12]

$$\psi_f = \psi_B = \psi_U/2 = \tan^{-1}\left[\frac{1}{4(F/D_p)}\right] \tag{2.5}$$

2.2.2 Balanced and Unbalanced Feeds

The electrical performance of a reflector antenna cannot be determined without a proper description of the feed antenna employed to illuminate the reflector(s). The radiation pattern of an idealized feed with a fixed phase center can be described as [3]

$$\vec{E}_f(\vec{r}_f) = \frac{e^{-\jmath\beta r_f}}{r_f}[\hat{\theta}_f\ C_\theta(\theta_f)\cos\phi_f - \hat{\phi}_f\ C_\phi(\theta_f)\sin\phi_f] \tag{2.6}$$

where $C_\theta(\theta_f)$ and $C_\phi(\theta_f)$ denote the feed pattern cuts in the E-plane ($\phi = 0°$) and H-plane ($\phi = 90°$), respectively. This is, most of the time, all that is known. It is assumed that the feed is purely linearly polarized in the x_f-direction. A y_f-polarized feed pattern may be obtained from (2.6) by replacing the argument ϕ_f with $\phi_f - \pi/2$. In addition, a circularly polarized feed can be obtained by combining the x_f-polarized feed pattern in (2.6) with a y_f-polarized feed pattern that is in phase quadrature (i.e., multiplied by a factor of $\jmath$) [14, 17].

The feed is defined "balanced" (i.e., the primary radiation pattern is symmetric in ϕ_f) for $C_\theta(\theta_f) = C_\phi(\theta_f)$. In that case, (2.6) reduces to

$$\vec{E}_f(\vec{r}_f) = \frac{e^{-j\beta r_f}}{r_f} C(\theta_f) [\hat{\theta}_f \cos\phi_f - \hat{\phi}_f \sin\phi_f] \tag{2.7}$$

Examples of balanced feeds are given below [15, 18]:

$$C(\theta_f) = 1 + \cos(\theta_f) \qquad \text{Huygen's source,} \tag{2.8}$$

$$C(\theta_f) = \cos^q(\theta_f) \qquad \text{Cos}^q \text{ feed model} \tag{2.9}$$

and

$$C(\theta_f) = G_0 10^{\left[\frac{A_l}{20}(\theta_f/\theta_{f0})^2\right]} \qquad \text{Gaussian feed model} \tag{2.10}$$

where A_l is the amplitude level in dB at $\theta_f = \theta_{f0}$. The gain normalization constant G_0 is found by numerical integration of (2.10) [15]. The $\cos^q$ feed model given in (2.9) is used in the Parabolic Reflector Analysis Code, PRAC, described in Appendices A and B (Chapters 10 and 11). The current version of PRAC does not handle CP feeds and cannot generate uv-contour plots directly and therefore is not used in this chapter.

The physical optics portion of the commercial code GRASP7 [15] was used to generate all far-field pattern cuts and uv-contour plots presented in this chapter. The physical optics formulation applied to the analysis of reflector antennas is explained

in detail in Appendix A (Chapter 10). This approach is reportedly more accurate than other methods (e.g., geometrical optics), especially for the determination of the cross-polarized fields [19]. Since they are of main importance for the present study, physical optics was employed by GRASP7 and PRAC in all computer simulations presented in this dissertation. Furthermore, only the main lobe and near-in sidelobes are considered, since the method fails to determine the far-out sidelobes and back-lobe region accurately. A combination of physical optics and approaches based on diffraction theory is preferable in those situations [12, 20, 21, 22]. However, this was not performed in the present study since the pattern region close to boresight (i.e., main lobe and near-in sidelobes) is, most of the time, the region of interest when analyzing high-gain antennas, such as the reflector antennas considered here.

In all computer simulations presented in this chapter, the feed is modeled using the symmetric ("balanced") Gaussian radiation pattern of (2.10) with a 10-dB beamwidth of 70° shown in Fig. 2.2. The feed polarization can be LP or CP and the feed can be located on or off the paraboloid focal point. We also comment on how an unbalanced feed (i.e., the primary radiation pattern is not symmetric in ϕ_f) affects the electrical performance of reflector antennas.

2.3 Cross Polarization in Single Reflector Configurations

2.3.1 Axisymmetric Reflectors

Baseline axisymmetric and offset reflector configurations were selected to facilitate performance comparisons; the configuration parameters are listed in

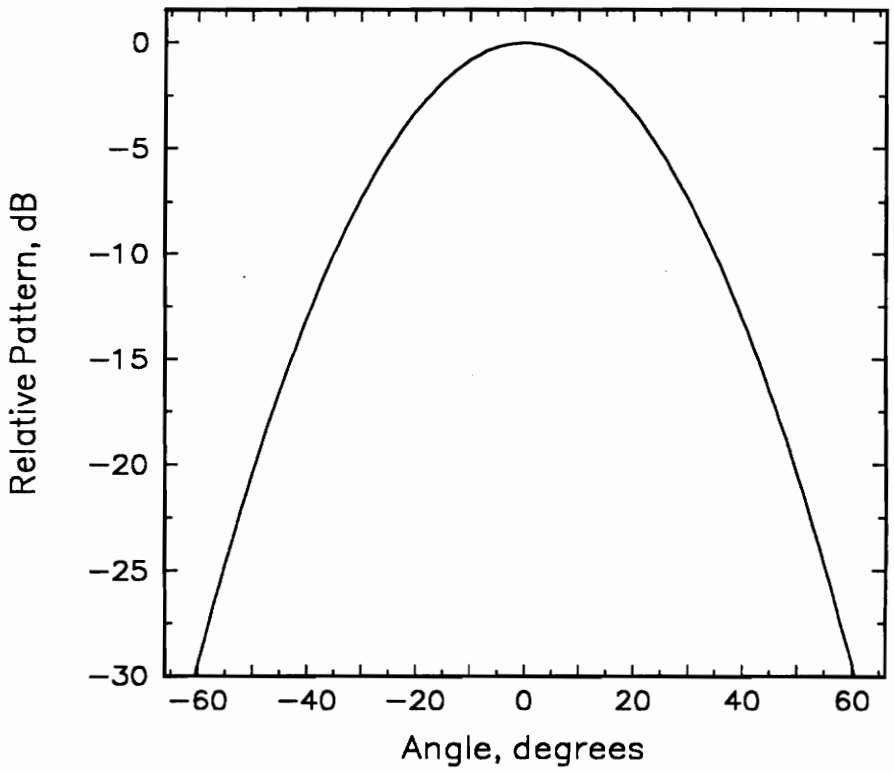

Figure 2.2. Gaussian feed pattern.

Table 2.2. We first examine the axisymmetric reflector of Table 2.2 using a balanced feed with the Gaussian pattern of Fig. 2.2 and purely linearly polarized along the x_f-axis; that is $\phi_f = 0°$. The computed level of XPOL displayed in Fig. 2.3 is very low (maximum of -65.35 dB). Typically, the feed assembly and supports (not considered here) will create more XPOL than this. Therefore, reflector-induced XPOL in axisymmetric reflectors illuminated by balanced feeds is often negligible. According to Fig. 2.3, the XPOL peaks are all located in the 45° planes. The gain G is 48.62 dBi and the half-power beamwidth HP is 0.72° for all ϕ. The computed performance values are summarized in Table 2.3.

Next the LP feed is rotated so that $\phi_f = 30°$. This is done in order to investigate the XPOL arising from a CP feed by examining instantaneous electric fields. Figure 2.4 shows that the generated far-field XPOL contour plot is also rotated by 30° as expected. Note that since the output coordinate system $x_o y_o z_o$ has been rotated by 30°, the x-axis (of the antenna coordinate system) is no longer coincident with the x_o-axis (radiation is x_o-polarized). The output coordinate system $x_o y_o z_o$ is rotated in order to have the projections of $\hat{x}_f$ and $\hat{y}_f$ (i.e., $\hat{x}_o$ and $\hat{y}_o$) be the co and cross polarizations directions, respectively. In a measurement setup this is equivalent to rotating the transmitting antenna to align its main polarization with the polarization of the antenna under test. Although not shown in Fig. 2.4, the co-polarized pattern plot is the same as the co-polarized pattern plot of Fig. 2.3.

Figure 2.5 shows the aperture fields for an axisymmetric parabolic reflector fed by a vertically polarized dipole [23]. It is interesting to examine the electric field vector components in the reflector aperture. It is easy to see that the XPOL peaks are located at the 45° planes. This applies to the reflector far-field also, but XPOL is canceled in the principal planes. We can state then that the more "balanced" is the feed, the lower is the XPOL level on the aperture plane. Thus, we expect high

Table 2.2.

Baseline Configurations

(a) Main Reflector Configuration	Axisymmetric	Offset
Shape	Paraboloid	Paraboloid
Projected diameter (D), λ	171.0	85.5
Parent reflector diameter (D_p), λ	171.0	171.0
Focal length (F)	0.3 D_p	0.3 D_p
Offset of reflector center (H), λ	0.0	42.75
(b) Feed Configuration (on-focus)		
Polarization	Linear (x_f)	Linear (x_f)
Pattern shape	Gaussian	Gaussian
Gain (G_f), dBi	14.04	14.04
10-dB beamwidth, degrees	70.0	70.0
Feed pointing angle (ψ_f), degrees	0.0	39.81
Edge Illum. (Lower,Upper), dB	(-56.8,-56.8)	(-13.0,-17.6)

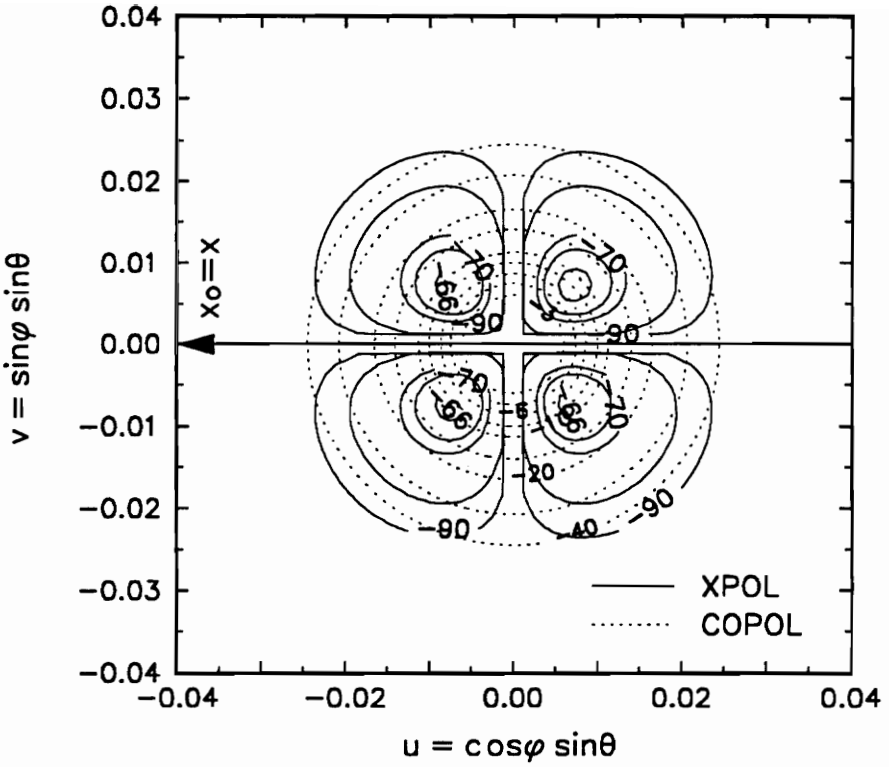

Figure 2.3. Contour plots (dB) of the computed co- (dashed curves) and cross-polarized (solid curves) patterns of the 171-λ diameter axisymmetric parabolic reflector specified in Table 2.2. The balanced feed is linearly polarized in the x_f-direction ($\phi_f = 0°$).

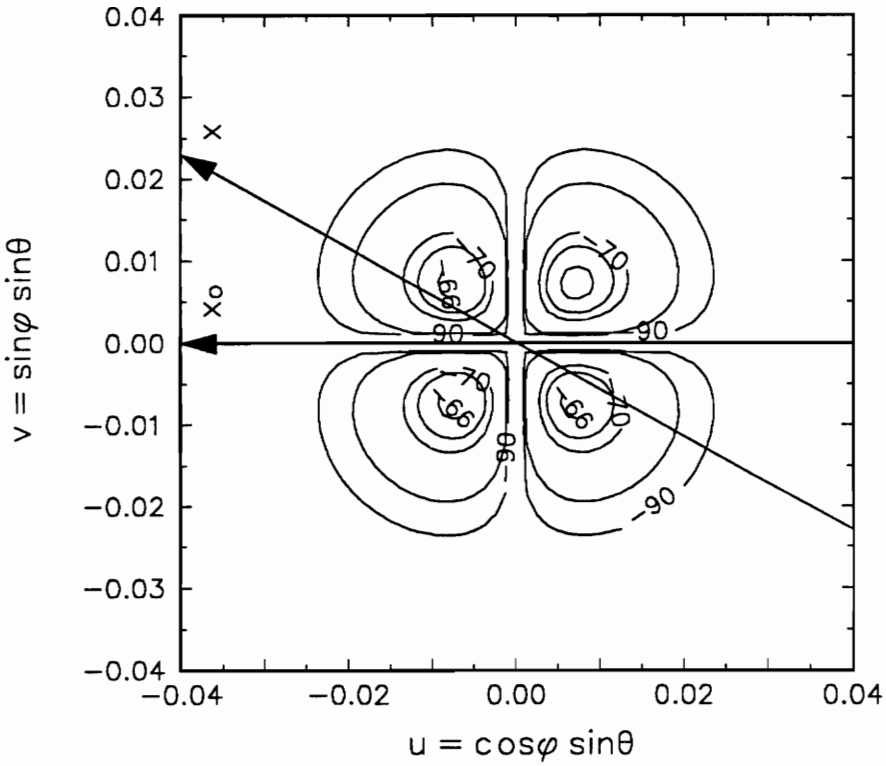

Figure 2.4. Contour plot (dB) of the computed cross-polarized pattern of the 171-λ diameter axisymmetric parabolic reflector specified in Table 2.2. The LP balanced feed and the output coordinate system are rotated by 30°.

Table 2.3.

Computed Performance Values for the Reflectors of Table 2.2

Main Reflector Configuration	Axisymmetric	Offset
Gain (G), dBi	48.62	47.39
Cross polarization level (XPOL), dB	-65.35	-22.40
Side lobe level (SLL), dB	-72.89	-31.90
Half-power beamwidth (HP), degrees	0.72	0.92

XPOL components in the 45° planes for an unbalanced feed, such as a dipole along the x_f-axis. If we change the feed in such a way that it becomes more and more "balanced", the curves in Fig. 2.5 will tend toward straight lines. However, there will always exist a residual cross-polarized field, even for ideal balanced feeds such as the Huygen's source, due to axial current flow [18].

2.3.2 Just Fully Offset Reflectors

Cross polarization behavior of offset reflectors is illustrated with a derivative of the 171 λ axisymmetric parent reflector of Table 2.2. The portion of the upper half of the axisymmetric reflector is retained such that the offset reflector of a 85.5 λ aperture (projected) diameter is just fully offset (i.e., $H = D/2$ in Fig. 2.1). The offset reflector corresponds to a 1.8-m diameter VSAT earth terminal antenna operating at 14.25 GHz. This is the 1.8-m reflector of a large commercial manufacturer of reflector antennas. If the feed remains pointed at the apex of the parent paraboloid

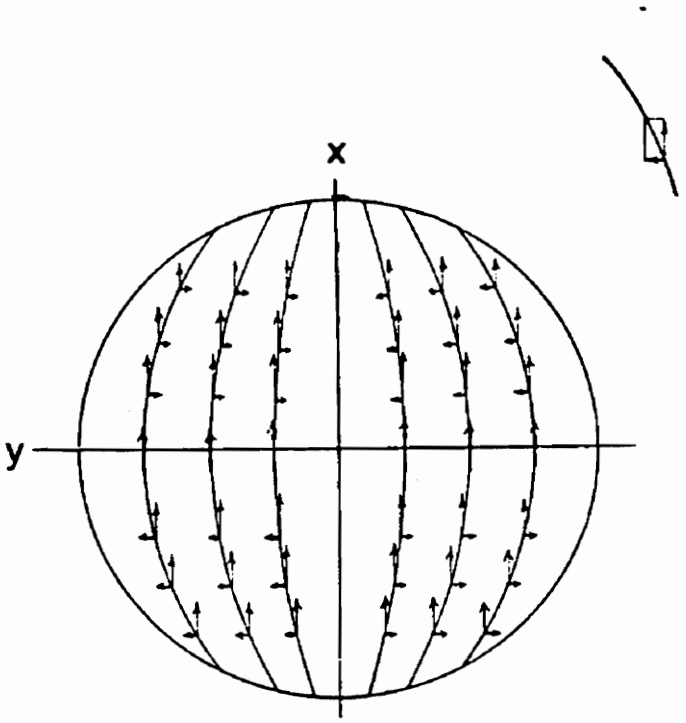

Figure 2.5. Typical aperture field distribution for an axisymmetric parabolic reflector illuminated by an unbalanced feed, such as a vertically polarized dipole. The arrows indicate the magnitude of the co- and cross-polarized components of the electric field (i.e., along the x- and y-directions, respectively).

(i.e., $\psi_f = 0°$), negligible XPOL will be generated [4]. However, this leads to large spillover and consequently gain loss. Therefore, in practice the feed is tilted to direct its pattern toward the reflector. This, however, introduces high cross polarization. The influence of the feed pointing angle, ψ_f, on the electrical characteristics of offset parabolic reflector antennas is discussed in the next section.

The offset configuration of Table 2.2 is not symmetric about the yz-plane (normal to the plane of symmetry), and therefore the cross polarization is not canceled in this plane as in the axisymmetric case. In fact, the peak XPOL levels occur in the yz-plane. However, reflector symmetry is still present about the xz-plane, and no substantial XPOL occurs in that plane. These results are well known [17] and are demonstrated for the offset reflector example with the XPOL contour plot shown in Fig. 2.6, for which the feed has a pointing angle of $\psi_f = \psi_B = 39.81°$. The feed again has the pattern of Fig. 2.2. The performance values are summarized in Table 2.3. The computed peak XPOL is -22.4 dB relative to the co-polarized beam maximum. Figure 2.6 indicates that the co-polarized pattern is still symmetric. It is worth noting that the peak XPOL levels occur at about the -6 dB level of the co-polarized main beam. A XPOL level of about -22 dB is often unacceptable high. The possibility of upgrading an existing single reflector configuration to a low cross-polarized dual offset Gregorian reflector antenna is investigated in detail in the next chapter.

In contrast to an axisymmetric paraboloid, rotation of a LP feed at the focal point of an offset reflector does not cause a corresponding rotation of the far-field pattern. This is illustrated with the example of an offset reflector with a feed rotated by an angle $\phi_f = 30°$ and tilted by $\psi_f = 39.81°$; the geometry is still given by Table 2.2 (offset case), although the feed is now rotated by 30°. Examination of the

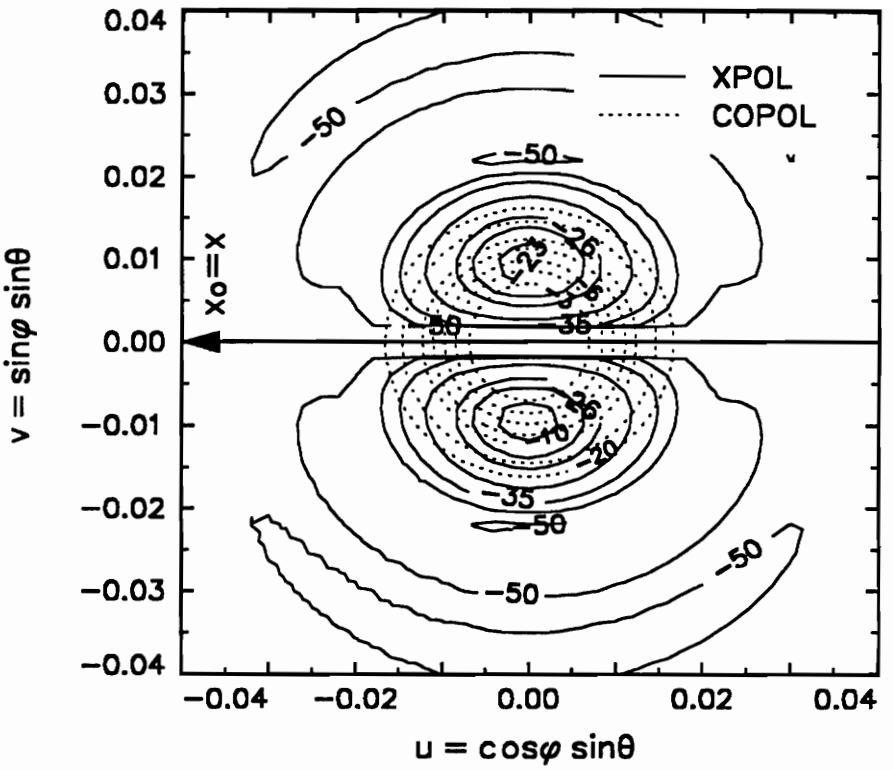

Figure 2.6. Contour plots (dB) of the computed co- (dashed curves) and cross-polarized (solid curves) patterns of the 85.5-λ diameter just fully offset parabolic reflector specified in Table 2.2. The balanced feed is linearly polarized in the x_f-direction ($\phi_f = 0°$).

reflector XPOL with a rotated LP feed also permits investigation of the instantaneous behavior of the XPOL generated by a CP feed. The XPOL contour plot (far-field) for this configuration is shown in Fig. 2.7. Although not shown, the co-polarization contour plot is equal to that of Fig. 2.6. Note that the secondary XPOL pattern remains stationary as the feed is rotated, provided that the output coordinate system is also rotated (see Section 2.3.1 for further details). This is because the polarization vector rotates with the feed. This conclusion was confirmed by extensive computer simulations and has been previously noted in the literature [24, 25].

As the electric field vector of a CP wave from a feed rotates with time (e.g., clockwise viewed along the direction of propagation), the field radiated from the reflector will also rotate in the same clockwise direction (although in the opposite direction of propagation). It will not move "backwards" presenting an instantaneous counterclockwise motion. Thus, although at each rotation angle there are high LP cross-polarized fields present in both the aperture distribution and far field pattern of the offset reflector (see Fig. 2.7), no circular XPOL is present in the radiated field.

Thus, we conclude that the offset parabolic reflector does not generate circular XPOL when illuminated by a balanced CP feed. This is a general result, not limited to just fully offset paraboloids. Also, due to sense reversal encountered upon reflection from the main reflector, the sense of the far field radiation is opposite to that of the feed [17]. For example, a right hand circularly polarized (RHCP) feed produces a left hand circularly polarized (LHCP) radiation in the reflector far field. Although CP is not depolarized by an offset reflector, the beam is squinted as explained in the Section 2.4. It should be mentioned that our analysis assumes a reflector diameter of at least 12 λ. Substantial circular XPOL can occur in small offset paraboloids ($D < 12\lambda$) with short focal lengths ($F/D_p < 0.25$). This problem is addressed in Section 2.4.

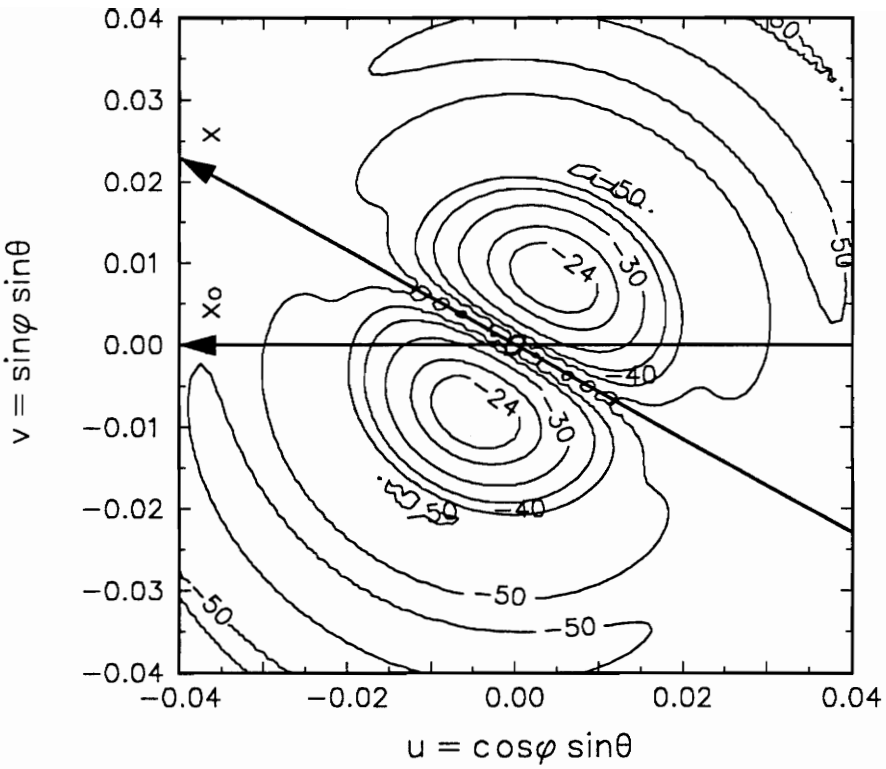

Figure 2.7. Contour plot (dB) of the computed cross-polarized pattern of the 85.5-λ diameter just fully offset parabolic reflector specified in Table 2.2. The LP balanced feed and the output coordinate system are rotated by 30°.

Finally, for completeness, Fig. 2.8 shows the aperture field orientation lines for an offset reflector illuminated by a x_f-directed dipole, as in Fig. 2.5 [26]. It is important to note that the field lines in Fig. 2.8 are not the same as those in the upper section of Fig. 2.5. The aperture distribution is altered due to the tilting of the feed (ψ_f); see Fig. 2.1. This causes the electric field vector to point away from the xz-plane (plane of symmetry) at all points in the aperture, in contrast to the axisymmetric case where the electric field points toward the xz-plane. This is not true for a feed with y_f-polarization since the tilting is restricted to the xz-plane and, therefore, does not alter the orientation of the electric field vector. In that case, the field lines in the aperture of the offset reflector are the same as those in the upper section of Fig. 2.5 after being rotated by 90°. All results presented in this section are also valid for the case where $H > D/2$ (i.e., general offset reflectors) addressed in the next section.

2.3.3 General Offset Reflectors

In this section we investigate the influence of the feed pointing angle, ψ_f, on cross polarization, gain, and side lobe level of offset reflectors having $H > D/2$ (i.e., general offset reflectors). Scattering from support structures is not included, but for an offset configuration these are typically negligible. In order to cite specific performance values, a specific configuration must be selected. We choose a reflector of diameter

$$D = 85.5\ \lambda \tag{2.11}$$

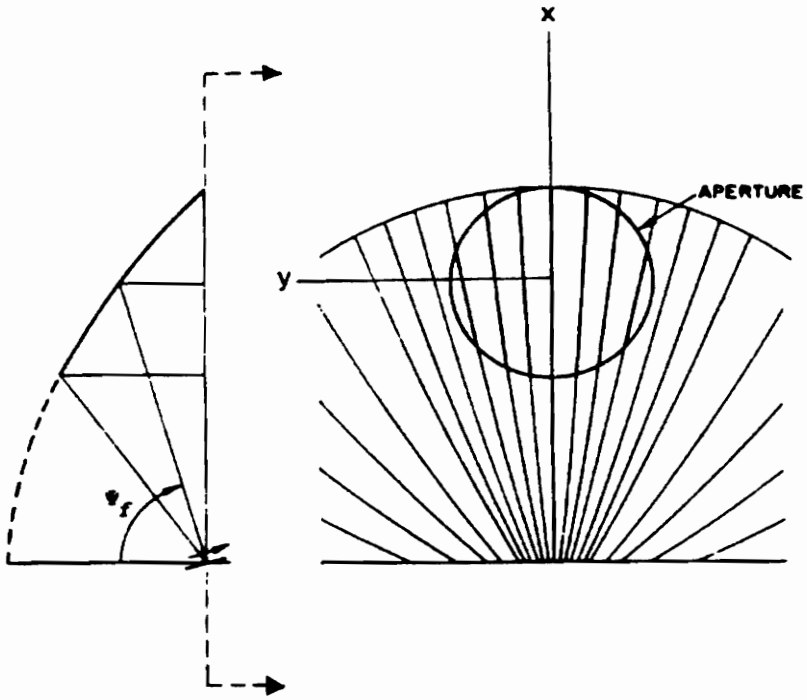

Figure 2.8. Typical aperture field orientation for an offset parabolic reflector illuminated by an unbalanced feed.

The reflector curvature is governed by

$$F/D_p = 0.3 \tag{2.12}$$

To be completely general, our study was conducted for a more than fully offset reflector ($H > D/2$). This provides a blockage-free region for structures in the focal region. The offset distance is

$$H = \frac{5D}{8} \tag{2.13}$$

corresponding to a geometry that is popular in VSAT applications.

The feed is modeled using the symmetric ("balanced") Gaussian radiation pattern with a 10 dB-beamwidth of 70°; see Fig. 2.2. This leads to a feed taper of FT_L = 10.0 dB, FT_U = 10.0 dB and edge illuminations of EI_L = -10.1 dB, EI_U = -14.6 dB for the case of $F/D_p = 0.3$, $H = 5D/8$ and the feed pattern maximum pointed to bisect the angle subtended by the reflector ($\psi_f = \psi_B$). The feed is linearly polarized along the x_f-direction, i.e. in the plane of offset. Note that feed taper does not strongly influence cross polarization; increasing feed taper from 10 to 20 dB reduces maximum cross polarization by only 1 dB [24].

Figure 2.9 shows XPOL, G, and SLL as the feed pointing angle is varied for the configuration of (2.11), (2.12), and (2.13). Note that XPOL decreases with decreasing feed angle, ψ_f. However, the gain and side lobe level must be evaluated as ψ_f is varied to ensure that there is no sacrifice in primary performance. We note from Figure 2.9 that the gain curve has a broad peak, and side lobe level is not very sensitive to feed pointing. In this analysis only the near-in sidelobes are considered.

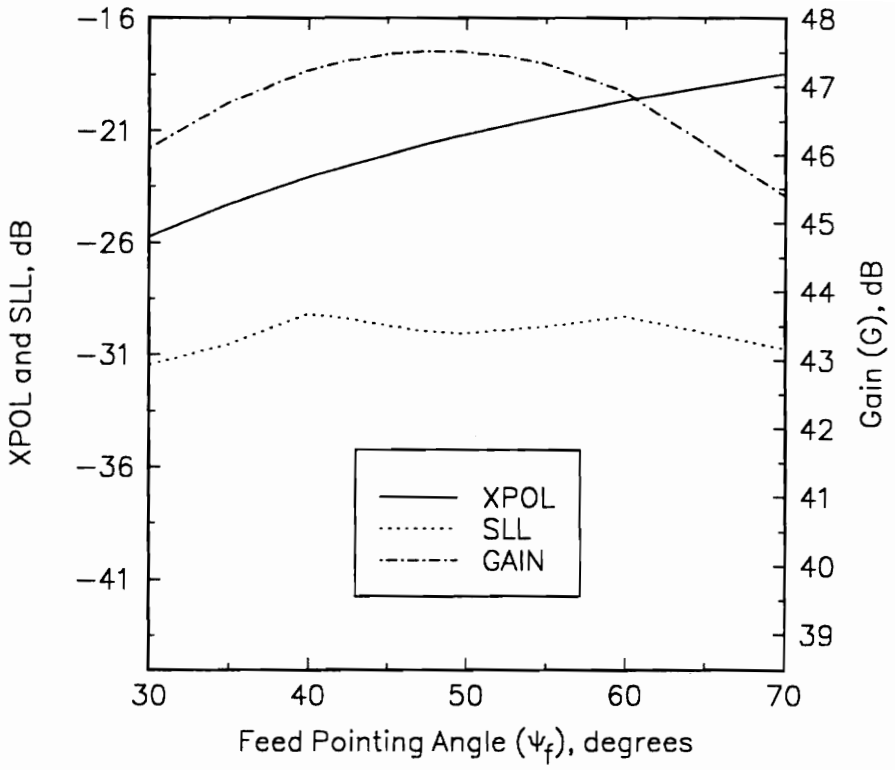

Figure 2.9. Peak cross polarization level (XPOL), side lobe level (SLL), and gain (G), as a function of ψ_f for an offset parabolic reflector of $(H/D) = 5/8$, $D = 85.5\lambda$, and $(F/D_p) = 0.3$.

For approximate designs, as is often sufficient in practice, the feed is aimed within the range

$$40° \leq \psi_f \leq 60° \tag{2.14}$$

in order to keep spillover losses (and subsequent gain loss) reasonable. Note that the values in (2.14) correspond to angles within $\pm 10°$ of the bisecting angle ψ_B. For peak gain operation, the feed must be pointed with an angle of $\psi_f = 47°$, which yields a peak gain of G = 47.52 dB.

A classical design scenario has now emerged. The feed angle, ψ_f, is reduced until desirable cross polarization performance is achieved or until gain is reduced as far as can be accepted. If, on the other hand, side lobe performance is a critical performance parameter, the feed pointing angle can be optimized to yield near the lowest SLL, with only small penalties in G and XPOL. It turns out that this operating point produces a balanced aperture illumination. That is, for a feed pointing angle of $\psi_f = \psi_E$ the edge illumination levels (in the plane of offset) in the aperture are equal, yielding a near-minimum sidelobe level. Figure 2.10 shows the side lobe level for our study configuration over the practical feed pointing angle range of (2.14). The feed pointing angle value of

$$\psi_f = \psi_E = 49.58°, \tag{2.15}$$

determined as discussed in the next paragraphs, falls near the local minimum SLL = -30.06 dB.

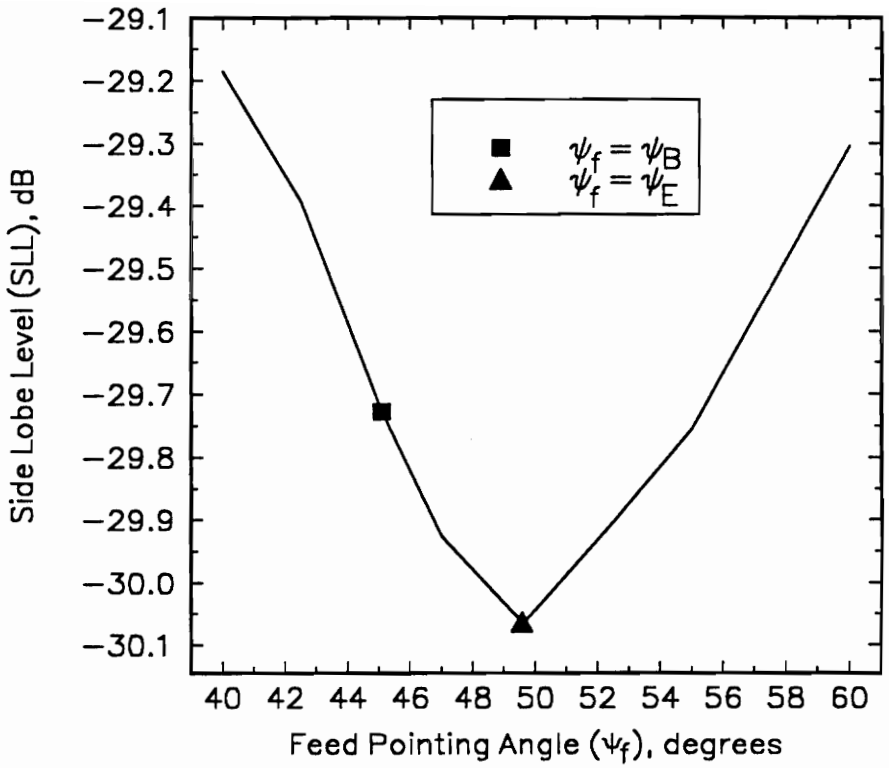

Figure 2.10. Peak side lobe level as a function of ψ_f ($40° \leq \psi_f \leq 60°$) for an offset parabolic reflector of $(H/D) = 5/8$, $D = 85.5\lambda$, and $(F/D_p) = 0.3$. $\psi_E \approx \psi_C$ for this specific example.

We now describe how to obtain the feed pointing angle, ψ_f, that yields a specified difference in edge illuminations:

$$\Delta EI = EI_U - EI_L \qquad \text{[dB]} \tag{2.16}$$

The negative of edge illumination is the sum of the feed edge taper, FT, and the spherical spreading loss, SPL. So (2.16) can be expressed as

$$FT_L + SPL_L = FT_U + SPL_U + \Delta EI \tag{2.17}$$

For a parabolic reflector, spherical spreading loss is given by [12]

$$SPL(\psi) = -20 \log \left[\cos^2 \frac{\psi}{2} \right] \tag{2.18}$$

Substituting (2.18) into (2.17) yields the design equation [4]

$$\Delta FT = FT_L - FT_U = 40 \log \left\{ \frac{\left[\cos \frac{\psi_L}{2} \right]}{\left[\cos \frac{\psi_U}{2} \right]} \right\} + \Delta EI \tag{2.19}$$

We illustrate the use of (2.19) for the case of a balanced aperture illumination; i.e., $\Delta EI = 0$, for the offset geometry of Fig. 2.10 ($D = 180$ cm, $H = 5D/8$, and $F/D_p = 0.3$). According to [3], the angles to the upper and lower edges of the reflector are $\psi_U = 79.61°$ and $\psi_L = 10.58°$, respectively. The design equation (2.19) gives

$$\Delta FT = 4.5 \text{ dB} \tag{2.20}$$

The angle between the upper and lower edges is

$$2\psi_S = (\psi_U - \psi_L) = 69.03^\circ \tag{2.21}$$

We introduce the graphical technique illustrated in Fig. 2.11 for determining the feed pointing angle required to produce the feed taper imbalance (2.20), which in turn yields a balanced edge illumination. The graphical technique is especially useful with measured feed pattern data; if the analytical form of the feed pattern is available, (2.17) can be solved using a numerical routine. The design starts by cutting a piece of gridded paper (with the same scale used in the plot of the feed pattern) with a width given by (11). The reference points 0 and ΔFT are marked as shown in Fig. 2.11. Finally, the marked piece of paper is moved on the feed radiation pattern plot until points 0 and ΔFT fall on the feed pattern curve. Next, the value of the angle between the pattern peak and the lower edge point, ΔFT, is read from the graph; in this example

$$\psi_P = 39.00^\circ \tag{2.22}$$

Finally, the feed pointing angle is computed by adding ψ_L to ψ_P; in this example we have

$$\psi_E = \psi_L + \psi_P = 10.58^\circ + 39.00^\circ = 49.58^\circ \tag{2.23}$$

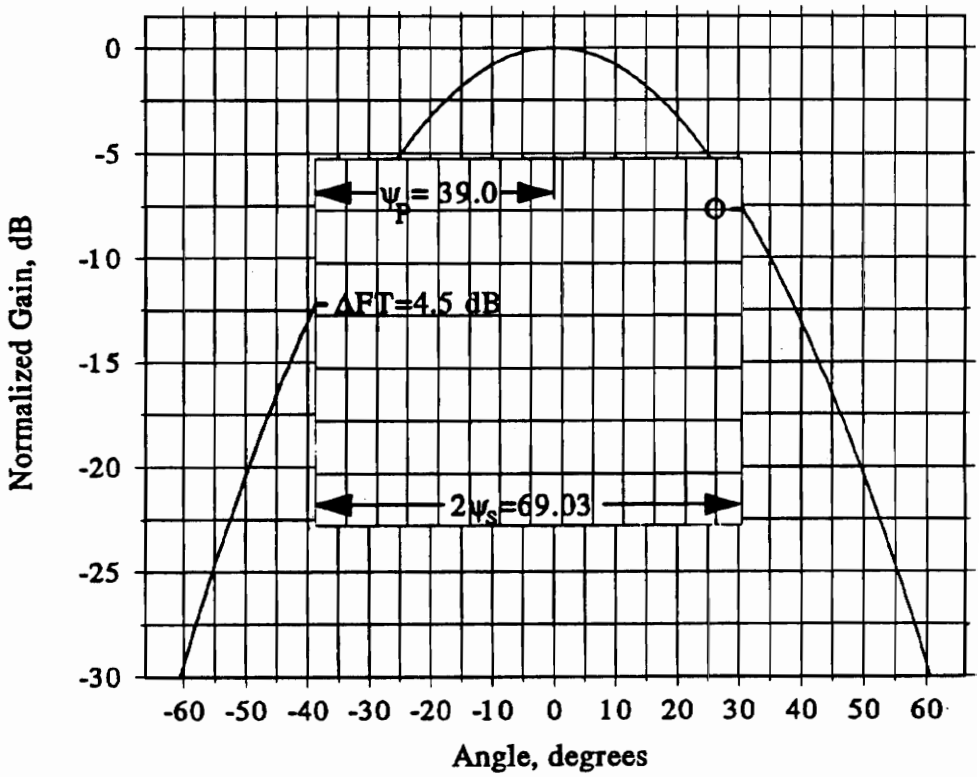

Figure 2.11. Graphical determination of the angle ψ_E.

All results presented in this section are also valid for the just fully offset case described in Section 2.3.2. In fact the just fully offset reflector can be viewed as a particular case of the general offset reflector geometry. When an offset reflector is illuminated by a balanced CP feed no substantial XPOL is generated, but the main beam squints off boresight. The beam squint phenomenon is is addressed in the next section.

2.4 Beam Squint In Single Reflector Configurations

Reflector antennas experience what is known as beam deviation and beam squint, which are now defined. As a feed is displaced from the focal point of a reflector, the pattern main beam is scanned to the opposite side of the reflector axis. This is referred to as beam deviation, and arises from a tipping of the aperture field phase plane relative to the reflector aperture plane. The main beam direction determined based on these considerations is herein referred to as the reference axis, which is tilted from the reflector axis (i.e., the z-axis in Fig. 2.1) according to the amount of feed displacement. For configurations employing a feed located at the paraboloid focal point, the reference axis is coincident with the reflector axis.

Beam squint is defined as the displacement of the main beam off the reference axis, and normally occurs in the plane orthogonal to the plane of symmetry (xz-plane in Fig. 2.1) and containing the reference axis. This is the yz-plane of Fig. 2.1 for feeds located at the focal point. Beam squint occurs in offset parabolic reflectors with CP feeds located on or off the focal point [27] and in axisymmetric parabolic

reflectors with CP feeds displaced from the focal point [27, 28]. In the configurations employing an off-focus CP feed, both the squint and deviation effects are present at the same time.

A somewhat surprising result is that beam squint can also occur with LP feeds in small offset parabolic reflectors ($D < 12\lambda$) with short focal lengths ($F/D_p < 0.25$) [29]. The squint is now restricted to the xz-plane of the offset reflector (plane of symmetry) and becomes negligible for most practical applications when the reflector is larger than 12 λ [29]. In order to verify this effect, we consider the small, just fully offset parabolic reflector specified in Table 2.4. The feed is linearly polarized in the x_f-direction with the pattern shown in Fig. 2.2. The co-polarized pattern cut computed by GRASP7 in the plane of symmetry, $\phi = 0°$, is shown in Fig. 2.12. Note that the main beam peak of gain 23.9 dBi is squinted -0.45° from boresight. As already mentioned in Section 2.3, linear XPOL in the plane of symmetry is very low (below -140 dB for this example). However, the squint effect can deteriorate the circular polarization performance for this class of small offset reflectors, introducing substantial circular XPOL (e.g., -30 dB) [29]. It should be mentioned that no squint occurs if the feed is polarized in the y_f-direction.

With the exception of the aforementioned case, beam squint occurs whenever [27]:

1) The reflector depolarizes the primary radiation, and

2) The orthogonal components of the incident field are not in phase. This is the case for a circularly polarized feed antenna.

Table 2.4.

Offset Reflector Configuration Employed in the LP Beam Squint Study

(a) Main Reflector Configuration	Offset
Shape	Paraboloid
Projected diameter (D), λ	6.0
Parent reflector diameter (D_p), λ	12.0
Focal length (F)	0.25 D_p
Offset of reflector center (H), λ	3.0
(b) Feed Configuration (on-focus)	
Polarization	Linear (x_f)
Pattern shape	Gaussian
Gain (G_f), dBi	14.04
10-dB beamwidth, degrees	70.0
Feed pointing angle (ψ_f), degrees	45.00
Edge Illum. (Lower,Upper), dB	(-16.5,-22.5)

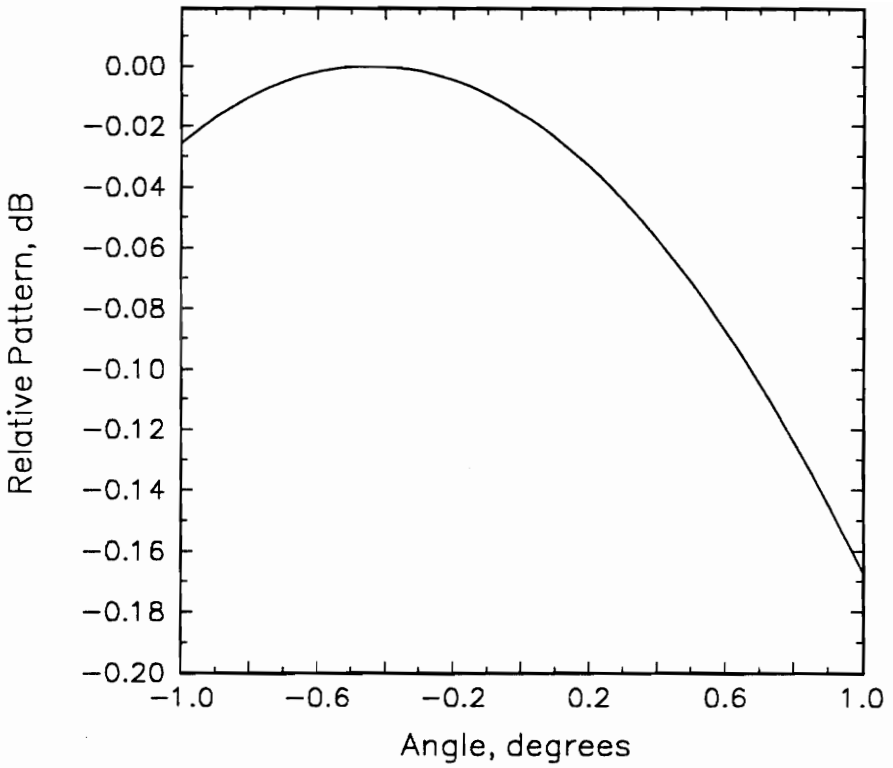

Figure 2.12. Pattern main beam computed for the just fully offset parabolic reflector specified in Table 2.4 with a LP feed located at the focal point. The pattern was computed in the plane $\phi = 0°$ (plane of symmetry). Note the beam squint from the boresight axis.

A practical formula for the prediction of the beam squint angle θ_S in offset parabolic reflectors with on-focus CP feeds is derived in [30], and for the geometry of Fig. 2.1 is given by

$$\theta_S = \mp \sin^{-1}\left(\frac{\sin\psi_f}{2Fk}\right) \tag{2.24}$$

where F is the focal distance, and k is the free space wave number $2\pi/\lambda$. A negative θ_S means that the beam is squinted toward the left (LHCP feed), and conversely, a positive θ_S indicates a squint to the right (RHCP feed). Equation (2.24) shows that the amount of squinting is inversely proportional to the focal distance F. That is, longer focal length reflectors experience less beam squint. If the feed is displaced from the focal point, an equation similar to (2.24) is derived in [27].

As an illustrative example, we consider the just fully offset configuration specified in Table 2.5 with a CP feed with the pattern of Fig. 2.2; this geometry was selected because it is used in VSAT applications at 18.5 GHz and measured data are available [3, 24]. Figure 2.13 shows co-polarized pattern cuts computed using GRASP7 in the $\phi = 90°$ plane (i.e., normal to the plane of symmetry) with opposite sense CP feeds. For the RHCP main beam case (the feed is LHCP) the squint is to the left as observed in Fig. 2.13. Conversely, the LHCP main beam squints to the right. From Fig. 2.13 we note that the angle between the two beams (total beam separation) is 0.700°, which compares favorably with the value of 0.686° from (2.24). The reported measured value [24, 3] is 0.750°. Although not shown in Fig. 2.13, circular XPOL is low (maximum of 42.71 dB below the gain of 33.88 dBi for any of the feed polarizations).

Table 2.5.

Offset Reflector Configuration Employed in the CP Beam Squint Study

(a) Main Reflector Configuration	Offset
Shape	Paraboloid
Projected diameter (D), λ	18.8
Parent reflector diameter (D_p), λ	37.6
Focal length (F)	0.25 D_p
Offset of reflector center (H), λ	9.4
(b) Feed Configuration (on-focus)	
Polarization	Circular
Pattern shape	Gaussian
Gain (G_f), dBi	14.04
10-dB beamwidth, degrees	70.0
Feed pointing angle (ψ_f), degrees	45.00
Edge Illum. (Lower,Upper), dB	(-16.5,-22.5)

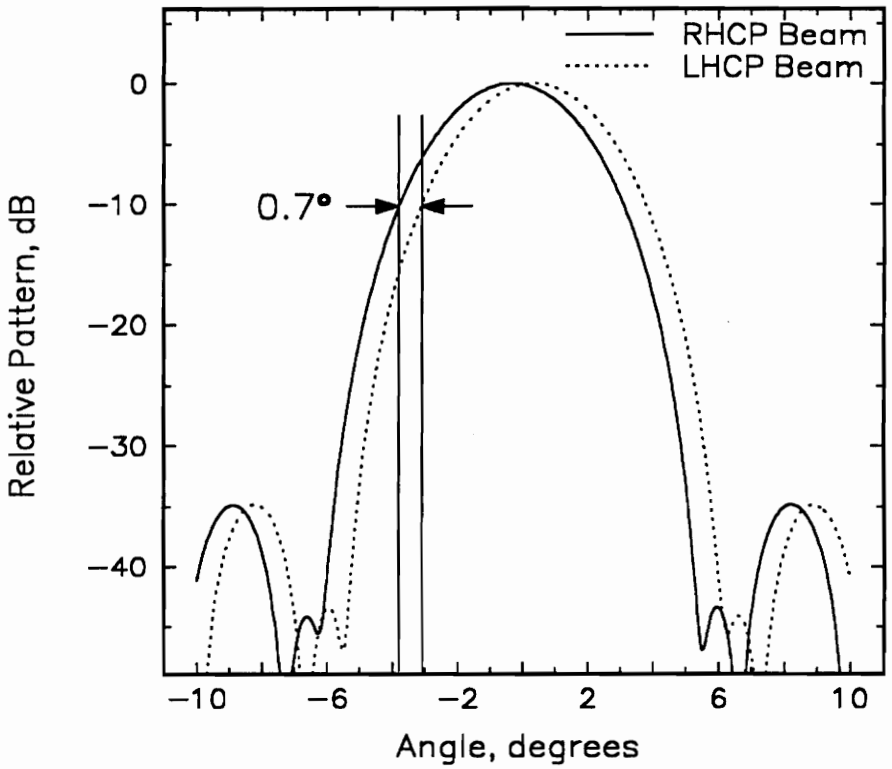

Figure 2.13. Computed RHCP (solid curve) and LHCP (dotted curve) far-field patterns in the $\phi = 90°$ plane (normal to the plane of symmetry) for the 18.8 λ just fully offset paraboloid specified in Table 2.5. Note the beam squint effect.

Summarizing, offset parabolic reflectors illuminated by a CP feed do not present substantial XPOL, as explained in Section 2.3; however, beam squint does occur. We now present a brief explanation of the beam squint generation mechanism.

Figure 2.8 shows that the electric field components on the left side of the reflector ($y > 0$) always lead or lag in phase relative to the ones on the right side, depending on whether the primary field is LHCP or RHCP. This leads to a phase slope condition across the aperture, which squints the main beam to the left (negative angles in Fig. 2.13) or to the right (positive angles in Fig. 2.13). As an illustration, consider any two points in the offset paraboloid aperture that are equidistant from the reflector plane of symmetry. If the feed is LHCP, the electric field at those points rotates counter-clockwise (RHCP main beam) viewed as shown by Fig. 2.14. Thus, the electric field vector to the left is leading the one to the right, and as a final result (considering the influence of all points) the beam squints to the right (the view in Fig. 2.14). This is equivalent to a squint to the left in the yz-plane of the reflector coordinate system (negative angles in Fig. 2.13).

2.5 Dual Reflector Considerations

In dual offset reflector systems, the secondary reflector provides an additional degree of freedom which can be used to cancel the cross polarization [31]; see Chapter 3 for further details on the optimization of dual offset reflectors for low linear XPOL. Beam squint occurs only in dual offset reflectors that are not optimized for low linear XPOL. If the Mizugutch and/or Rusch conditions [31] are satisfied, the reflector does not depolarize the primary radiation (on-focus feed), and therefore no squint occurs. Thus, we conclude that properly designed dual offset configurations can present negligible levels of XPOL and beam squint. Although not presented here,

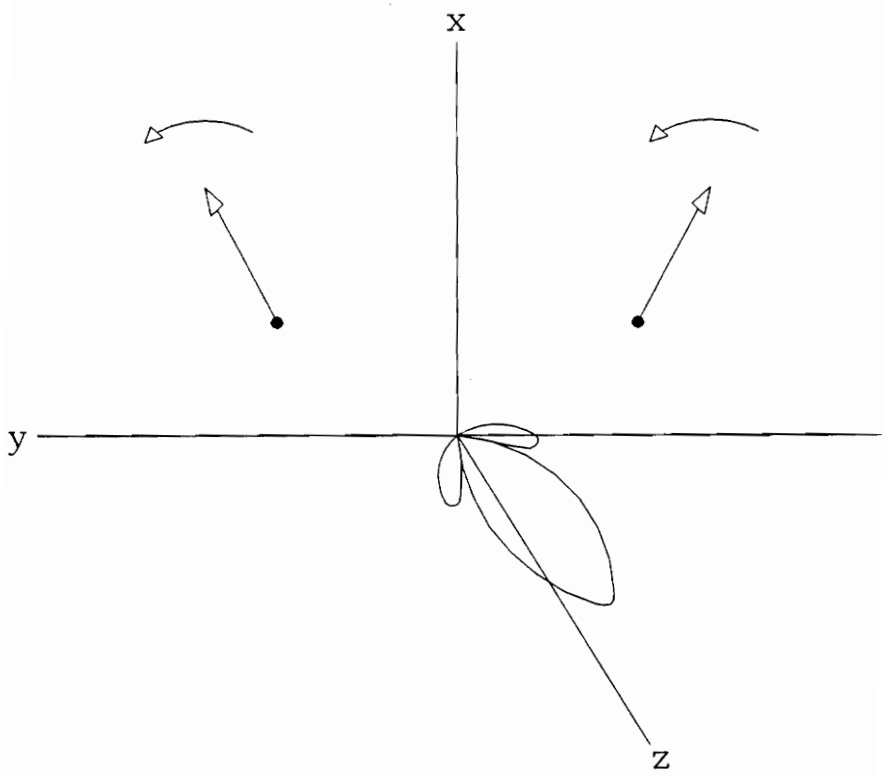

Figure 2.14. Beam squint generation mechanism.

these results were verified through several computer simulations using GRASP7 and agreement with results reported in the literature [27] was obtained; see Section 3.6.2.

2.6 Conclusions

A comprehensive description of the cross polarization (XPOL) behavior in parabolic reflectors was presented. Emphasis was given to the offset parabolic reflector illuminated by a balanced circularly polarized (CP) feed. However, both the offset and axisymmetric configurations with linearly polarized (LP) feeds were also considered. The absence of circular XPOL in offset parabolic reflectors larger than 12 λ in diameter and illuminated by CP feeds was explained.

Beam squint and beam deviation (scanning) phenomena were presented and the former was examined and explained in detail. The commercial code GRASP7 [15] was used to compute all of the far-field pattern cuts and uv-contour plots presented in the figures. Agreement between computations and predictions using the simple model of (2.24) with measured beam squint values obtained from the literature for the study case was excellent.

There are a large number of possible reflector geometries, feed types, locations, and polarizations. Representative configurations were examined to provide specific values as well as general conclusions. The many possible configurations are summarized in Table 2.6 together with XPOL, beam squint, and beam deviation effects. Table 2.6 shows that unbalanced feeds (i.e., the primary radiation pattern is not symmetric) usually generate substantial XPOL independent of the feed polarization or reflector configuration. Also, displacing the feed from the focal point normally generates XPOL and beam deviation. Most of the results presented in Table 2.6 were verified in this work.

Table 2.6.

Presence of Cross Polarization, Beam Squint, and Beam Deviation Effects in Single Parabolic Reflector Antennas

Reflector Geometry	Feed			Cross. Pol.	Beam Squint	Beam Deviation
	Location	Type	Polarization			
Axi-Symmetric	On-Focus	Balanced	Linear	No	No	No
			Circular	No	No	No
		Unbalanced	Linear	Yes	No	No
			Circular	Yes	No	No
	Off-Focus	Balanced	Linear	Yes	No	Yes
			Circular	Yes	Yes	Yes
		Unbalanced	Linear	Yes	No	Yes
			Circular	Yes	Yes	Yes
Offset ($\psi_f > 0°$)	On-Focus	Balanced	Linear	Yes	No*	No
			Circular	No*	Yes	No
		Unbalanced	Linear	Yes	No*	No
			Circular	Yes	Yes	No
	Off-Focus	Balanced	Linear	Yes	No*	Yes
			Circular	Yes	Yes	Yes
		Unbalanced	Linear	Yes	No*	Yes
			Circular	Yes	Yes	Yes

*Except for small reflectors ($D < 12\lambda$ and $F/D_p < 0.25$); see Section 2.4 for further information.

Beam squint occurs only in dual offset reflectors not optimized for low linear XPOL. If the Mizugutch and/or Rusch conditions are satisfied, the reflector does not depolarize the feed radiation (on-focus feed), and therefore no squint occurs. Thus, dual offset configurations can be free from circular XPOL and beam squint, if properly designed to present low linear cross polarization.

In addition, The behavior of the cross polarization in offset reflectors as a function of the feed pointing angle ψ_f was studied. Results obtained from several numerical simulations using GRASP7 showed that the orientation of the feed strongly influences cross polarization. Cross polarization can be significantly reduced by using a small feed pointing angle, ψ_f. However, small angles lead to high spillover. Thus, high cross polarization and side lobe levels can be expected if high gain is to be maintained.

We also note that for large F/D_p values (which, in turn, lead to reduced feed pointing angles, ψ_f) the cross polarization level improves (decreases) but that side lobe level degrades (increases). In addition, there is also a penalty in gain. However, unlike ψ_f, the curvature of the dish (through F/D_p) is not easily adjusted. It is worth mentioning that XPOL decreases as the offset distance H is increased, although not very significantly. In dual offset reflector systems, the secondary reflector provides an additional degree of freedom which can be used to cancel the geometrical optics cross polarization [31]; this is addressed in the next chapter.

Chapter 3

Design of Dual Offset Gregorian Reflector Antennas for Minimum Cross Polarization for a Specified Main Reflector and Feed Pattern

3.1 Introduction

In this chapter the addition of a subreflector to an existing offset parabolic reflector to reduce cross polarization level is investigated. A complete procedure to upgrade an existing offset parabolic reflector to a low cross-polarized dual offset Gregorian reflector is presented. In addition, the possibility of using the same sub-optics assembly (i.e., subreflector and feed) with different main reflectors is investigated. Case examples based on real reflector antenna configurations are discussed in detail. Measured pattern data and results computed with the Virginia Tech code PRAC and the commercial code GRASP7 are presented and compared, validating the proposed procedures.

3.2 Reflector Upgrading Concepts and Requirements

As discussed in Chapter 1, a cost effective way to improve the performance of an existing offset prime-focus reflector is to add a subreflector, forming a dual reflector system with very low cross polarization. There is a large international market for this product. In fact, a few antenna manufacturers have recently advertised such a product. However, this is a difficult design problem given the constraints of using an existing main reflector and feed.

The motivation to use a specified main reflector often arises from a desire to use an existing mold which is usually very expensive. Frequently, reflector antenna manufacturers offer a complete line (i.e., "family") of single offset paraboloids. In such a family, the paraboloids have different aperture sizes, but share a similar F/D ratio. In that case, the molds are related to each other by a scaling factor. When introducing a dual reflector configuration it is also desirable to use the same suboptics assembly (i.e., feed and subreflector) with all reflectors in a family. In the present work this problem is referred to as reflector system upgrading.

The degrees of freedom available for the design of a dual reflector are the subreflector shape and the relative positions and orientations of the reflectors and feed. The procedures available in the literature to design low XPOL, non-shaped dual offset reflector antennas are not especially suitable for upgrading existing configurations. In addition, they assume an ideal, pure linearly polarized feed (e.g., [32]). Since the proposed problem is based on a practical setting, we must consider the possibility of having feeds with relatively large XPOL levels, and investigate the influence of feed XPOL on the total system XPOL. Many applications impose limitations on system XPOL. For example, the EUTELSAT specification for VSAT

communications is -35 dB within the -1 dB contour of the main beam [11]. In the present work an effort is made to achieve -35 dB XPOL over a broad pattern region (i.e., main beam and near-in sidelobes), thus satisfying the EUTELSAT requirement.

We have shown in a previous work that single offset reflectors illuminated by conventional feeds usually present a XPOL level much worse than -35 dB [4]. Offset reflector systems (single and properly designed dual configurations) employing a parabolic main reflector larger than 12 λ and illuminated by circularly polarized (CP) feeds do not present substantial circular XPOL [33]; see Chapter 2. In the same chapter we commented that a dual offset configuration optimized for low linear XPOL (e.g., -35 dB or better) presents negligible beam squint when illuminated by a CP feed, as illustrated in Section 3.6.2. This property allows such a reflector antenna to operate with either a LP or a CP feed over a broad bandwidth without the need of being repositioned to eliminate beam squint. This is especially important in satellite and deep space communications.

A Gregorian configuration is selected for intensive study here because our analysis includes the use of just fully offset paraboloids as main reflectors (i.e., the bottom of the reflector just touches its axis of symmetry). These reflectors are widely employed in commercial applications. A Cassegrain configuration is more appropriate for main reflectors other than the just fully offset due to inherent blockage; see Fig. 3.1. For details on the Gregorian and Cassegrain antennas see [31]. However, this is not a restriction since all derivations presented in this work are valid for main reflectors with any degree of offset.

An example of a dual offset Gregorian configuration employing a main reflector that is not just fully offset is the Green Bank Telescope operating as a dual offset system [7, 8]. The Gregorian configuration permits the main reflector to be

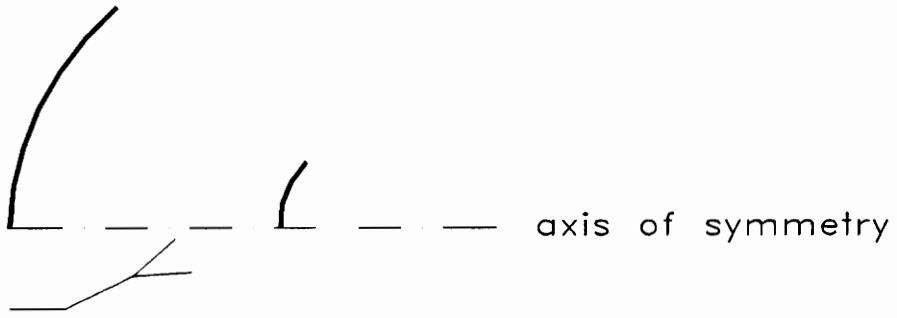

(a) Just fully, dual offset Cassegrain antenna

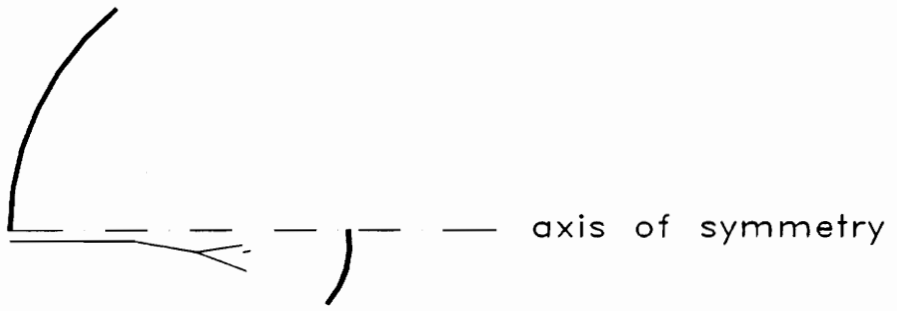

(b) Just fully, dual offset Gregorian antenna

Figure 3.1. Dual offset reflector antenna configurations employing a main reflector that is just fully offset. Note that only the Gregorian configuration (b) is free of blockage.

used as a prime-focus offset system without the need of removing the subreflector. This is not possible with a Cassegrain configuration [7].

An extensive search of the open literature showed that methods for upgrading existing prime-focus reflector systems in a general and systematic way are not available. The reflector upgrading problem addressed in this dissertation is summarized as follows:

- Introduce a subreflector to an existing offset main reflector in order to form a low cross-polarized dual offset Gregorian reflector antenna (XPOL $\leq$ -35 dB); see Section 3.4.

- Account for the XPOL characteristics of low-cost, conventional feed antennas and investigate methods of reducing feed influence on XPOL. This is addressed in Chapters 4 and 6.

- Use the same sub-optics assembly (i.e., feed and subreflector) with a family of main reflectors with different sizes but similar F/D ratios; see Section 3.5.

- Impose a constraint on the clearance between the bottom of the main reflector and the feed axis in order to lower manufacturing costs. This is addressed in Chapter 5.

The procedure produces a low cross-polarized dual offset Gregorian antenna which has adequate clearance between the feed axis and the bottom of the main reflector. In addition, the resulting configuration has the ability to operate with either a LP or a CP feed without the need of being repositioned (no substantial beam squint). The attraction of this procedure is that an existing main reflector and a low-cost, conventional feed are employed, thus requiring minimum incremental capital outlay. These constraints are not taken into account by other design procedures.

3.3 Dual Offset Gregorian Geometry and Conditions for XPOL Minimization

Our main goal is to upgrade an existing prime-focus offset reflector antenna to a dual offset Gregorian reflector antenna with low XPOL. This is accomplished by the addition of an ellipsoidal subreflector to the original single reflector. The general geometry of a dual offset Gregorian antenna is presented in Fig. 3.2 and the symbols are defined in Table 3.1. If the subreflector and feed are positioned according to Mizugutch [16] and/or Rusch [31] conditions, the resultant dual configuration presents low linear XPOL when illuminated by a pure linearly polarized feed. Mizugutch [16] gave the following condition necessary to cancel the cross polarization introduced by the reflector system:

$$\tan\alpha = \frac{|e^2-1|\sin\beta}{(1+e^2)\cos\beta - 2e} \tag{3.1}$$

where α is the feed pointing angle measured relative to the ellipsoid axis of symmetry (x_S), β is the angle between the ellipsoid and the parent paraboloid axes (x_S and s, respectively), and e is the subreflector eccentricity ($0 < e < 1$ for an ellipsoid). Mizugutch condition is derived in Appendix C (Chapter 12). Rusch [31] gave the following condition to minimize simultaneously XPOL and spillover loss (i.e., feed radiation missing the subreflector) based on the equivalent paraboloid formulation [31]:

$$\tan\frac{\beta}{2} = (\frac{e-1}{e+1})^2 \tan(\frac{\beta+\psi_c}{2}) \tag{3.2}$$

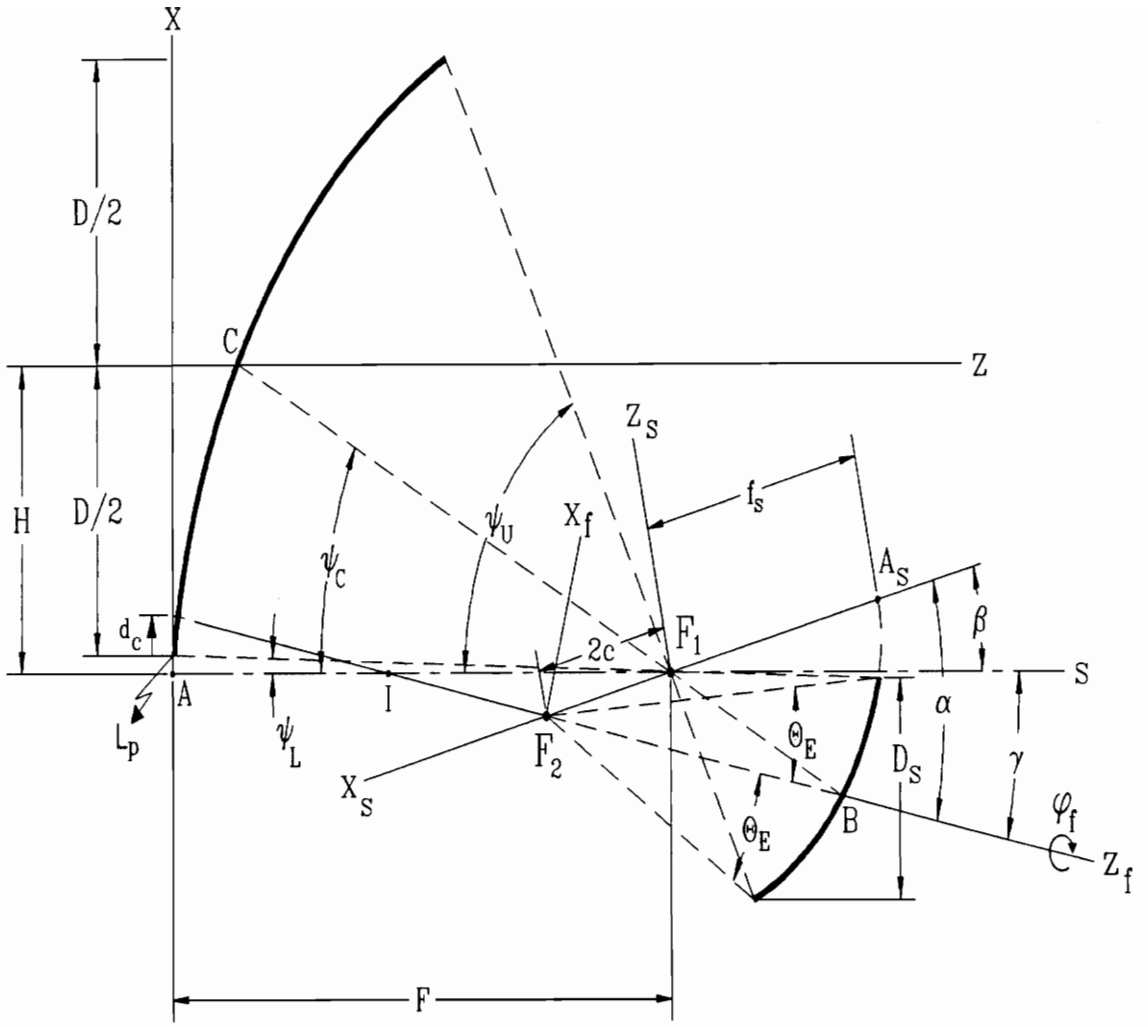

Figure 3.2. Geometry of the dual offset Gregorian reflector antenna. The symbols are defined in Table 3.1.

Table 3.1.

Definitions of Symbols

D = Diameter of the projected circular aperture of the parabolic main reflector.

D_p = Diameter of the projected circular aperture of the parent paraboloid.

H = Offset of reflector center

F = Paraboloid focal length.

Point F_1 = Common focal point of the parabolic main reflector and ellipsoidal subreflector.

Point F_2 = Ellipsoid focal point; feed antenna location.

Point A = Apex of the parent paraboloid.

Point A_s = Apex of the ellipsoidal subreflector.

Point B = Point on subreflector which bisects subtended angle viewed from F_2. Point B also results from the intersection of the ray coming from point C on the main reflector and the feed axis (z_f).

Point C = Point on main reflector which projects to the center of the circular projected aperture.

Point I = Point resultant from the intersection of the main reflector axis of symmetry (s) and the feed axis (z_f).

Point L_p = Projection of the bottom of the main reflector onto the x-axis.

ψ_C = Angle of feed antenna pattern peak after reflecting on the subreflector relative to the main reflector axis of symmetry (s).

ψ_U = Angle subtended by the parabolic main reflector as viewed from the focal point F_1.

Table 3.1. **(cont.)**

D_S = Height of the ellipsoidal subreflector.

e = Subreflector eccentricity ($0 < e < 1$ for an ellipsoid).

c = Half of the interfocal distance.

f_s = Distance between a focal point and the closest ellipsoid apex.

α = Feed pointing angle measured relative to the ellipsoid axis of symmetry (x_S).

β = Angle between the ellipsoid and parent paraboloid axes of symmetry (x_S and s, respectively).

γ = Angle between the main reflector and feed axes (s and z_f, respectively).

θ_E = Half of the angle subtended by the subreflector as viewed from the feed antenna location (ellipsoid focal point F_2).

ϕ_f = Rotation of the feed antenna with respect to the feed axis z_f. A positive ϕ_f denotes a clockwise rotation when looking at the feed.

d_c = Distance between the projection of the bottom of the main reflector (point L_p) and the intersection of the feed axis (z_f) with the x-axis. For $d_c = 0$, the feed axis intersects the projection of the bottom of the main reflector (point L_p). For $d_c < 0$, there is a clearance between the bottom of the main reflector and the feed axis.

We note that (3.2) is valid only for main reflectors with a circular projected aperture [31]. However, there is not such a condition for the ellipsoidal subreflector, which has in general an elliptical projected aperture; see Fig. 3.3 in Section 3.4. The angle ψ_c is the angle from the focal point F_1 through the center of the main reflector (point C) and is given by

$$\psi_c = 2\tan^{-1}(\frac{H}{2F}) \tag{3.3}$$

Our design procedure is based on (3.1) and (3.2) and its initial part is similar to the one given in [32]. The procedure is especially valuable in the design of dual reflectors that upgrade a specified offset main reflector in order to obtain a low cross-polarized reflector system. Once the main reflector is specified (from an existing prime-focus system), the procedure is used to determine the corresponding low cross-polarized dual configuration. The procedure published in [32] treats the main reflector specifications as output parameters instead of design constraints.

Our procedure begins with a design that employs canonical shapes for the reflectors and a geometry determined according to Mizugutch and Rusch conditions (3.1) and (3.2). This design is herein referred to as the classical configuration. Then feed cross polarization effects and practical manufacturing constraints are imposed resulting in non-conventional designs. These parameters are not taken into account by any other procedure and are discussed in detail in the next chapters. We now present the methodology used in the upgrading process.

3.4 Design Methodology and Numerical Implementation

As discussed in the last section, the initial part of our design procedure is dedicated to upgrade an existing main reflector and is similar to the one given in [32]. In fact, most of the basic equations were derived in [32] but they are applied here in a different fashion in order to allow the main reflector specifications to be used as input parameters. The rest of our procedure is not related to the one in [32] and is presented in future chapters. The design methodology is valid for the synthesis of dual offset Gregorian reflector antennas with any degree of offset and starts by determining the angle β from the following approximate equation [32]

$$\beta \cong 2\tan^{-1}[\frac{8HF}{D^2}\tan^2(\frac{\theta_E}{2})] \tag{3.4}$$

where θ_E is the feed edge angle, H is the distance between the main reflector center to the axis of symmetry, D is the main reflector diameter, and F is the distance of its focal point to the apex. See Fig. 3.2 for further details. Equation (3.4) can be derived from geometrical considerations and provides a good approximation for small values of θ_E [32]. Next, a rearranged version of (3.2) is employed to determine the eccentricity e [32]

$$e = \frac{1 - \sqrt{\frac{\tan\frac{\beta}{2}}{\tan(\frac{\beta+\psi_c}{2})}}}{1 + \sqrt{\frac{\tan\frac{\beta}{2}}{\tan(\frac{\beta+\psi_c}{2})}}} \tag{3.5}$$

We now employ Dragone condition [34] to determine the feed pointing angle α. Dragone condition is a modified version of (3.1) and is derived in the Appendix C (Chapter 12).

$$\alpha = 2\tan^{-1}[(\frac{e+1}{1-e})\tan\frac{\beta}{2}] \tag{3.6}$$

Finally, the half distance c of the subreflector interfocal length is given by [32]

$$c = \frac{eD_s}{(1-e^2)[\frac{sin\psi_U}{e\cos(\psi_U+\beta)+1} - \frac{sin\psi_L}{e\cos(\psi_L+\beta)+1}]} \tag{3.7}$$

where D_s is the subreflector height, projected onto the main reflector aperture plane. ψ_L and ψ_U are the angles subtended to the lower and upper edges of the reflector, respectively, and are given by [3]

$$\psi_L = 2\tan^{-1}(\frac{H-D/2}{2F}) \tag{3.8}$$

and

$$\psi_U = 2\tan^{-1}(\frac{H+D/2}{2F}) \tag{3.9}$$

Since the starting point of the design via (3.4) is an approximate equation, we must now verify if the result is close to the desired one. This can be done by determining the subreflector edge angle θ_E, as observed from the feed phase center [32]

$$\theta_E = 2\tan^{-1}\{(\frac{1-e}{1+e})\tan[\frac{\psi_U+\beta}{2}]\} - \alpha \tag{3.10}$$

If the value of θ_E computed from (3.10) is not equal to the one used in (3.4), one should repeat the process described by (3.4) to (3.10) using a new value for β until the desired θ_E is obtained. If this is not done, the resulting θ_E may be less than the feed edge angle to be used in practice, resulting in high spillover loss.

Figure 3.3 shows the geometry of an offset subreflector obtained from the intersection of a conic section around its focal axis, and a circular cone of half-angle ψ_S. If the conic is an ellipsoid (i.e., $0 < e < 1$), it is easy to show that the projections onto both $x_S y_S$- and $y_S z_S$- principal planes are ellipses [35]. In particular, the equation of the projection of the intersection curve (rim) on the $z_S y_S$-plane is given by

$$\frac{(z_S - Z_{S_c})^2}{{a_s}^2} + \frac{y_S^2}{{b_s}^2} = 1 \tag{3.11}$$

where

$$Z_{S_c} = \frac{(1+e)[e\cos(\beta+\psi_L+\psi_S)+\cos\psi_S]\sin(\beta+\psi_L+\psi_S)}{(1-e^2)\sin^2(\beta+\psi_L+\psi_S)+[\cos(\beta+\psi_L+\psi_S)+e\cos\psi_S]^2} f_s \tag{3.12}$$

$${b_s}^2 = \frac{(1+e)^2\sin^2\psi_S}{(1-e^2)\sin^2(\beta+\psi_L+\psi_S)+[\cos(\beta+\psi_L+\psi_S)+e\cos\psi_S]^2} f_s^2 \tag{3.13}$$

$${a_s}^2 = \frac{(1+e)^2[\cos(\beta+\psi_L+\psi_S)+e\cos\psi_S]^2\sin^2\psi_S}{\{(1-e^2)\sin^2(\beta+\psi_L+\psi_S)+[\cos(\beta+\psi_L+\psi_S)+e\cos\psi_S]^2\}^2} f_s^2 \tag{3.14}$$

and f_s is the distance between any of the ellipsoid focal points to the closest apex. Z_{S_c} is the Z_S-coordinate of the center of the projected subreflector, and b_s and a_s are respectively the minor and major half-axes of the projected subreflector; see Fig. 3.3

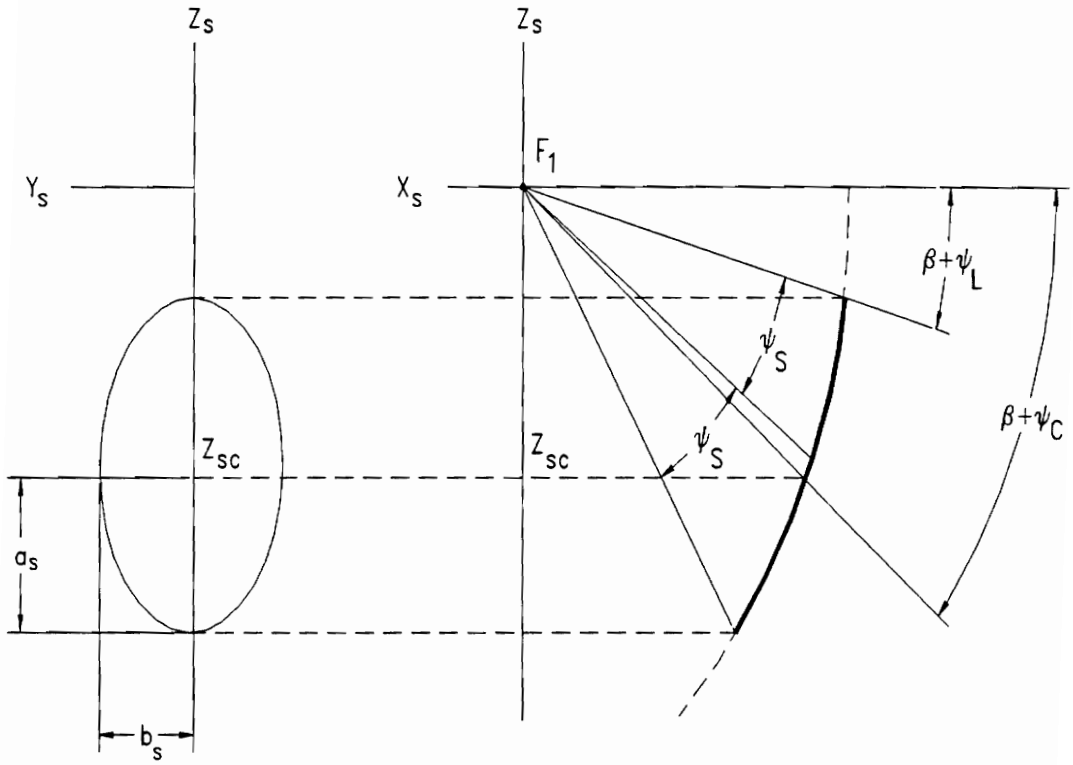

Figure 3.3. Intersection of an ellipsoid section with a circular cone.

for further details. The angle ψ_S is half of the angle that subtends the main reflector (or the subreflector) and is given by

$$\psi_S = \frac{\psi_U - \psi_L}{2} \tag{3.15}$$

It is known [31, 35] that any ray coming from one of the focal points, say F_2, is reflected by the ellipsoid surface towards the other focal point, F_1 (see Figure 3.2). Due to this conic section property, any circular cone of rays emanating from F_2 with axis F_2B will then be reflected as another circular cone of rays with vertex at the other focal point F_1 and axis F_1B. Thus, if F_1 is coincident with the paraboloid focal point F, and the feed is located at F_2, a perfect circular cone of rays originated at F_1 will illuminate the paraboloid. Due to the parabola reflecting property, a plane wave will then appear at the paraboloid aperture plane. Diffraction effects are ignored in this analysis.

The whole iterative process described by (3.4) to (3.10) was implemented in the program OPTIMUM. OPTIMUM designs a dual offset Gregorian antenna optimized for minimum XPOL for a given offset main reflector and feed pattern. Dual offset reflector configurations produced by OPTIMUM present a cross polarization level at least 35 dB below the main beam co-polar peak, when illuminated by a feed antenna purely polarized in the x_f or y_f directions. Once the design is completed, OPTIMUM presents a detailed description of the geometrical configuration. The main reflector is specified by the user, thereby permitting the use of an existing mold which is usually very expensive. This allows reflector antenna manufacturers to meet stringent requirements on XPOL with minimal capital outlay. Typical input and output parameters used in OPTIMUM are (see Fig. 3.2 and Table 3.1):

Input parameters required by OPTIMUM: D, F, H, θ_E, and D_S.

Output parameters generated by OPTIMUM: θ_E, α, β, e, c, f_s, d_c, ψ_C, ψ_L, ψ_U, and the subreflector projections onto the $x_s y_s$-plane and $y_s z_s$-plane.

A second code, VERIFY, was also derived from the aforementioned procedure. This code verifies that the dual offset configuration defined by the user has been optimized for minimum cross polarization (XPOL) according to Mizugutch and Rusch conditions. This is accomplished by numerically evaluating the left and right sides of (3.1) and (3.2) for the geometry specified by the user. Typical input and output parameters used in VERIFY are:

Input parameters required by VERIFY: D, F, H, α, β, e and f_s.

Output parameters: θ_E, α, β, e, c, f_s, d_c, ψ_C, ψ_L, ψ_U, and an evaluation of Mizugutch and Rusch conditions for the specified geometry.

Both codes create a data file that numerically describes the subreflector surface as a set of points defined with respect to the subreflector coordinate system $x_s y_s z_s$. This is a valuable feature especially when the subreflector is to be fabricated by a computerized machining process. This data file is also employed as the starting point for the shaping process described in Chapter 6. The far-field patterns can be computed by a suitable reflector analysis code, such as GRASP7. However, this is not required since the effectiveness of the codes has been confirmed through comparisons with measured data and extensive computer simulations with GRASP7. A few of these comparison studies are presented in Section 3.6. The codes OPTIMUM and VERIFY, together with the codes ROTATION and ECCENTRICITY described in

Chapter 5, form a complete suite of codes for the synthesis of non-conventional, low cross-polarized dual offset Gregorian reflector antennas. This suite of codes is herein referred to as the DORA package (Dual Offset Reflector Antennas Synthesis Package).

3.5 Use of the Same Sub-Optics Assembly with Different Main Reflectors

In this section, we comment on the problem of using the same feed and subreflector with different parabolic main reflectors. Our study indicates that it is possible to use the same sub-optics assembly if all the paraboloids have a similar F/D ratio. However, this is only true if the focal point of the parent ellipsoidal subreflector is placed at the same location as the focal point of the parent parabolic main reflector, and all of the orientation angles remain unchanged. This is illustrated by Fig. 3.4.

3.6 Numerical Results and Comments

In the following sections practical examples of single and dual reflector systems are employed to validate the design procedure discussed in Section 3.4 and implemented in the code OPTIMUM. The single reflectors correspond to real antenna systems commercialized by a major reflector antenna manufacturer. The measured patterns were provided by the manufacturer, and all computed patterns were obtained with the Virginia Tech code PRAC and the commercial code GRASP7. The dual configurations designed with OPTIMUM are the results of our efforts to upgrade the existing single reflectors to low cross-polarized dual reflector antennas.

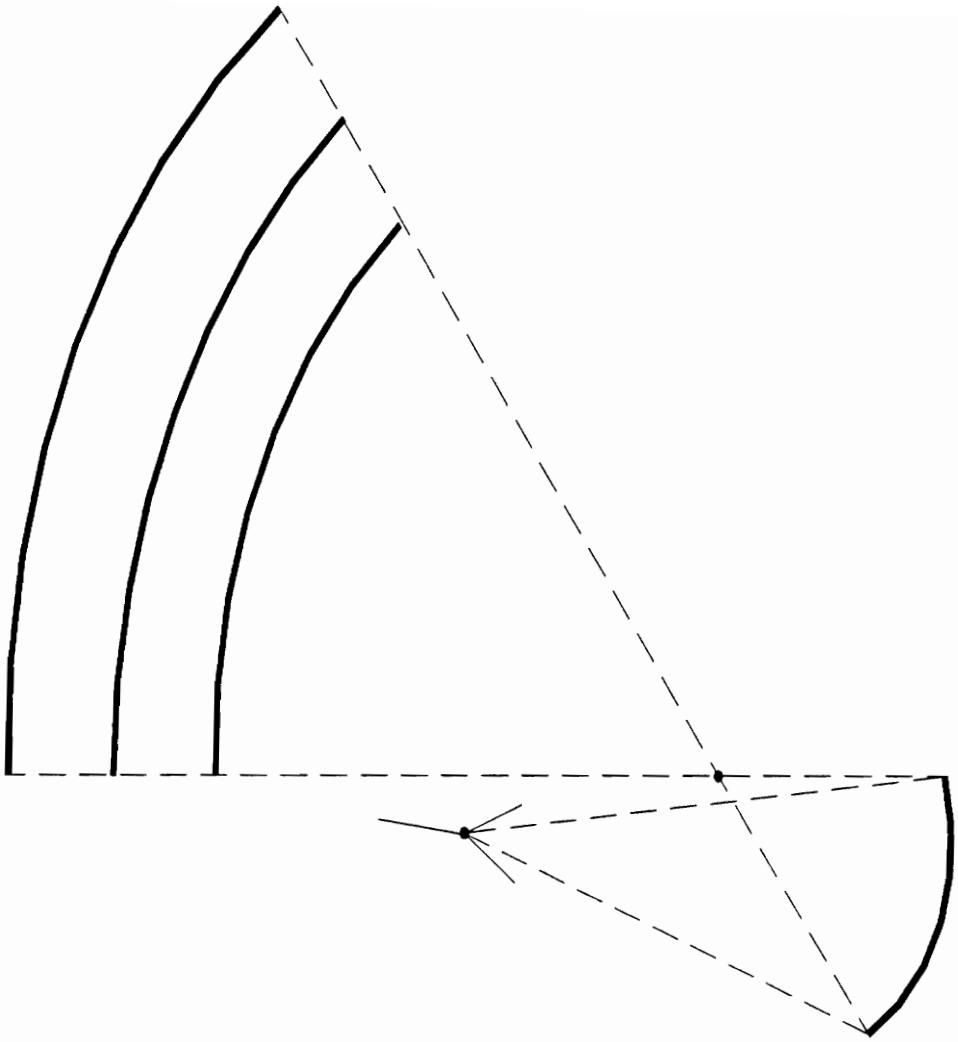

Figure 3.4. Use of the same sub-optics assembly with main reflectors of different projected aperture diameters but similar (F/D_p) ratios.

3.6.1 Single Offset Reflector System (Before Upgrading)

We start by examining the just fully offset configuration of Table 3.2. It is fed with an x_f-polarized feed that has a symmetric ("balanced") pattern similar to that in Fig. 2.2. The offset reflector choice corresponds to a 1.8-m diameter VSAT earth terminal antenna operating at 14.25 GHz. This is the 1.8-m reflector of a large commercial manufacturer of reflector antennas. If the feed remains pointed at the apex of the parent paraboloid (i.e., $\psi_f = 0°$), negligible XPOL is generated [4]; see Chapter 2. However, this leads to large spillover and associated gain loss. Therefore, in practice the feed is tilted such that its pattern peak is directed toward the central region of the reflector. This introduces high XPOL.

Figure 3.5 shows the computed co- and cross-polarized patterns and measured data for the offset parabolic reflector of Table 3.2 in the plane normal to the plane of symmetry (i.e., the yz-plane in Fig. 2.1). XPOL is expected to be maximum in this plane [4]. The patterns were computed using the commercial code GRASP7 [15] and the Virginia Tech code PRAC (Parabolic Reflector Analysis Code). PRAC is a user friendly code developed by the author to analyze axisymmetric and offset parabolic reflectors. PRAC evaluates the radiation integral (physical optics surface current integration) with the Jacobi-Bessel method [13, 14], and yields the co- and cross-polarized radiated fields with high accuracy and efficiency. A complete description of PRAC is given in Appendix B (Chapter 11). We note from Fig. 3.5 that both PRAC and GRASP yield almost identical results for this example; in addition, both are in very good agreement with the measured data [36, 37]. The measured gain is about 0.8 dB below the computed gain due to losses and system imbalances. Measured system XPOL is -22.00 dB, which compares well with the computed XPOL values of -21.27 dB from PRAC and -21.29 dB from GRASP7.

Table 3.2.

Geometrical Configuration and Performance Values for the Just Fully Offset Paraboloid

(a) Main Reflector Configuration			
Shape: Offset paraboloid			
Projected diameter (D), λ	85.5		
Parent reflector diameter (D_p), λ	171.0		
Focal length (F)	0.3048 D_p		
Offset of reflector center (H)	$D/2$		
(b) Feed Configuration	**Measured**	**PRAC**	**GRASP**
Polarization	Linear (x_f)	Linear (x_f)	Linear (x_f)
Pattern shape	—	$\cos^{4.57}$	Gaussian
Gain (G_f), dBi	—	13.07	13.13
10 dB beamwidth, degrees	≈78.00	78.00	78.00
Feed pointing angle (ψ_f), deg.	43.61	43.61	43.61
Edge Illum. (Lower,Upper), dB	(-12.0,-14.5)	(-12.8,-12.4)	(-12.5,-12.6)
(c) System Performance	**Measured**	**PRAC**	**GRASP**
Gain (G), dBi	46.78	47.59	47.52
Cross pol. level (XPOL), dB	-22.00	-21.27	-21.29
Side lobe level (SLL), dB	-23.50	-25.94	-26.40
Aperture efficiency (ϵ_{ap}), %	66.03	79.63	78.27

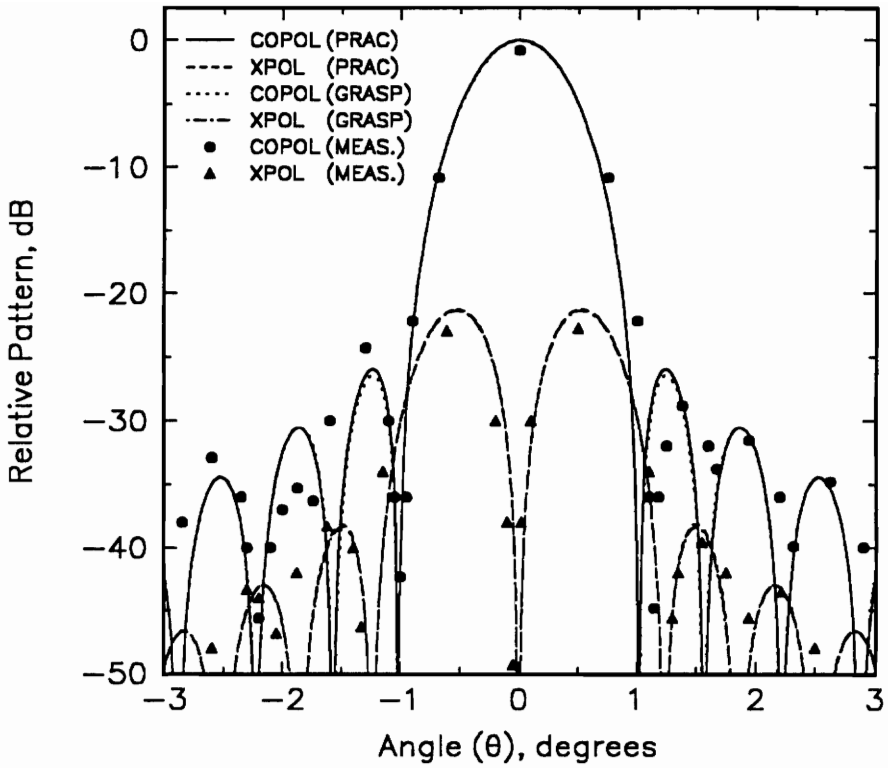

Figure 3.5. Radiation patterns of the 1.8-m single offset configuration specified in Table 3.2 (f = 14.25 GHz).

Aperture efficiency (ϵ_{ap}) was computed according to [12]

$$G = \epsilon_{ap}(\frac{\pi D}{\lambda})^2 \tag{3.16}$$

where G is the measured or computed gain of the reflector antenna, and D is the projected reflector diameter.

This example is typical of single offset reflectors, and indicates that single offset paraboloids illuminated by conventional feeds are limited by XPOL performance. In fact, this result is generic and well reported in the literature [3, 24, 25, 38]. A XPOL level of about -22 dB is often unacceptably high. In the next section we employ the program OPTIMUM to add an ellipsoidal subreflector to the just fully offset paraboloid example in order to form a low XPOL dual offset Gregorian configuration.

3.6.2 Dual Offset Reflector Systems (After Upgrading)

Dual offset reflector configurations can be designed for low geometrical optics XPOL when illuminated by a pure linearly polarized feed [16, 31]. Our goal is to upgrade the just fully offset reflector specified in Table 3.2 and discussed in Section 3.6.1 to a low cross-polarized, just fully offset Gregorian dual reflector antenna. This is accomplished by adding a concave ellipsoidal subreflector to the original single reflector system. The general geometry of a dual offset Gregorian antenna is presented in Fig. 3.2. Note that for the just fully offset case $H = D/2$.

The program OPTIMUM, described in Section 3.4, is applied to the just fully offset paraboloid of Table 3.2 to determine the corresponding low cross-polarized dual

configuration. The resulting configuration, referred to as the classical configuration, is listed in Table 3.3. Figure 3.6 shows the co- and cross-polarized patterns computed by GRASP7 for the classical dual Gregorian antenna of Table 3.3 in the plane normal to the plane of symmetry (i.e., the yz-plane in Fig. 3.2). XPOL is expected to be maximum in this plane [4, 33]. Table 3.3 also presents the performance values at 14.25 GHz computed with GRASP in the plane normal to the plane of symmetry (i.e., the yz-plane in Fig. 3.2). We note that XPOL is now -47.06 dB, more than 25 dB lower than the XPOL of the single configuration in Table 3.2.

Next, we use the same sub-optics assembly (i.e., subreflector and feed) specified in Table 3.3 with a 2.4-m diameter just fully offset paraboloid (f = 14.25 GHz), which is also part of the family of single reflector antennas offered by the aforementioned manufacturer. The resulting dual configuration is listed in Table Table 3.4. Note that the focal point of the parent ellipsoid is placed at the same location as the focal point of the parent paraboloid, and all of the orientation angles remain unchanged, as addressed in Section 3.5. The geometrical configuration is shown in Fig. 3.7. The associated prime-focus configuration presents a peak cross polarization level (XPOL) of -22.43 dB when illuminated by a pure linearly polarized feed, and therefore does not meet the XPOL requirement of -35 dB.

Figure 3.8 shows the co- and cross-polarized patterns computed by GRASP7 for the 2.4-m diameter dual offset Gregorian antenna of Table 3.4 in the plane normal to the plane of symmetry (i.e., the yz-plane in Fig. 3.2). Table 3.4 also lists the computed performance values. Aperture efficiency (ϵ_{ap}) was computed according to [12]. Note from Fig. 3.8 that low total system XPOL (-48.19 dB) was achieved using the classical design. However, when feed XPOL is included, the total system XPOL for the dual reflector will degrade; this is addressed in the next chapter.

Table 3.3.

Geometrical Configuration and Computed Performance Values for the 1.8-m Diameter Dual Offset Gregorian Reflector Antenna

(a) Main Reflector Configuration	
Shape	Offset paraboloid
Projected diameter (D), λ	85.5
Parent reflector diameter (D_p), λ	171.0
Focal length (F)	0.3048 D_p
Offset of reflector center (H)	$D/2$
(b) Subreflector Configuration	
Shape	Offset ellipsoid
Projected height (D_S), λ	14.1800
Parameter c of ellipse, λ	12.6340
Parameter f_s of ellipse, λ	9.9146
Eccentricity (e)	0.5603
Angle β, degrees	4.12
Angle θ_E, degrees	13.38
(c) Feed Configuration	
Polarization	Linear (x_f)
Pattern shape	Gaussian
Gain (G_f), dBi	22.30
11-dB beamwidth, degrees	26.76
Angle α, degrees	14.54
Angle γ, degrees	10.42
Distance d_c, λ	3.13
(d) System Performance (GRASP)	
Gain (G), dBi	47.21
Cross polarization level (XPOL), dB	-47.06
Side lobe level (SLL), dB	-24.37
Spillover loss, dB	0.51
Aperture efficiency (ϵ_{ap}), %	72.82

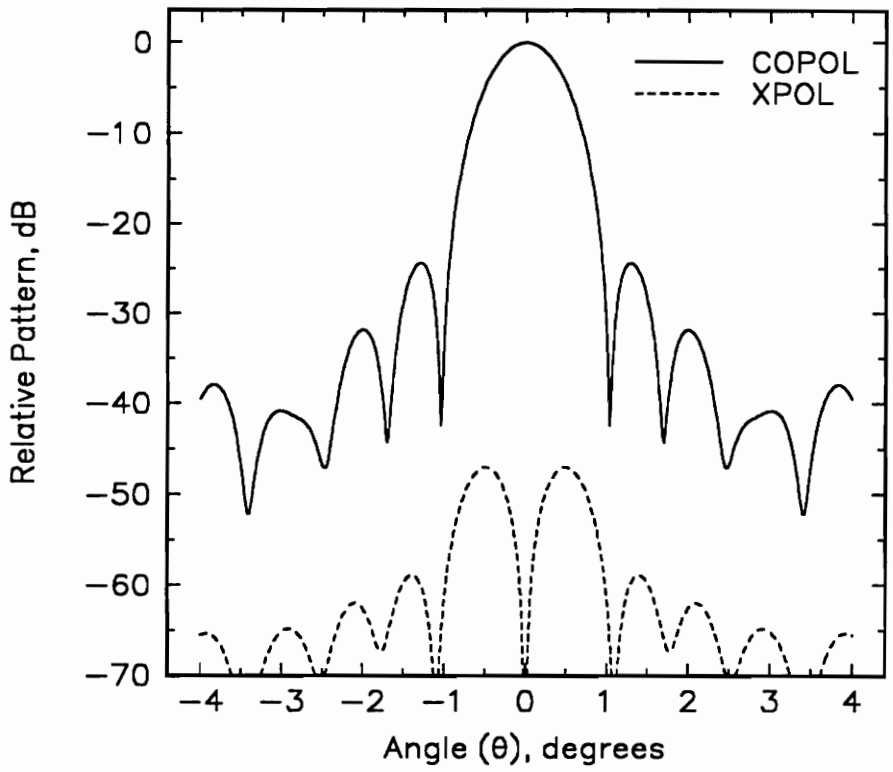

Figure 3.6. Computed co- (solid curve) and cross-polarized (dotted curve) far-field patterns of the dual offset Gregorian configuration specified in Table 3.3. The patterns were computed in the $\phi = 90°$ plane (i.e., the yz-plane in Fig. 3.2). The XPOL peak is 47.06 dB below the COPOL peak.

Table 3.4.

Geometrical Configuration and Computed Performance Values for the 2.4-m Diameter Dual Offset Gregorian Reflector Antenna

Main Reflector (paraboloid):

$D = 115.8240\ \lambda$

$D_p = 231.6480\ \lambda$

$F/D_p = 0.3048$

$\psi_C = 44.60°$

$\psi_U = 78.72°$

Subreflector (ellipsoid):

$D_S = 14.1800\ \lambda$

$c = 12.6340\ \lambda$

$f_s = 9.9146$

$e = 0.5603$

$\beta = 4.12°$

$\theta_E = 13.38°$

Feed (located at the focal point F_2):

Pattern shape = Gaussian (Fig. 4.1)

Gain G = 22.30 dBi

$\alpha = 14.54°$

$\gamma = 10.42°$

11 dB beamwidth = 26.76°

Polarization = Linear (x_f-directed)

XPOL = None

Computed Performance Values:

Gain (G), dBi	49.85
Cross polarization level (XPOL), dB	-48.19
Side lobe level (SLL), dB	-24.33
Spillover loss, dB	0.51
Aperture efficiency (ϵ_{ap}), %	72.96

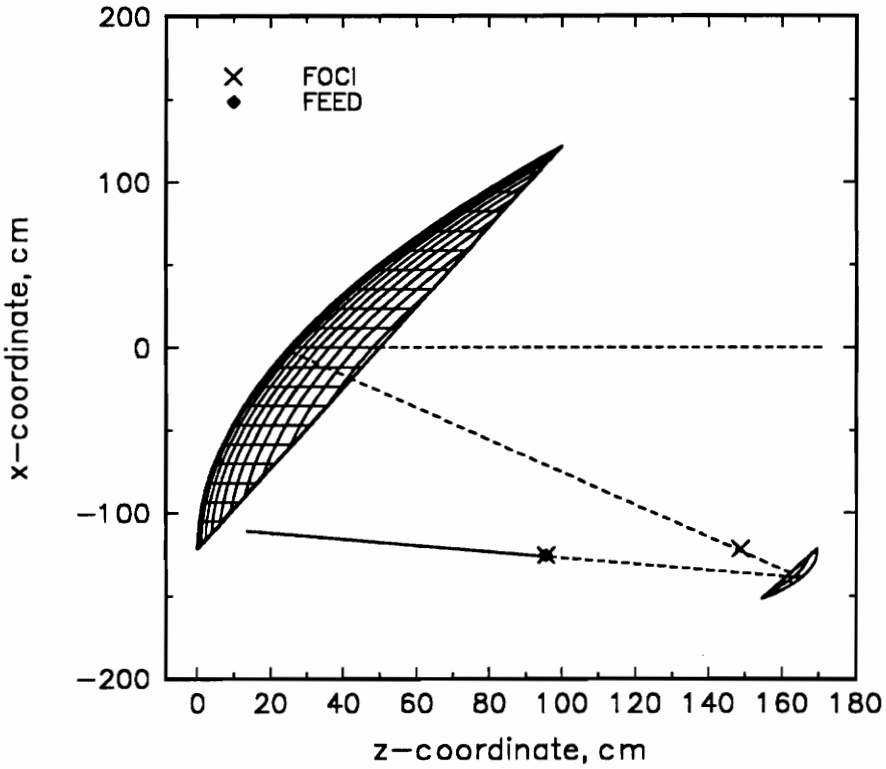

Figure 3.7. Geometry of the dual offset Gregorian reflector antenna specified in Table 3.4 (f = 14.25 GHz).

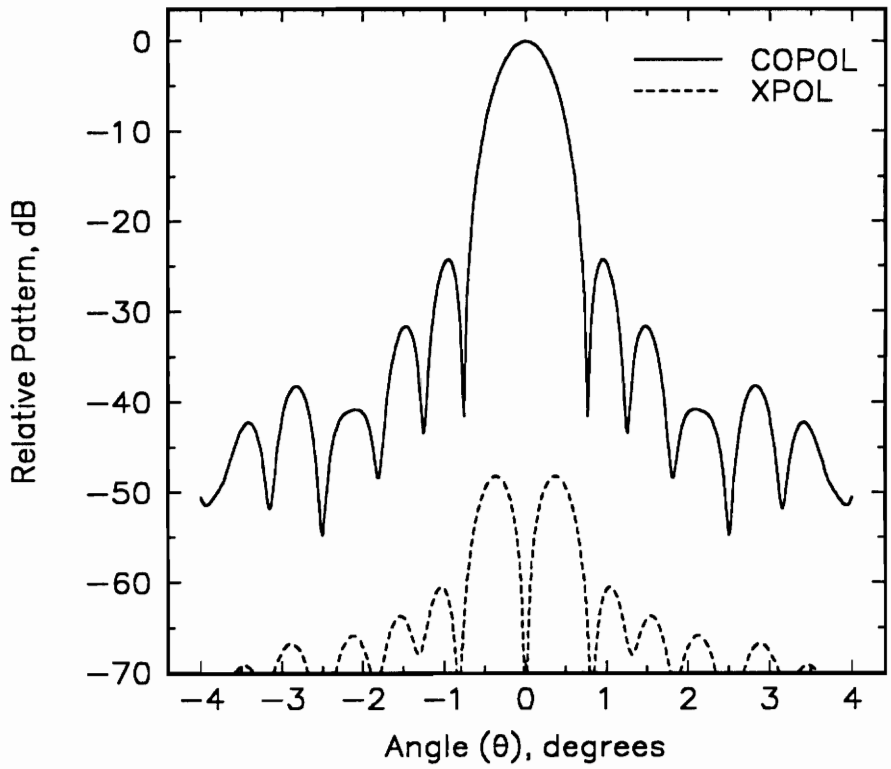

Figure 3.8. Computed co- (solid curve) and cross-polarized (dotted curve) far-field patterns of the dual offset Gregorian configuration specified in Table 3.4. The patterns were computed in the $\phi = 90°$ plane (i.e., the yz-plane in Fig. 3.2). The XPOL peak is 48.19 dB below the COPOL peak.

Finally, for completeness, we consider the same configuration of Table 3.4 illuminated with a right-handed circularly polarized (RHCP) feed. Figure 3.9 shows that circular XPOL is very low, -47.72 dB, and no beam squint is present. This confirms the conclusion presented in Section 2.5 that dual offset reflectors designed for low linear XPOL are free of circular XPOL and beam squint. In the next section we investigate XPOL sensitivity with respect to the orientation angles α and β.

3.6.3 Sensitivity Analysis

In this section we numerically investigate the sensitivity of gain and XPOL with respect to the orientation angles α and β; see Fig. 3.2 and Table 3.1 for definition of symbols. We choose the 2.4-m diameter, dual offset Gregorian antenna of Table 3.4 as the baseline configuration for this study. Our main goal is to determine how much the angles α and β can deviate from the values listed in Table 3.4 such that XPOL remains below -35 dB. In order to facilitate the investigation, we define the auxiliary angles α_d and β_d. These angles represent the deviation of α and β from the values listed in Table 3.4.

Figure 3.10 shows the behavior of gain as a function of α_d and β_d. All computer simulations were performed with the code GRASP7. Note that the point $\alpha_d = \beta_d = 0°$ represents the geometry of Table 3.4. Fig. 3.10 shows that gain deteriorates considerably as α_d and β_d are varied. This is due primarily to spillover loss. In addition, the main beam also scans off boresight as β_d is varied. The maximum gain of 49.85 dBi occurs for $\alpha_d = \beta_d = 0°$, confirming that the configuration of Table 3.4 has been optimized for minimum spillover loss; see Rusch condition (3.2).

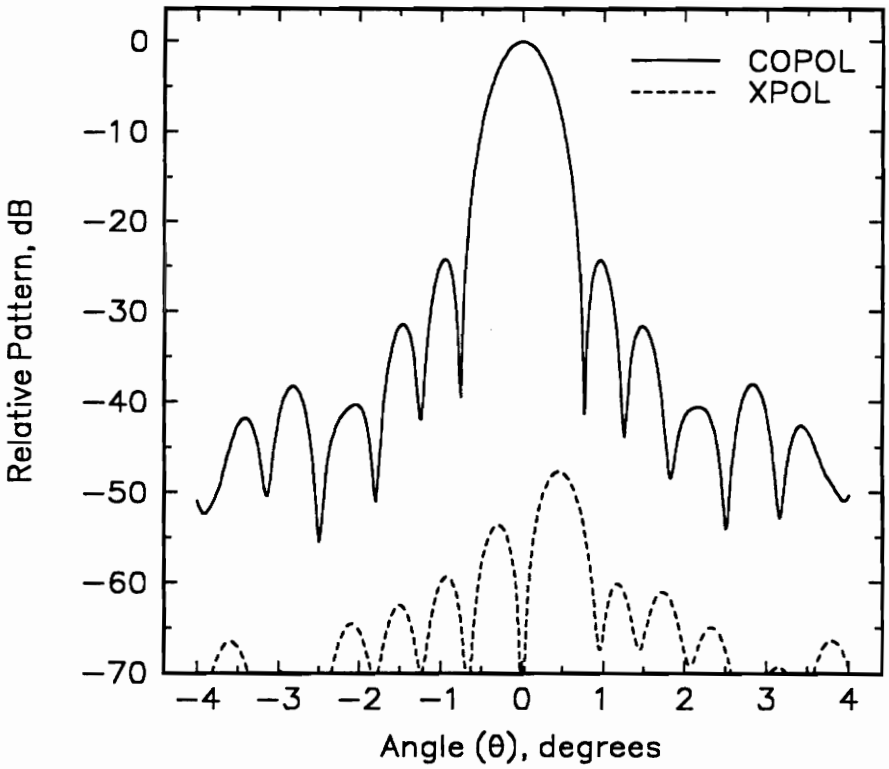

Figure 3.9. Computed co- (solid curve) and cross-polarized (dotted curve) far-field patterns of the dual offset Gregorian configuration specified in Table 3.4 illuminated by a RHCP feed. The patterns were computed in the $\phi = 90°$ plane (i.e., the yz-plane in Fig. 3.2). The circular XPOL peak is 47.72 dB below the COPOL peak.

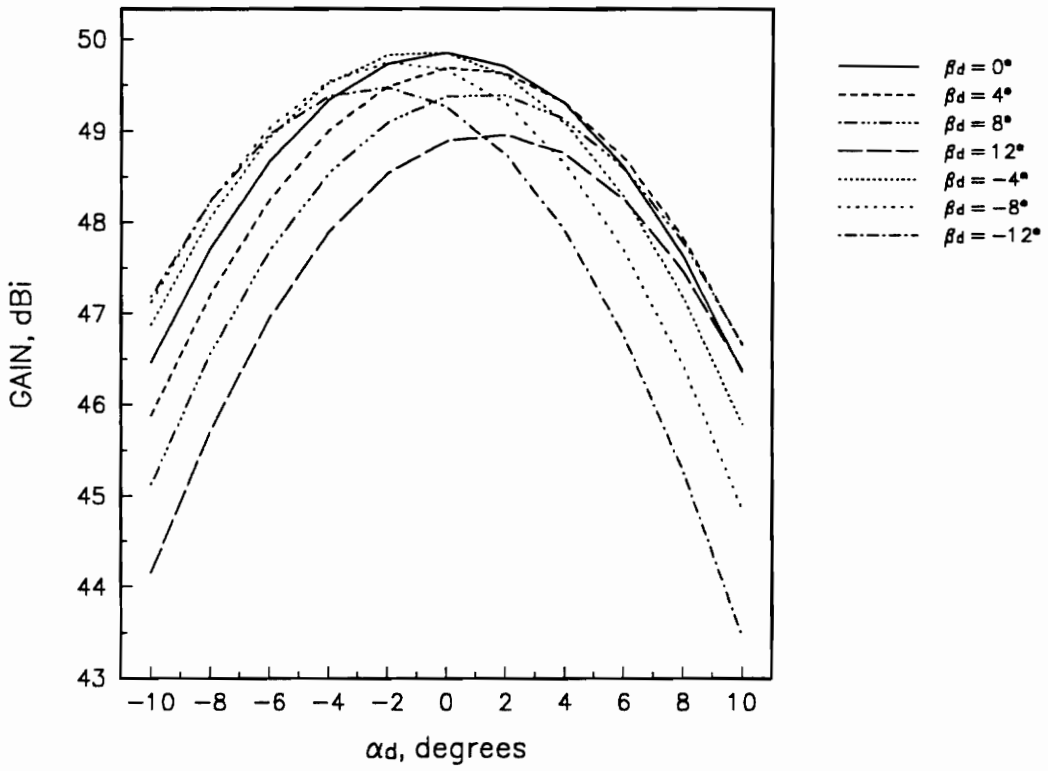

Figure 3.10. Gain as a function of the angles α_d and β_d for the 2.4-m diameter, dual offset Gregorian reflector antenna specified in Table 3.4.

Figure 3.11 shows the behavior of XPOL as a function of α_d and β_d. As in Fig. 3.10 the geometry of Table 3.4 was taken as the baseline configuration. Figure 3.11 shows that it is possible to achieve XPOL levels slightly below the one obtained with the configuration of Table 3.4 (i.e., -48.19 dB). However, there is an inherent penalty in gain, as shown by Fig. 3.10. According to Fig. 3.11, a XPOL level below -35 dB is obtained for values of α_d and β_d within the following ranges

$$-10^\circ \leq \alpha_d \leq 10^\circ \tag{3.17}$$

and

$$-5^\circ \leq \beta_d \leq 5^\circ \tag{3.18}$$

These values can be used to set the mechanical tolerance of the manufacturing process, if a XPOL level below -35 dB is desired.

We now investigate the sensitivity of XPOL with respect to frequency. Numerical simulations performed with GRASP7 show that the configuration of Table 3.4 has G = 42.11 dBi and XPOL = -40.59 dB at 6 GHz. In addition, the same configuration has G = 56.41 dBi and XPOL = -58.15 dB at 30 GHz. Therefore, we note that the XPOL behavior of the configuration of Table 3.4 is not very sensitive to frequency, remaining below -35 dB within a very large bandwidth (at least from 6 to 30 GHz). This is an expected result since the design procedure of Section 3.4 is frequency independent.

However, XPOL performance deteriorates at low frequencies (e.g., 2 GHz or below) due to diffraction effects. In order to assure effective designs, a subreflector size of at least 10 λ is recommended [32]. The upper limit of the operational

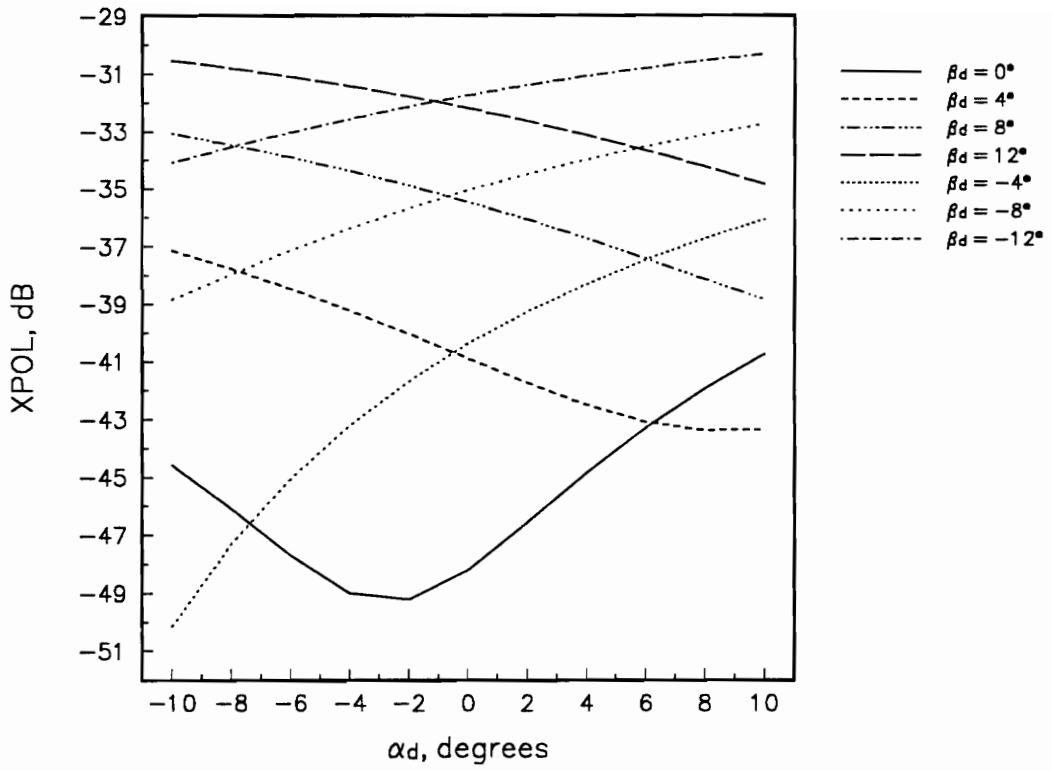

Figure 3.11. XPOL as a function of the angles α_d and β_d for the 2.4-m diameter, dual offset Gregorian reflector antenna specified in Table 3.4.

bandwidth is determined by the smoothness of the parabolic and ellipsoidal surfaces. Mechanical imperfections and surface distortions can introduce phase errors at high frequencies and degrade overall performance. In practice, the operational bandwidth of a reflector system is set by the bandwidth of the feed antenna used to illuminate the reflector(s). Although illustrated for the configuration of Table 3.4, these conclusions are generic and can be extended to other configurations.

3.7 Conclusions

A general algorithm was presented for upgrading single offset reflectors to dual reflector configurations to achieve low cross polarization. The problem consists of adding a subreflector to an existing family of offset paraboloids in order to achieve a low level of linear cross polarization (e.g., -35 dB). The feed can be polarized along the x_f- or y_f-direction. In addition, the resulting configuration operates with either a LP or a CP feed without the need of being repositioned (no substantial beam squint). In the next few chapters, we take into account the feed cross polarization effects and impose practical constraints for the low-cost production of dual offset Gregorian reflector antennas. General procedures to minimize XPOL under those circumstances will be introduced.

Chapter 4

Influence of Feed XPOL on System XPOL and the Feed Rotation Technique

4.1 Introduction

In the last chapter we investigated the addition of a subreflector to an existing offset parabolic reflector to reduce cross polarization level. Since the proposed problem is motivated by practical applications, cross polarization effects of conventional, low-cost feeds must be accounted for in the analysis. In this chapter the influence of the feed cross polarization (XPOL) is examined in detail. A model for predicting the total system XPOL due to the reflectors and feed is presented and discussed. In addition, a new technique to reduce the feed XPOL effects of a certain class of feed antennas is introduced. The theoretical procedures are confirmed with practical configuration examples analyzed with the commercial code GRASP7 [15].

4.2 Simple Feed Model

In all computer simulations presented in this chapter the feed co-polarized pattern was modeled using the symmetric ("balanced") Gaussian radiation pattern shown in Fig. 4.1, which has a 11-dB beamwidth of 26.76°; see Section 2.2.2 for further information on balanced feeds. In addition, the computer simulations employed the cross-polarization feed pattern of Fig. 4.1, which has a peak of -32 dB. This value was obtained from measured data of a typical low-cost, conical corrugated horn used to illuminate commercial reflector systems. The data were provided by a major reflector antenna manufacturer.

The theoretical feed model shown in Fig. 4.1 was obtained by combining the x_f- and y_f-polarized feed models described in Section 2.2.2; see the same section for CP feed models. Assuming that the main polarization is along the x_f-direction, the co- and cross-polarized feed patterns are given by [15]

$$\vec{E}_{\text{co}}(\vec{r}_f) = C(\theta_f)\,[\hat{\theta}_f\,\cos\phi_f - \hat{\phi}_f\,\sin\phi_f]\,\frac{e^{-\jmath\beta r_f}}{r_f} \tag{4.1}$$

and

$$\vec{E}_{\text{cross}}(\vec{r}_f) = p_r\,C(\theta_f)\,[\hat{\theta}_f\,\sin\phi_f + \hat{\phi}_f\,\cos\phi_f]\,\frac{e^{-\jmath\beta r_f}}{r_f} \tag{4.2}$$

where $C(\theta_f)$ is the Gaussian model of (2.10) and p_r is the complex polarization ratio defined as

$$p_r = \text{XPOL}_F\,[\cos\delta + \jmath\sin\delta] \tag{4.3}$$

The quantity XPOL_F determines the feed XPOL peak relative to the peak co-polarized beam. During this investigation various values were used for the difference in phase δ between the cross- and co-polarized feed patterns defined as

$$\delta = \text{PHASE}\{\text{XPOL}_F\} - \text{PHASE}\{\text{COPOL}_F\} \tag{4.4}$$

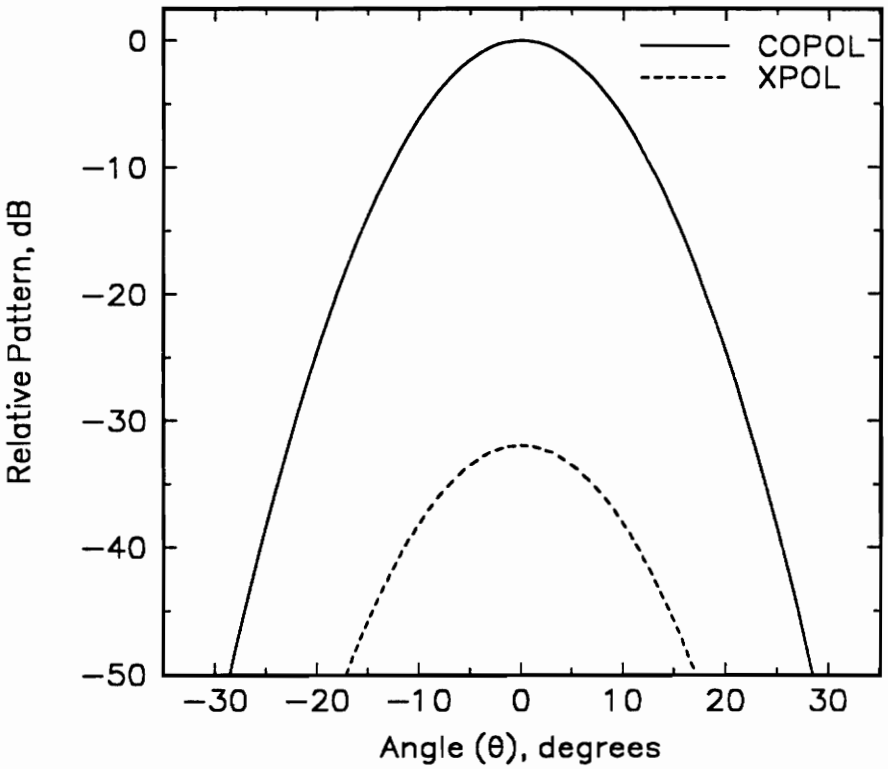

Figure 4.1. Gaussian feed pattern used for studying reflector performance. The 11-dB beamwidth of the co-polarized pattern (COPOL) is 26.76° and the cross-polarized pattern (XPOL) peak is 32 dB below the COPOL peak.

4.3 Influence of Feed XPOL on System XPOL

4.3.1 System XPOL Prediction Model

The degrees of freedom available to reduce feed XPOL effects without altering the feed are the subreflector shape and the relative positions and orientations of the reflectors and feed. However, before we attempt to reduce feed XPOL, it is necessary to understand its influence from a system point of view. A simple approximate model for predicting the influence of feed XPOL in reflector systems is the worst case formula of [17]:

$$\mathrm{XPOL}_S = \mathrm{XPOL}_F + \mathrm{XPOL}_R \tag{4.5}$$

where XPOL_S, XPOL_F, and XPOL_R, are the cross polarization levels of the total system, the feed (on-axis), and the dual reflector antenna alone (peak), respectively. XPOL here is expressed as a field ratio and dB values can be converted using $10^{\frac{\text{Value in dB}}{20}}$. Note that (4.5) is similar to the relation for two parallel admittances [17]. It was developed to evaluate system XPOL in a transmit/receive link, but gives approximate results for this situation. In fact, extensive computer simulations performed with the commercial code GRASP7 [15] showed that (4.5) predicts well the total system XPOL. The simple result in (4.5) shows that either the feed or the reflector XPOL can dominate the system XPOL. Since classical designs using (3.1) and (3.2) yield low LP reflector XPOL, system XPOL is usually limited by feed XPOL. Deterioration of system XPOL due to feed XPOL has been noted previously in the literature, but no attempts for its prediction have been reported [39, 40].

4.3.2 Numerical Results and Comments

As an example we consider the 2.4-m diameter dual offset Gregorian reflector of Table 3.4, Section 3.6.2. When a typical feed XPOL value of -32 dB is included through the feed pattern in Fig. 4.1, the XPOL computed by GRASP7 increases from -48.19 dB (Fig. 3.8) to -31.75 dB, as shown in Fig. 4.2. Equation (4.5) yields -30.75 dB, which is in good agreement for such a simple formula. In addition, (4.5) predicts that a feed with a XPOL level of at least -37.15 dB is required to achieve the system XPOL goal of -35 dB with the example reflector configuration.

These results confirm that the classical dual reflector system is XPOL performance limited by the feed. In the remaining sections we consider a technique for reducing system XPOL.

4.4 XPOL Improvement by Feed Rotation

4.4.1 Analytical Formulation

A simple procedure that might reduce the effects of feed XPOL is rotation of the feed about its axis. This is investigated in the present section and, as we will shown, it is an effective means for reducing system XPOL. The angle about the feed z_f-axis, ϕ_f, is positive for a clockwise rotation viewed looking toward the feed; see Fig. 3.2. The theoretical feed model of Fig. 4.1 is used and, while it may not be completely realistic, it illustrates that the rotation technique can be useful in some applications.

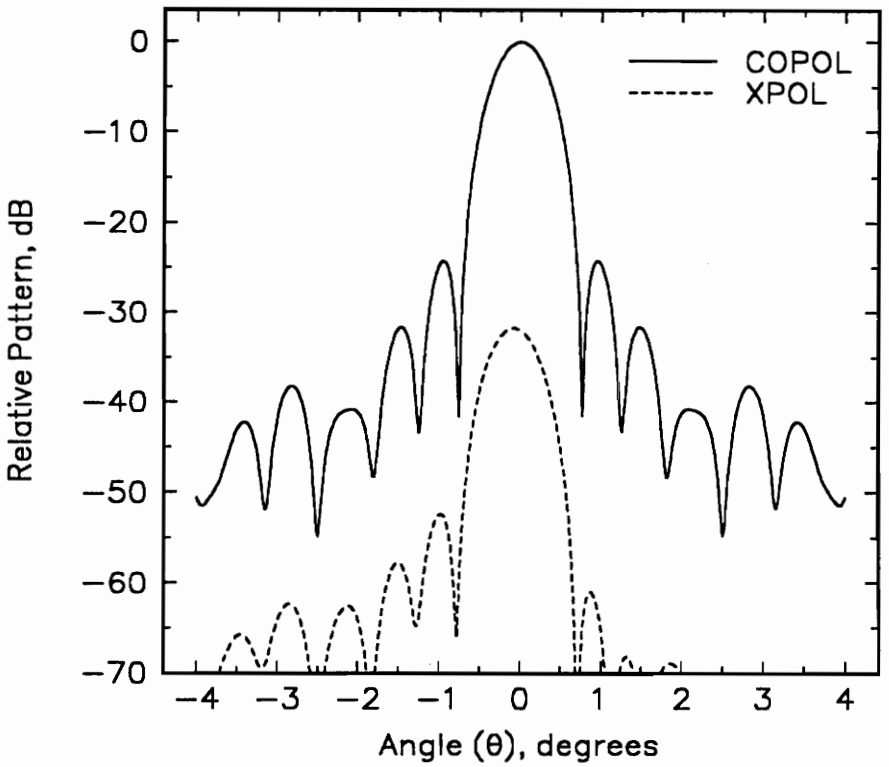

Figure 4.2. Computed co- (solid curve) and cross-polarized (dotted curve) far-field patterns of the dual offset Gregorian configuration specified in Table 3.4 with the feed pattern of Fig. 4.1 ($\delta = 0°$). The patterns were computed in the $\phi = 90°$ plane (i.e., the yz-plane in Fig. 3.2). Note that XPOL is high, -31.75 dB, due to the feed XPOL effects.

We start by expressing the fields (4.1) and (4.2) with relation to a rotated coordinate system (r'_f,θ'_f,ϕ'_f). The primed coordinate system is obtained by rotating the feed coordinate system (r_f,θ_f,ϕ_f) about the z_f-axis by an angle α. If the prime superscripts are dropped, this is equivalent to illuminating the subreflector with a feed antenna rotated about the z_f-axis by an angle $-\alpha$. The Eulerian angle α is defined in the Appendix A, Section 10.3. Thus, (4.1) and (4.2) are expressed with respect to (r'_f,θ'_f,ϕ'_f) in component form as

$$\begin{bmatrix} E_{r'_f}(\vec{r_f}') \\ E_{\theta'_f}(\vec{r_f}') \\ E_{\phi'_f}(\vec{r_f}') \end{bmatrix} = \begin{pmatrix} \sin\theta'_f\cos\phi'_f & \sin\theta'_f\sin\phi'_f & \cos\theta'_f \\ \cos\theta'_f\cos\phi'_f & \cos\theta'_f\sin\phi'_f & -\sin\theta'_f \\ -\sin\phi'_f & \cos\phi'_f & 0 \end{pmatrix} \begin{pmatrix} \cos\alpha & \sin\alpha & 0 \\ -\sin\alpha & \cos\alpha & 0 \\ 0 & 0 & 1 \end{pmatrix}$$

$$\begin{pmatrix} \sin\theta_f\cos\phi_f & \cos\theta_f\cos\phi_f & -\sin\phi_f \\ \sin\theta_f\sin\phi_f & \cos\theta_f\sin\phi_f & \cos\phi_f \\ \cos\theta_f & -\sin\theta_f & 0 \end{pmatrix} \begin{bmatrix} 0 \\ E_{\theta_f}(\vec{r_f}) \\ E_{\phi_f}(\vec{r_f}) \end{bmatrix} \quad (4.6)$$

which yields

$$\begin{bmatrix} E_{r'_f}(\vec{r_f}') \\ E_{\theta'_f}(\vec{r_f}') \\ E_{\phi'_f}(\vec{r_f}') \end{bmatrix} = \begin{pmatrix} \sin\theta'_f\cos\phi'_f[I_1\cos\alpha + I_2\sin\alpha] + \\ \qquad \sin\theta'_f\sin\phi'_f[-I_1\sin\alpha + I_2\cos\alpha] + I_3\cos\theta'_f \\ \cos\theta'_f\cos\phi'_f[I_1\cos\alpha + I_2\sin\alpha] + \\ \qquad \cos\theta'_f\sin\phi'_f[-I_1\sin\alpha + I_2\cos\alpha] - I_2\sin\theta'_f\cos\alpha \\ -\sin\phi'_f[I_1\cos\alpha + I_2\sin\alpha] + \cos\phi'_f[-I_1\sin\alpha + I_2\cos\alpha] \end{pmatrix} \quad (4.7)$$

where

$$
\begin{aligned}
I_1 &= E_{\theta_f}(\vec{r_f})\cos\theta_f\cos\phi_f - E_{\phi_f}(\vec{r_f})\sin\phi_f \\
I_2 &= E_{\theta_f}(\vec{r_f})\cos\theta_f\sin\phi_f + E_{\phi_f}(\vec{r_f})\cos\phi_f \\
I_3 &= E_{\theta_f}(\vec{r_f})\sin\theta_f
\end{aligned}
\tag{4.8}
$$

Assuming that the main polarization is along the x'_f-direction, the co- and cross-polarized fields can be obtained from (4.7) through the relations

$$
\begin{aligned}
&\vec{E}(\vec{r_f}') = \hat{r}'_f\, E_{r'_f}(\vec{r_f}') + \hat{\theta}'_f\, E_{\theta'_f}(\vec{r_f}') + \hat{\phi}'_f\, E_{\phi'_f}(\vec{r_f}') \\
&E_{\mathrm{co}}(\vec{r_f}') = \vec{E}(\vec{r_f}')\bullet\hat{a}_{co} = \\
&\quad = \vec{E}(\vec{r_f}')\bullet[\hat{\theta}'_f\cos\phi'_f - \hat{\phi}'_f\sin\phi'_f] = E_{\theta'_f}(\vec{r_f}')\cos\phi'_f - E_{\phi'_f}(\vec{r_f}')\sin\phi'_f \\
&E_{\mathrm{cross}}(\vec{r_f}') = \vec{E}(\vec{r_f}')\bullet\hat{a}_{cross} = \\
&\quad = \vec{E}(\vec{r_f}')\bullet[\hat{\theta}'_f\sin\phi'_f + \hat{\phi}'_f\cos\phi'_f] = E_{\theta'_f}(\vec{r_f}')\sin\phi'_f + E_{\phi'_f}(\vec{r_f}')\cos\phi'_f
\end{aligned}
\tag{4.9}
$$

Setting $|E_{\mathrm{cross}}|$ to zero yields the relation

$$
\begin{aligned}
&|I_1\sin\phi'_f\cos\phi'_f\cos\alpha(1-cos\theta'_f) + I_2\sin\phi'_f\cos\phi'_f\sin\alpha(1-cos\theta'_f) + \\
&I_2\sin\theta'_f\sin\phi'_f\cos\alpha + (I_1\sin\alpha - I_2\cos\alpha)(\sin^2\phi'_f\cos\theta'_f + \cos^2\phi'_f)| = 0
\end{aligned}
\tag{4.10}
$$

Simplification of (4.10) is possible for angles close to boresight; i.e., $\theta'_f \approx 0°$. Then $\cos\theta'_f \approx 1$ and $\sin\theta'_f \approx 0$, and (4.10) reduces to

$$
|\tan\alpha - \frac{C(\theta_f)[\cos\phi_f + p_r\sin\phi_f]\cos\theta_f\sin\phi_f + C(\theta_f)[p_r\cos\phi_f - \sin\phi_f]\cos\phi_f}{C(\theta_f)[\cos\phi_f + p_r\sin\phi_f]\cos\theta_f\cos\phi_f - C(\theta_f)[p_r\cos\phi_f - \sin\phi_f]\sin\phi_f}| = 0
\tag{4.11}
$$

where $E_{\theta_f}(\vec{r_f})$ and $E_{\phi_f}(\vec{r_f})$ were obtained from (4.1) and (4.2). For angles close to boresight we also have $\cos\theta_f \approx 1$ and $\sin\theta_f \approx 0$. Then

$$|\tan\alpha - p_r| = 0 \qquad \text{for angles close to boresight} \tag{4.12}$$

Using (4.3) we arrive at

$$\sqrt{(\tan\alpha - \text{XPOL}_F\ \cos\delta)^2 + (-\text{XPOL}_F\ \sin\delta)^2} = 0 \tag{4.13}$$

which yields

$$\alpha = \tan^{-1}[\text{XPOL}_F\ \cos\delta] \tag{4.14}$$

and

$$\text{XPOL}_F = 0 \qquad \text{or} \qquad \delta = 0^\circ \tag{4.15}$$

From (4.15) we see that on-axis feed XPOL is completely canceled via (4.14) only for $\delta = 0^\circ$. However, if we relax the condition of zero feed XPOL to very low feed XPOL, some reduction is still possible for $\delta \neq 0^\circ$. In fact, we investigate in the next section how much δ can deviate from 0° such that the total system XPOL remains below -35 dB. It is assumed in our analysis that XPOL_F is small (e.g., $\text{XPOL}_F = -32$ dB), which satisfies (4.15) in an approximate fashion even for $\delta \neq 0^\circ$. Within this context, the maximum possible reduction for any value of δ is obtained with a rotation given by (4.14).

As mentioned before, if the prime superscripts of (4.7) and (4.9) are dropped, the described procedure is equivalent to illuminating the subreflector with a feed antenna rotated about the z_f-axis by an angle $-\alpha = \phi_f$; see Fig. 3.2 and Table 3.1. Thus, the angle that yields minimum XPOL, $\phi_f = \phi_{fX}$, is given in an approximate fashion by

$$\phi_{fX} = \tan^{-1}(\text{XPOL}_F \cos\delta) \tag{4.16}$$

4.4.2 Numerical Results and Comments

As an example, consider the classical reflector configuration specified in Table 3.4 illuminated by the feed modeled as in Fig. 4.1 and presenting -32 dB of XPOL with $\delta = 0°$. Rotating the feed as in (4.16) yields $\phi_{fX} = 1.44°$. Physical optics analysis for this configuration with $\phi_f = \phi_{fX}$ yields a cross polar level of -48.17 dB over the main lobe and near-in sidelobes, as shown by Fig. 4.3. This represents a reduction of more than 16 dB from XPOL = -31.75 dB, prior to the rotation. In order to confirm that Fig.4.3 contains the peak cross polar value, the cross polar contour plot is shown in Fig.4.4. We note that XPOL has a peak value of -48.17 dB at the u = 0 cut (i.e., $\phi = 90°$), which is exactly the pattern cut showed by Fig.4.3. Thus, system XPOL has been reduced to a satisfactory level by means of the feed rotation. Also, for this case, the gain loss due to the polarization mismatch introduced by the feed rotation was negligible. It is worth noting that system XPOL is very sensitive to the amount of rotation and ϕ_{fX} must be achieved accurately for good cancellation of feed XPOL.

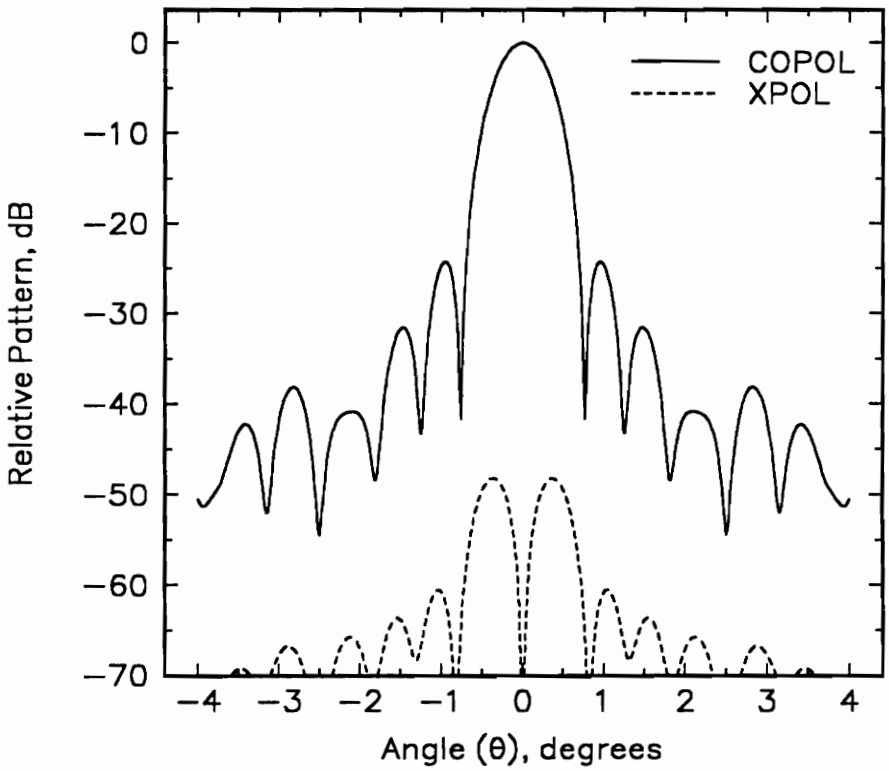

Figure 4.3. Computed co- (solid curve) and cross-polarized (dotted curve) far-field patterns of the dual offset Gregorian configuration specified in Table 3.4 with the feed pattern of Fig. 4.1 ($\delta = 0°$). The patterns were computed in the $\phi = 90°$ plane (i.e., the yz-plane in Fig. 3.2). Note that system XPOL has been reduced to a satisfactory level by means of the feed rotation ($\phi_f = 1.44°$).

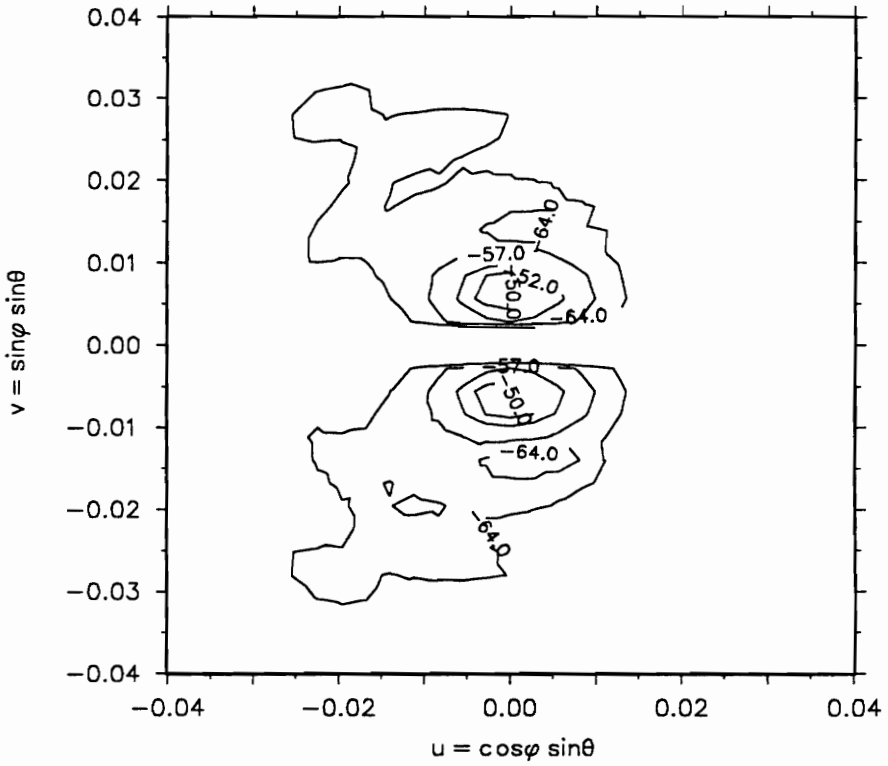

Figure 4.4. Contour plot (dB) of the computed cross-polarized pattern of the dual offset Gregorian reflector antenna specified in Table 3.4 with the feed antenna rotated by $\phi_f = 1.44°$ ($\delta = 0°$). Note that the peak cross polar level of -48.17 dB lies in the u = 0 cut (i.e., $\phi = 90°$), which is exactly the pattern cut shown by Fig. 4.3.

We next investigate the sensitivity of system XPOL to phase δ. Equation (4.16) shows that as δ approaches $\pm 90°$, ϕ_{fX} approaches 0°. In other words, no XPOL reduction is possible by means of feed rotation when the cross-polar field is in phase quadrature with the co-polar field ($\delta = \pm 90°$). This is because when the co-polar component reaches a peak value, the cross-polar component is zero (or vice-versa), and no cancellation can be achieved. This is the reason why the feed rotation technique cannot be used with single offset reflectors. XPOL introduced by reflection on the reflector surface is always 90° out of phase from the main polarization [24]. On the other hand, with a properly designed dual offset system, the cross-polar components introduced by the two reflections cancel each another, and the only remaining substantial XPOL is due to the feed. Thus, feed rotation can be used to reduce system XPOL of an offset dual reflector. The rotation procedure yields a system bandwidth that is limited only by the variations of the feed pattern with frequency.

The specific design goal of the example is to achieve a system XPOL below -35 dB using the configuration of Table 3.4 and the feed model of Fig. 4.1 (i.e., XPOL_F = -32 dB). Computer simulations performed with GRASP7 [15] showed that this goal is met with feed rotation if the phase is confined to the following range:

$$-45.00° \leq \delta \leq 45.00° \tag{4.17}$$

The required feed rotation ϕ_{fX} determined by (4.16) for the limiting cases of $\delta = \pm 45.00°$ is 1.02°.

Figure 4.5 shows the computed co- and cross-polarized patterns for the configuration of Table 3.4 illuminated by a feed rotated by $\phi_f = 1.02°$ and with $\delta = 45.00°$. The peak cross polarization level according to Fig. 4.5 is -35.01 dB. Although not shown, the same XPOL level was obtained with $\delta = -45.00°$ for the same amount of feed rotation. In addition, we note that the feed can be rotated in the opposite direction (negative angles ϕ_{fX}) if the phase is within the range $135.00° \leq \delta \leq 225.00°$.

If the feed pattern is essentially different than the one presented in Fig. 4.1 (e.g., a pattern that is not symmetric or "balanced"), a possible solution is to shape the subreflector in order to minimize feed XPOL effects. This problem is analyzed in detail in Chapter 6. Herein, we only considered canonical (i.e., non-shaped) reflectors in order to assure broad operational bandwidths. The next chapter includes the constraint of producing a design with suitable clearance between the main reflector and feed axis. The enforcement of this constraint leads to deterioration of system XPOL in our study configuration. In order to minimize that effect, the technique of replacing the subreflector by one of higher eccentricity is introduced.

4.5 Conclusions

It was shown that the XPOL of dual offset Gregorian antennas designed for low XPOL is generally limited by the feed XPOL. Equation (4.5) can be used to determine the minimum feed XPOL level necessary to achieve a required specification of system XPOL. Nevertheless, a suitable computer code should be used to validate the electrical performance values.

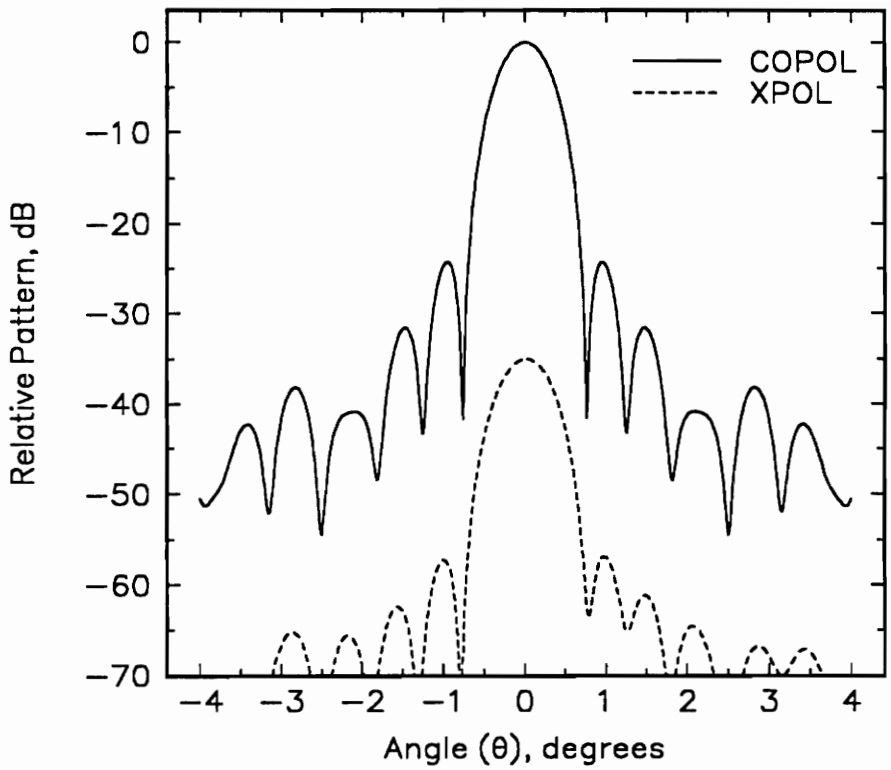

Figure 4.5. Computed co- (solid curve) and cross-polarized (dotted curve) far-field patterns of the dual offset Gregorian configuration specified in Table 3.4 with the feed pattern of Fig. 4.1 ($\delta = 45°$). The patterns were computed in the $\phi = 90°$ plane (i.e., the yz-plane in Fig. 3.2.). Note that system XPOL has been reduced to a level below -35 dB by means of the feed rotation ($\phi_f = 1.02°$).

The possibility of reducing feed XPOL by rotating the feed was investigated in detail. The procedure was effective for the feed model considered in Section 4.3. Although this feed model may not be completely realistic, it illustrates that the rotation can be useful in some applications. It should be mentioned that it is possible to compensate for a certain amount of feed XPOL through the shaping of both the main reflector and the subreflector [40]. The possibility of shaping only the subreflector to reduce the influence of XPOL effects caused by feed antennas with XPOL characteristics different than the ones considered in Section 4.2 is investigated in Chapter 6. A synthesis procedure based on the gradient method [41, 42] is presented to assure effective designs (i.e., designs that meet the specifications and constraints herein presented). Numerical simulations confirm the viability of the process, although some pattern deterioration and narrowing of operational bandwidth can be experienced due to the introduction of phase errors.

In the next chapter we investigate system XPOL reduction while enforcing practical constraints for the mass production of dual offset Gregorian reflector antennas. A procedure to rotate the parent ellipsoidal subreflector is introduced. That is necessary to achieve clearance between the bottom of the main reflector and the feed axis. Manufacturing costs can be substantially reduced through the enforcement of this condition. However, the rotation of the subreflector introduces substantial XPOL in a system designed to present low XPOL. The proposed solution is to replace the subreflector by one of higher eccentricity, producing a design with the desired XPOL performance and suitable clearance between the main reflector and feed axis. Also, the resultant design presents large operational bandwidth since the feed was relocated to the focal point of the new ellipsoidal subreflector, avoiding the introduction of phase errors.

Chapter 5

XPOL Reduction with Practical Constraints

5.1 Introduction

In this chapter practical manufacturing constraints for large scale production are imposed on low cost dual offset Gregorian antennas. In particular, designs for adequate clearance between the bottom of the main reflector and the feed axis are investigated. This constraint is not taken into account by other design procedures and is not addressed in the open literature. New procedures to enforce the aforementioned constraint while keeping system XPOL below -35 dB are developed in a generic analytical form and applied to practical case examples. Computer simulations are employed to validate the design algorithms.

In addition, we evaluate the performance of the largest steerable dish antenna in the world, the Green Bank Radio Telescope (GBT), located in Green Bank, West Virginia. We first upgrade its 100-m diameter, single offset main reflector to a low cross-polarized dual offset Gregorian antenna based on the Virginia Tech code DORA, developed by the author. The geometrical parameters determined with

DORA are in very good agreement with those published in [7]. New designs can be obtained with DORA if the subreflector size is changed. All designs are optimized for low cross polarization. The GBT dual configuration is a good example of a dual offset Gregorian antenna not employing a just fully offset paraboloid as the main reflector. The possibility of imposing the practical constraints addressed in this dissertation on the GBT case example is discussed in detail.

5.2 Feed Region Clearance

As commented in Chapter 1, cost effective designs often require that an existing single offset reflector mold be used to construct the main reflector of a dual configuration. Many such molds are for just fully offset geometries. This in turn leads to a dual reflector configuration that is Gregorian with the feed axis z_f intersecting the main reflector; see Fig. 3.1 and Section 3.2 for further information. The same problem may also occur in certain Gregorian configurations even when the main reflector is not just fully offset. It is desirable that the final design provide suitable clearance between the bottom of the main reflector and the feed axis in order to access the feed antenna with a straight section of waveguide, thus reducing the complexity and cost of the mechanical structure. In general, the distance d_c between the projection of the bottom of the main reflector (point L_p in Fig. 3.2) and the feed axis displacement from the reflector axis (s) as shown in Fig. 5.1 is given by

$$d_c = d_a - (H - D/2) = F\tan\gamma - 2c\,(\sin\beta + \cos\beta\tan\gamma) - (H - D/2) \qquad (5.1)$$

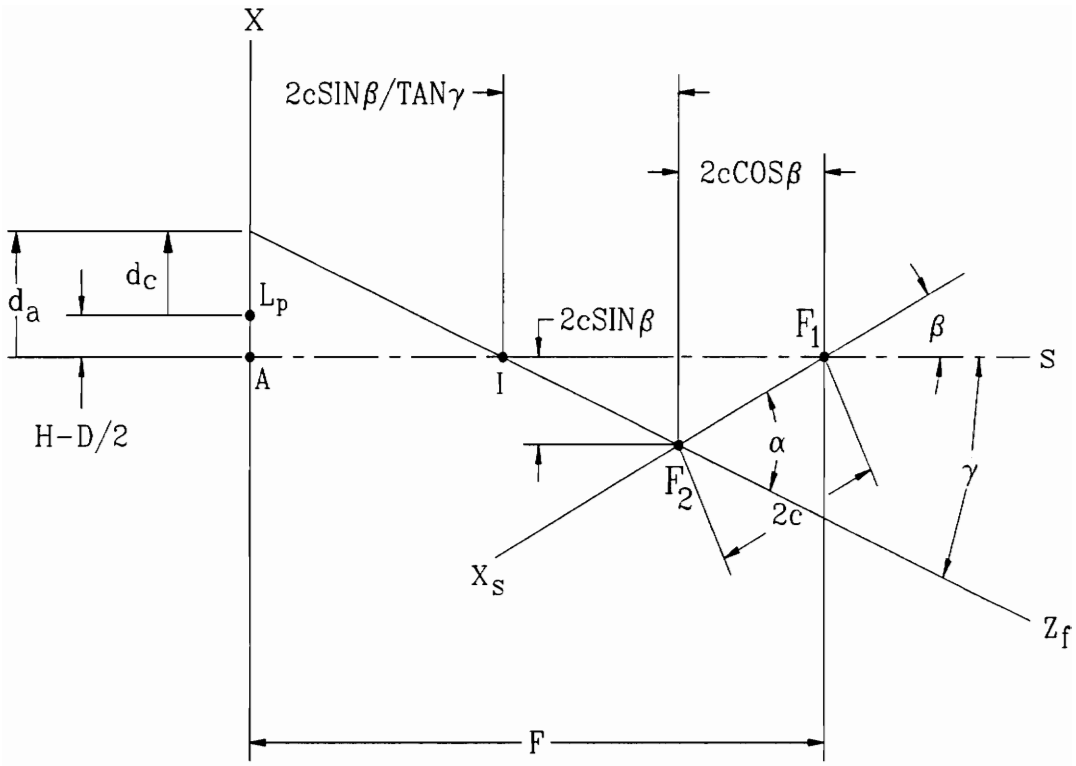

Figure 5.1. Geometrical determination of the distance d_c.

All symbols are defined in Table 3.1. The angle γ is related to α and β as

$$\gamma = \alpha - \beta \tag{5.2}$$

which follows from the triangle shown in Figs. 3.2 and 5.1 and formed by the points I, F_1 and F_2.

We note from Figs. 3.2 and 5.1 that for $d_c = 0$, the feed axis strikes the projection of the bottom edge of the main reflector (point L_p). For $d_c < 0$, there is a clearance between the bottom of the main reflector and the feed axis. For the classical configuration specified in Table 3.4, (5.1) yields

$$d_c = 13.7562 \text{ cm} = 6.5342 \ \lambda \tag{5.3}$$

showing that the feed axis intersects the main reflector of the analyzed configuration; see Fig. 3.7. Decreasing the angle γ brings the feed axis away from the main reflector, allowing access to the feed with a straight section of waveguide and creates additional room for feed assembly hardware.

Figure 5.2 shows the behavior of β as a function of α, such that Mizugutch condition (3.1) is satisfied. The curves follow from (3.1) with e as a parameter. It is easy to see from Fig. 5.2 that α is always greater than β. Thus, it is not possible to produce a Gregorian design optimized for low XPOL according to (3.1), such that the feed axis is directed away from the main reflector. This can be achieved with a Cassegrain configuration, but a main reflector other than just fully offset should be employed to avoid blockage; see Section 3.2.

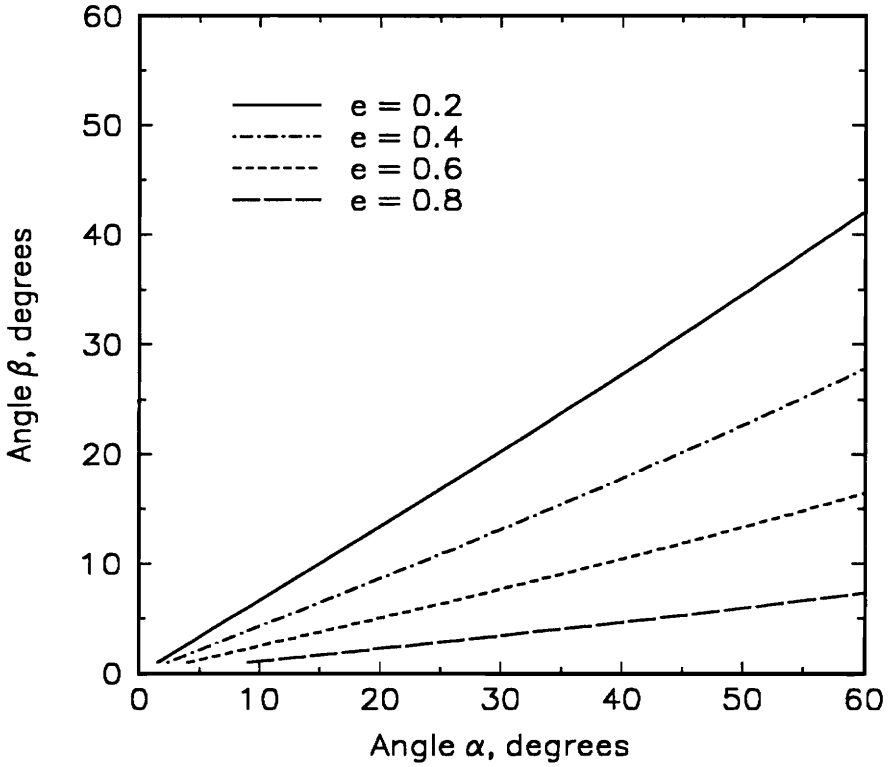

Figure 5.2. Dependence of angle β on angle α for geometries optimized for low XPOL according to Mizugutch condition. The curves follow from (3.1) for various subreflector eccentricity e values. Angles α and β are defined in Table 3.1.

Thus, the maximum possible clearance for a Gregorian configuration occurs with $\gamma = 0°$ (i.e., $\alpha = \beta$), which corresponds to a design with the feed axis parallel to the main reflector axis of symmetry (s). For this condition we can define the angle ν as

$$\nu = \alpha = \beta \tag{5.4}$$

The Mizugutch condition (3.1) then can be rewritten as

$$\frac{2\,e}{\cos\nu} = 1 + e^2 - |e^2 - 1| \tag{5.5}$$

where the subreflector eccentricity is by definition a positive number (i.e., $e \geq 0$) [35]. We now investigate all possible solutions of (5.5).

Case 1: Spherical Subreflector, $(e^2 - 1) < 0$ or $0 \leq e < 1$.

Then $|e^2-1| = -(e^2-1) = (1-e^2)$ and (5.5) has the following two possible solutions:

$$e = 0 \qquad \text{(spherical subreflector)} \tag{5.6}$$

and

$$e = \frac{1}{\cos\nu} \tag{5.7}$$

but the latter can be eliminated since it violates the condition $(e^2 - 1) < 0$.

Case 2: Parabolic Subreflector, $(e^2 - 1) = 0$ or $e = \pm 1$.

The value $e = +1$ is used since $e \geq 0$ and (5.5) is satisfied for

$$\nu = 0° \tag{5.8}$$

which corresponds to the double paraboloid configuration (i.e., both the main reflector and the subreflector are offset paraboloids). Since in this case the focal point F_2 is at infinity, the primary radiation should be as close to a plane wave as possible.

Case 3: Planar subreflector, $(e^2 - 1) > 0$ or $e > 1$.

Then $|e^2 - 1| = (e^2 - 1)$ and (5.5) reduces to

$$e = \cos \nu \tag{5.9}$$

which is not a valid solution since it violates the condition that $e > 1$. This case includes the planar subreflector where $e = \infty$. This solution is readily obtainable from Dragone condition [34]. Mizugutch and Dragone conditions are alternative mathematical forms of the same geometrical condition that assures XPOL minimization in dual offset reflector antennas [43]; see Appendix C (Chapter 12).

The spherical subreflector (Case 1) is not considered because the focal points F_1 and F_2 fall at the same position at center of the parent spheroid. This requires a special primary illumination to avoid caustics. Normally, an additional shaped reflector is employed. The planar subreflector (Case 3) is also not considered because of excessive spillover loss. Both focal points F_1 and F_2 are located at infinity in that

case. Thus, zero XPOL offset dual reflectors with aligned reflector axes (i.e., (5.5) is satisfied) must have a parabolic subreflector.

For proper operation, the subreflector of the dual parabolic configuration has to be illuminated by a plane wave, which can be obtained through the use of a feed horn with a lens or an array feed. Although feasible, this solution is not employed in the present study due to the constraint of using a single conventional feed. Thus, we conclude that for the stated design constraints, the feed and the main reflector axes cannot be parallel; i.e., $\alpha \neq \beta$.

An exact, practical solution does not exist because the posed problem was over constrained. However, we discovered that a solution does exist if the zero XPOL condition is relaxed to very low XPOL. This is accomplished by rotating the parent ellipsoid (i.e., the conical surface from where the offset subreflector is generated) until the desired clearance is obtained. However, this must be done in a way such that the feed remains pointed toward the intersection of the new subreflector and the ray coming from the center of the main reflector. The proposed procedure, fully described in the next section, avoids the introduction of spillover and phase errors, thus maintaining a satisfactory aperture efficiency and broad operational bandwidth.

5.3 Rotation of the Parent Ellipsoid

5.3.1 Analytical Development and Numerical Implementation

In this section we derive the expression for the value of β, denoted β_R, that yields the desired angle γ' between the main reflector and feed axes. Once γ' is

known, (5.1) is used to determine the new clearance d_c' between the feed axis and the bottom of the main reflector. We start by noting that the parent ellipsoid for the subreflector is only rotated and, therefore, the parameters c, e, and f_s, should remain unchanged. It can be shown using Fig. 5.3 and expressions derived in [35] that

$$\alpha' = \sin^{-1}\{\frac{\rho_1'}{\rho_2'}\sin[180^\circ - (\beta + \beta_R + \psi_C)]\} \tag{5.10}$$

where

$$\rho_1' = \frac{1+e}{1 - e\cos[180^\circ - (\beta + \beta_R + \psi_C)]} f_s \tag{5.11}$$

and

$$\rho_2' = 2(c + f_s) - \rho_1' \tag{5.12}$$

ρ_1' is the distance between the points F_1' and B' in Fig. 5.3, and ρ_2' is the distance between F_2' and B'. All other parameters are defined in Table 3.1. Equation (5.2) yields

$$\alpha' = (\beta + \beta_R) + \gamma' \tag{5.13}$$

since $\beta' = \beta + \beta_R$; see Fig. 5.3. Using (5.10) in (5.13), one obtains the following transcendental equation

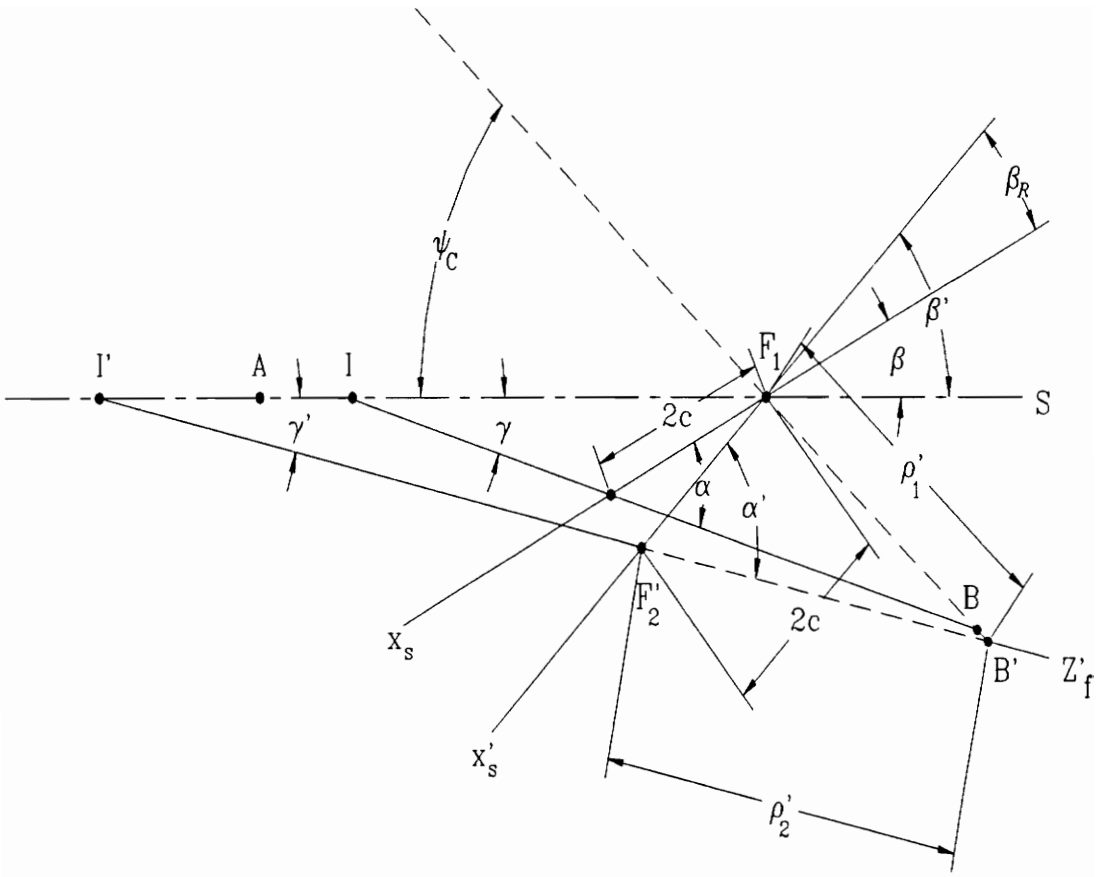

Figure 5.3. Geometry for determining of parent subreflector rotation β_R.

$$\frac{\frac{1+e}{1-e\cos(180°-\beta-\beta_R-\psi_C)}f_s}{2(c+f_s)-\frac{1+e}{1-e\cos(180°-\beta-\beta_R-\psi_C)}f_s}\sin(180°-\beta-\beta_R-\psi_C)=\sin(\beta+\beta_R+\gamma') \quad (5.14)$$

where β_R is the angle of rotation that yields the desired angle γ' between the main reflector and feed axes. Given the initial configuration and the desired angle γ', (5.14) can be employed to determine β_R. The value of γ', denoted γ'_A, such that the feed axis (z_f) just touches the apex of the main reflector (point A) is given approximately by

$$\gamma'_A \approx \tan^{-1}[\frac{\widehat{F_1B}\cos\psi_C}{F+\widehat{F_1B}\sin\psi_C}] \quad (5.15)$$

where $\widehat{F_1B}$ is the distance between the points F_1 and B in Fig. 5.3. Equation (5.15) is approximate because the point B displaces slightly during rotation of the parent ellipsoid. However, this is not a problem because usually only values of γ' smaller than γ'_A are employed when the main reflector is a just fully offset paraboloid. That is because clearance between the feed axis and the main reflector is expected for values of γ' such that $\gamma' < \gamma'_A$. When the main reflector is not just fully offset, a value greater than γ'_A may be employed depending on the degree of offset and on the desired amount of clearance. Although approximate, (5.15) is helpful in the determination of an adequate value for γ'.

The developed procedure, described by (5.10) to (5.15), was implemented in the program ROTATION. As already mentioned, the minimum XPOL Gregorian design produced by optimization codes such as OPTIMUM described in Section 3.4 very often has the feed axis intersecting the main reflector. This is avoided by using ROTATION, which rotates the parent ellipsoid (i.e., the conical surface from where

the offset subreflector is generated) until a desired clearance is obtained. This allows access to the feed antenna with a straight section of waveguide, thus reducing the complexity and cost of the manufacturing process. The rotation is performed in a way such that the feed remains pointed toward the intersection of the new subreflector and the ray coming from the center of the main reflector. The procedure avoids the introduction of spillover and phase errors, thus maintaining a satisfactory aperture efficiency and broad operational bandwidth. Typical input and output parameters used in ROTATION are:

Input parameters required by ROTATION: D, F, H, e, f_s, α, β, and the desired angle γ.

Output parameters (after rotating the parent ellipsoid): θ_E, α, β, e, c, f_s, d_c, ψ_C, ψ_L, ψ_U, and the subreflector projections onto the $x_s y_s$-plane and $y_s z_s$-plane.

5.3.2 Numerical Results and Comments

It is important to note that after rotation the conditions for low XPOL, (3.1) and/or (3.2), are no longer satisfied. Therefore, substantial XPOL is now present in the system. This is illustrated using the classical configuration of Table 3.4 as the initial configuration. In this case, (5.15) yields

$$\gamma'_A = 5.02^\circ \tag{5.16}$$

Choosing $\gamma' = 3°$ and solving (5.14) numerically gives

$$\beta_R = 11.41° \tag{5.17}$$

Rotating the parent ellipsoidal subreflector of the classical configuration specified in Table 3.4 by the amount in (5.17), produces the configuration listed in Table 5.1 and shown in Fig. 5.4. The subreflector projected height, D'_S, is given by

$$D'_S = \frac{1+e}{1-e\cos[180° - (\beta' + \psi_U)]} f_s \cos(90° - \psi_U) \tag{5.18}$$
$$- \frac{1+e}{1-e\cos[180° - (\beta' + \psi_L)]} f_s \cos(90° - \psi_L) = 15.8273\ \lambda$$

which is close to the value of 14.1800 λ, prior to the rotation (obtained from (5.18) by replacing β' with β). The difference is due to the fact that the offset subreflector is now cut from a different section of the parent ellipsoid. The new clearance distance, d'_c, for the geometry specified in Table 5.1 is given by (5.1) with β and γ replaced by β' and γ':

$$d'_c = -9.1366\ \text{cm} = -4.3399\ \lambda \tag{5.19}$$

This shows that clearance between the feed axis and the bottom of the main reflector was achieved by means of the rotation of the parent ellipsoidal subreflector.

However, as already noted, XPOL performance is expected to deteriorate due to the rotation. Figure 5.5 shows the co- and cross-polarized patterns computed by GRASP7 in the yz-plane for the configuration of Table 5.1 illuminated by an LP feed with no XPOL. The performance values are summarized in the same table. The XPOL is -33.14 dB, which is more than 15 dB worse than for the classical configuration.

Table 5.1.

Geometric Configuration and Computed Performance Values for the Classical Offset Dual Reflector of Table 3.4 After Rotation of the Parent Ellipsoidal Subreflector (see Table 3.1 for definitions of symbols)

Main Reflector (paraboloid):

$D = 115.8240\ \lambda$

$D_p = 231.6480\ \lambda$

$F/D_p = 0.3048$

$\psi_C = 44.60°$

$\psi_U = 78.72°$

Subreflector (ellipsoid):

$D'_S = 15.8273\ \lambda$

$c = 12.6340\ \lambda$

$f_s = 9.9146$

$e = 0.5603$

$\beta' = 15.53°$

Feed (located at the focal point F_2):

Pattern shape = Gaussian (Fig. 4.1)

Gain G = 22.30 dBi

$\alpha' = 18.53°$

$\gamma' = 3.00°$

11 dB beamwidth = 26.76°

Polarization = Linear (x_f-directed)

XPOL = None

Computed Performance Values:

Gain (G), dBi	49.88
Cross polarization level (XPOL), dB	-33.14
Side lobe level (SLL), dB	-26.79
Spillover loss, dB	0.31
Aperture efficiency (ϵ_{ap}), %	73.47

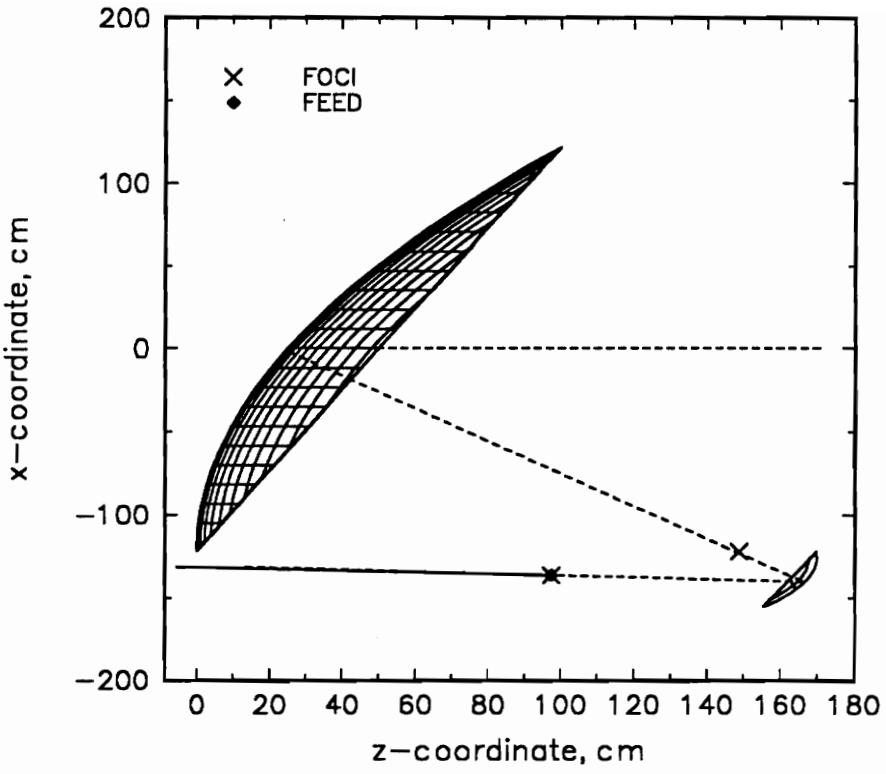

Figure 5.4. Geometry of the dual offset Gregorian reflector antenna after rotation of the parent ellipsoidal subreflector. The configuration parameters are listed in Table 5.1 (f = 14.25 GHz). Note the clearance between the bottom of the main reflector and the feed axis.

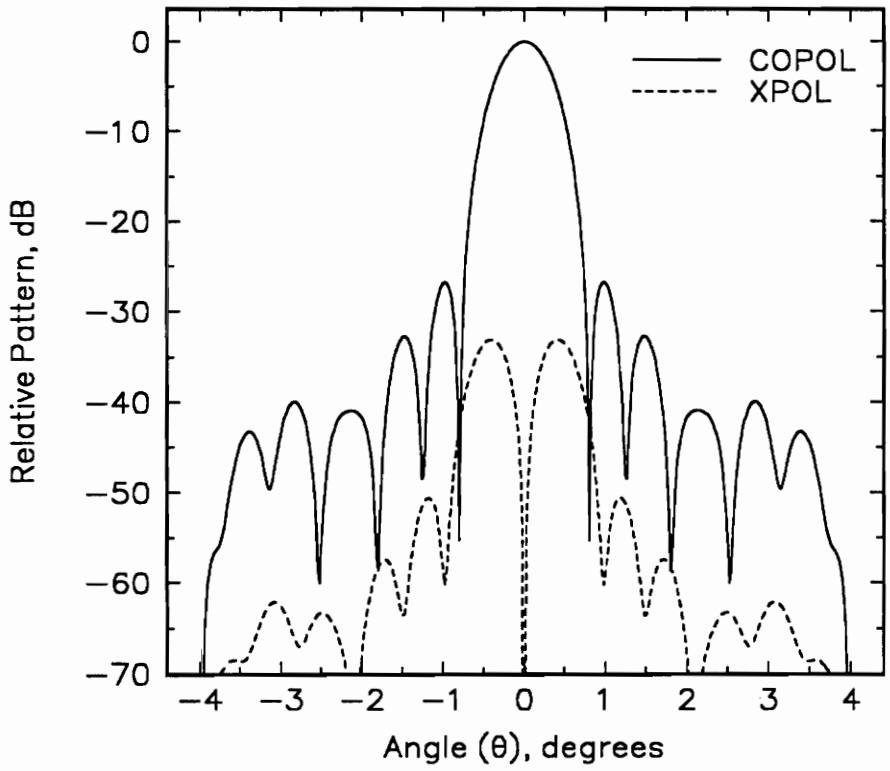

Figure 5.5. Computed co- (solid curve) and cross-polarized (dotted curve) far-field patterns for the configuration of Table 5.1, obtained by rotation of the parent ellipsoidal subreflector. The patterns were computed in the $\phi = 90°$ plane (i.e., the yz-plane in Fig. 3.2). The XPOL peak is 33.14 dB below the COPOL peak.

The XPOL level of -33.14 dB (after rotation) may not be adequate; however, it can be reduced by changing the eccentricity value of the ellipsoidal subreflector as discussed in the next section. Table 5.6 in Section 5.6 summarizes all the necessary steps developed in Chapters 3 and 5 for designing a low cross-polarized, dual offset reflector antenna with adequate clearance between the main reflector and feed axis.

5.4 Reduction of System XPOL by Altering the Subreflector Eccentricity Value

5.4.1 Analytical Development and Numerical Implementation

In this section the procedure for reducing XPOL by changing the eccentricity value of the ellipsoidal subreflector is developed. First, we note from Fig. 5.6 that the configuration of Table 5.1 (after rotation) satisfies Mizugutch condition (3.1) for a new subreflector eccentricity value of $e'' = 0.0896$ (the value listed in Table 5.1 is 0.5603). However, such a small eccentricity value causes the feed axis to intersect the main reflector once again ($d_c'' = 3\,\lambda$), or results in a subreflector height larger than that of the main reflector ($D_S'' = 181.4764\,\lambda$), depending on whether f_s or c is kept constant for the new value of e. Although illustrated for the configuration of Table 5.1, this is a generic result since as we rotate the parent subreflector, γ decreases with $\alpha \rightarrow \beta$, and $e \rightarrow 0$; see Fig. 5.6. Therefore, directly use of (3.1) with the geometry obtained after the parent subreflector rotation yields low eccentricity values and is herein discarded.

In Section 5.3.1 we showed that the double paraboloid configuration is the only practical solution to (3.1) that yields a design with the feed axis parallel to the

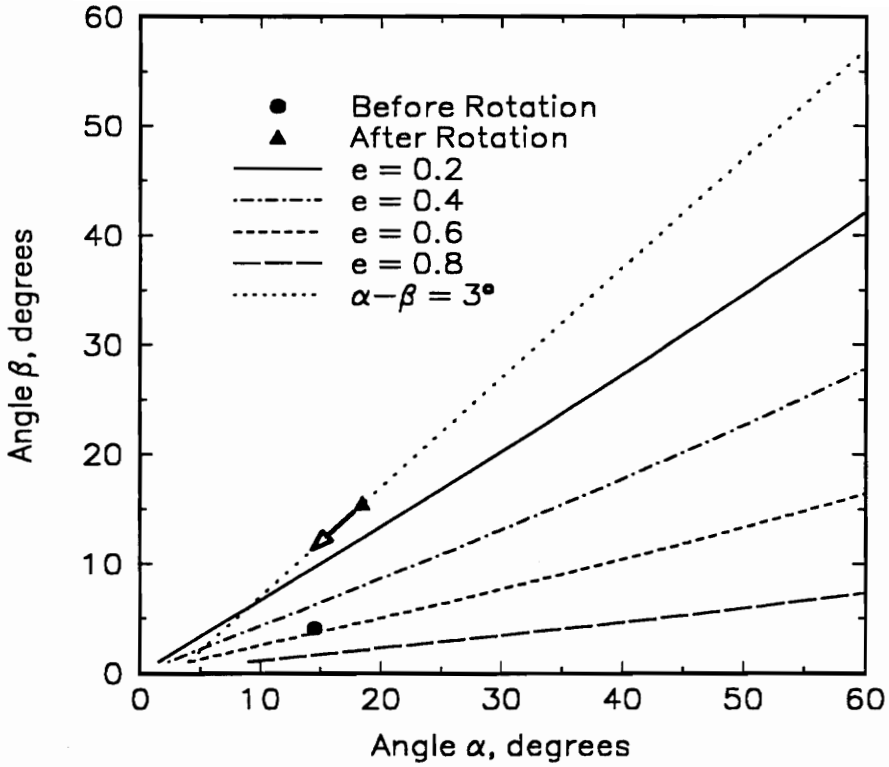

Figure 5.6. Dependence of angle β on angle α for geometries optimized for low XPOL according to the Mizugutch condition. The values of α and β for the configurations listed in Tables 3.4 (before rotation) and Table 5.1 (after rotation) are shown in the figure. Note that the configuration of Table 5.1 (after rotation) satisfies Mizugutch condition (3.1) for a new subreflector eccentricity value of $e'' = 0.0896$ (the value listed in Table 3.4 is $e = 0.5603$). This, however, is not a practical solution as discussed in the text.

main reflector axis. This shows that as $\gamma \rightarrow 0°$, with $\alpha \rightarrow 0°$ and $\beta \rightarrow 0°$, then $e \rightarrow 1$. Therefore, as we reduce γ by subreflector rotation, α and β should also be reduced by increasing e in order to reduce XPOL and eventually satisfy Mizugutch condition (3.1). For the geometry of Table 5.1 (after rotation), this is achieved by increasing the value of e, which reduces α and β as indicated by the arrow in Fig. 5.6. Note that the angle $\gamma = \alpha - \beta = 3°$ is kept constant, thus preserving the clearance obtained with the subreflector rotation. Furthermore, the proposed procedure gives control on the amount of XPOL to be reduced, since e can be altered just enough to meet a XPOL specification without necessarily satisfying Mizugutch condition.

Thus, the proposed approach is to increase the subreflector eccentricity e to a new value, e''. This relocates the focal point F_2' to a new position F_2'' on the feed axis z_f as shown in Fig. 5.7. Note that when F_2'' is at infinity, $e'' = 1$. This procedure keeps the angle $\gamma' = \alpha' - \beta' = \alpha'' - \beta''$ constant, thus maintaining the desired clearance between the feed axis and the bottom of the main reflector. In addition, the subreflector height D_S' remains approximately the same since f_s is not altered.

According to Fig. 5.7, the new value of β', denoted β'', is determined by noting that,

$$h' = 2\,c \sin\alpha' = 2\,c'' \sin\alpha'' \tag{5.20}$$

but $\alpha' = \beta' + \gamma'$ and $\alpha'' = \beta'' + \gamma'$. Thus,

$$\beta'' = \sin^{-1}[\frac{c}{c''} \sin(\beta' + \gamma')] - \gamma' \tag{5.21}$$

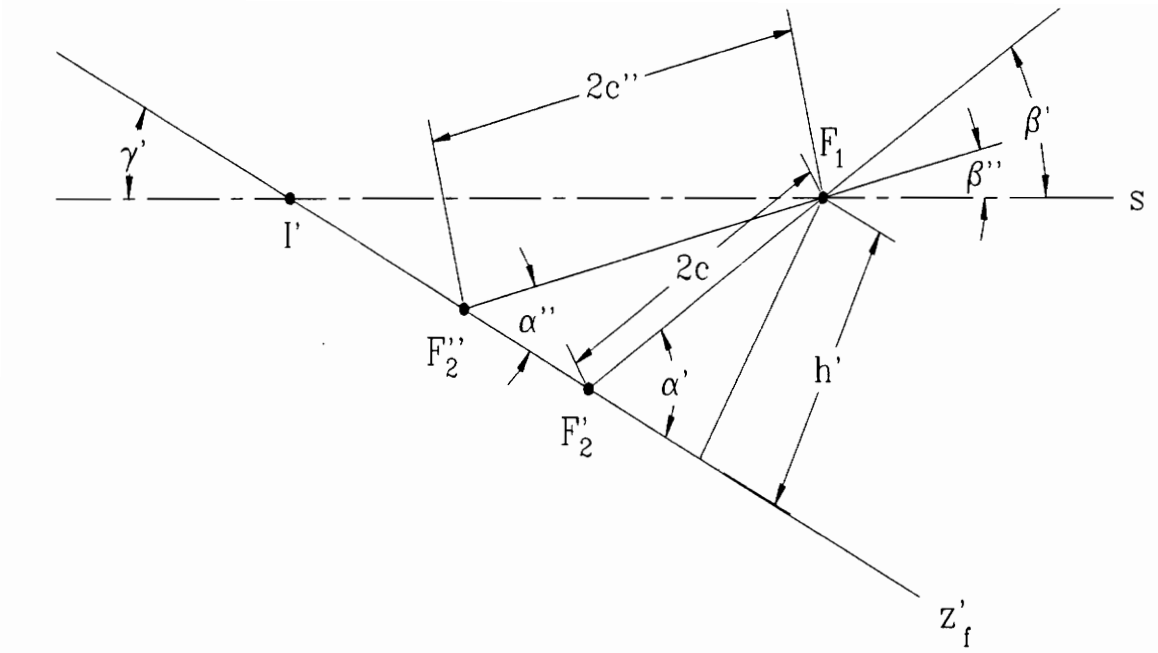

Figure 5.7. Geometrical determination of β'' for a new value of the subreflector eccentricity e''.

where c'' is determined according to the new eccentricity value e'' ($e < e'' < 1$) [35],

$$c'' = \frac{e'' f_s}{1 - e''} \tag{5.22}$$

The procedure described by (5.20) to (5.22) and Fig. 5.7 was implemented with other equations in the program ECCENTRICITY. Together with OPTIMUM, VERIFY and ROTATION, ECCENTRICITY forms the DORA package (Dual Offset Reflector Antenna Synthesis Package). Using the design generated by ROTATION as the starting point, ECCENTRICITY computes the various geometrical parameters of the dual offset configuration for a new subreflector eccentricity value, which is specified by the user. In general, eccentricity values greater than the one used with ROTATION will reduce system XPOL. ECCENTRICITY produces a low cross-polarized (-35 dB or better) dual offset Gregorian antenna which has adequate clearance between the feed axis and the bottom of the main reflector. The designed configuration has the ability to operate with either a LP or a CP feed over a wide bandwidth without the need of being repositioned (no substantial beam squint). Typical input and output parameters used in ECCENTRICITY are:

Input parameters required by ECCENTRICITY: D, F, H, c, f_s, α, β, and the new eccentricity value for the ellipsoidal subreflector.

Output parameters (after altering the eccentricity value): θ_E, α, β, e, c, f_s, d_c, ψ_C, ψ_L, ψ_U, and the subreflector projections onto the $x_s y_s$-plane and $y_s z_s$-plane.

In addition, ECCENTRICITY creates a data file that numerically describes the subreflector surface as a set of points defined with respect to the subreflector coordinate system $x_s y_s z_s$; see Fig. 3.2. This is a valuable feature especially when the subreflector is to be fabricated by a computerized machining process.

5.4.2 Numerical Results and Comments

In order to investigate the behavior of XPOL as a function of the eccentricity value e'', we define the following figure of merit

$$\Delta_M = |\tan\alpha'' - \frac{|(e'')^2 - 1|\sin\beta''}{[1 + (e'')^2]\cos\beta'' - 2e''}| \tag{5.23}$$

which was obtained by taking the difference between the left and right sides of Mizugutch condition (3.1). A decrease in Δ_M indicates a decrease in system XPOL, with Mizugutch condition being satisfied for $\Delta_M \to 0$.

Figure 5.8 shows Δ_M as a function of e'' for the configuration specified in Table 5.1. It is easy to see from Fig. 5.8 that XPOL reduction should be achieved by increasing the eccentricity value from $e = 0.5603$ ($\Delta_M = 0.9282$) to $e'' = 0.8785$ ($\Delta_M \approx 0$). In general, any configuration presenting a rotated parent ellipsoid can satisfy Mizugutch condition (3.1) by means of replacing the eccentricity value e by one within the range $e < e'' < 1$. However, as e is increased, the distance between the feed and the subreflector increases (see Fig. 5.7), increasing the spillover loss. This leads to penalties in gain and aperture efficiency. Therefore, it is recommended to alter e just enough to meet the specifications on XPOL.

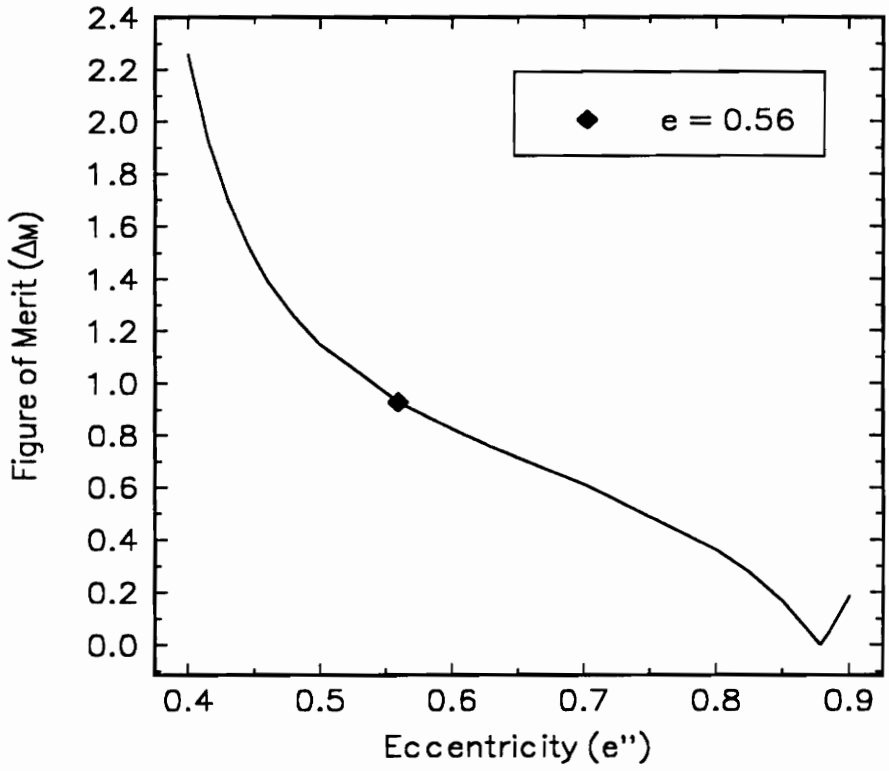

Figure 5.8. Figure of merit Δ_M as a function of the eccentricity e''. The point shown is for the initial value $e = 0.56$ which is the dual offset configuration specified in Table 5.1.

Table 5.2 lists the dual reflector configuration obtained by replacing the subreflector of Table 5.1 ($e = 0.5603$) by one with $e'' = 0.6300$ ($\Delta_M = 0.7571$). The geometrical configuration is shown in Fig. 5.9. Note the clearance between the feed axis and the bottom of the main reflector. Figure 5.10 shows the corresponding co- and cross-polarized patterns computed in the yz-plane. We note that the proposed configuration presents XPOL = -35.12 dB, thus meeting the specification for low XPOL and maintaining the desired clearance d_c' given in (5.19). Table 5.2 also summarizes all the computed performance values. The eccentricity value of 0.6300 was obtained by increasing e until system XPOL was just below -35 dB and resulted in a satisfactory aperture efficiency of about 70%. If eccentricity values larger than 0.6300 (but smaller than 0.8785) are used, see Fig. 5.8, lower XPOL levels are obtained at sacrifice of gain, as already discussed. It is worth mentioning that the final design is broadband since no phase errors are introduced.

Finally, for completeness, we use the same sub-optics assembly listed in Table 5.2 with the 1.8-m diameter main reflector specified in Table 3.3. The resultant configuration is listed in Table 5.3 and shown in Fig. 5.11. Table 5.3 also summarizes all the performance values, obtained with GRASP7 in the yz-plane. We note that the configuration presents XPOL = -35.04 dB, thus meeting the specification for low XPOL and maintaining an adequate clearance between the feed axis and the bottom of the main reflector. In fact, the clearance distance is now larger than the one obtained with the 2.4-m diameter main reflector. This is because the 1.8-m diameter dish has a shorter focal length; see Fig. 3.4 in Section 3.5 for further details. In the next section we investigate the possibility of enforcing the practical constraints discussed in this dissertation on the Green Bank Telescope reflector antenna.

Table 5.2.

Geometric Configuration and Computed Performance Values for the Offset Dual Reflector Antenna Specified in Table 5.1 After Alteration of the Ellipsoidal Subreflector Eccentricity Value (see Table 3.1 for definitions of symbols)

Main Reflector (paraboloid):

$D = 115.8240\ \lambda$

$D_p = 231.6480\ \lambda$

$F/D_p = 0.3048$

$\psi_C = 44.60°$

$\psi_U = 78.72°$

Subreflector (ellipsoid):

$D''_S = 15.7576\ \lambda$

$c'' = 16.8816\ \lambda$

$f_s = 9.9146$

$e'' = 0.6300$

$\beta'' = 10.76°$

Feed (located at the focal point F_2):

Pattern shape = Gaussian (Fig. 4.1)

Gain G = 22.30 dBi

$\alpha'' = 13.76°$

$\gamma' = 3.00°$

11 dB beamwidth = 26.76°

Polarization = Linear (x_f-directed)

XPOL = None

Computed Performance Values:

Gain (G), dBi	49.63
Cross polarization level (XPOL), dB	-35.12
Side lobe level (SLL), dB	-22.34
Spillover loss, dB	0.94
Aperture efficiency (ϵ_{ap}), %	69.20

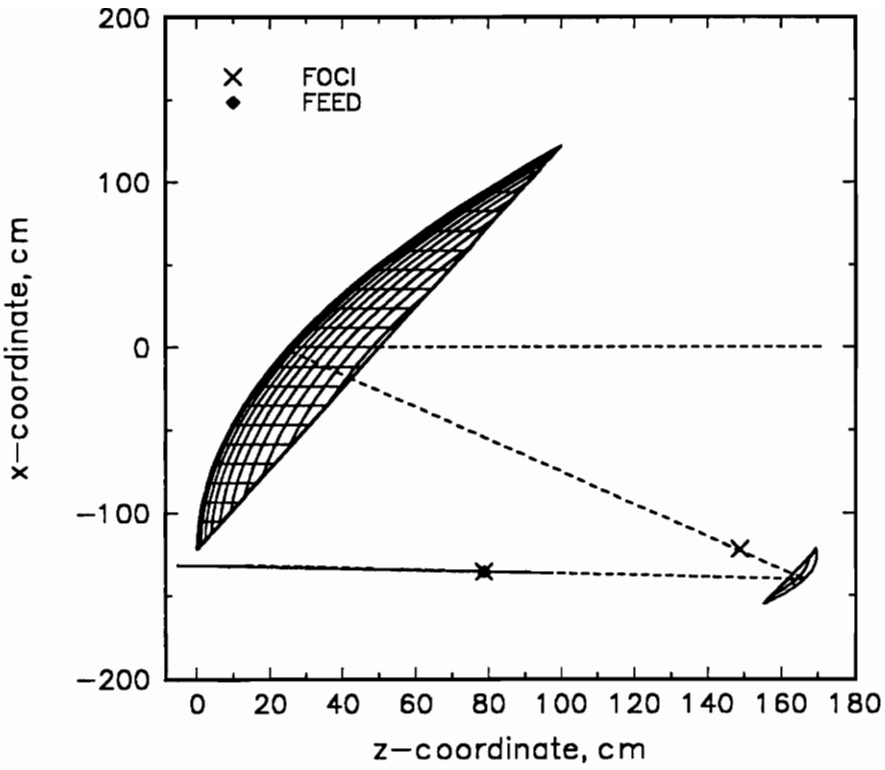

Figure 5.9. Geometry of the dual offset Gregorian reflector antenna after alteration of the ellipsoidal subreflector eccentricity value. The configuration parameters are listed in Table 5.2 (f = 14.25 GHz). Note the clearance between the bottom of the main reflector and the feed axis.

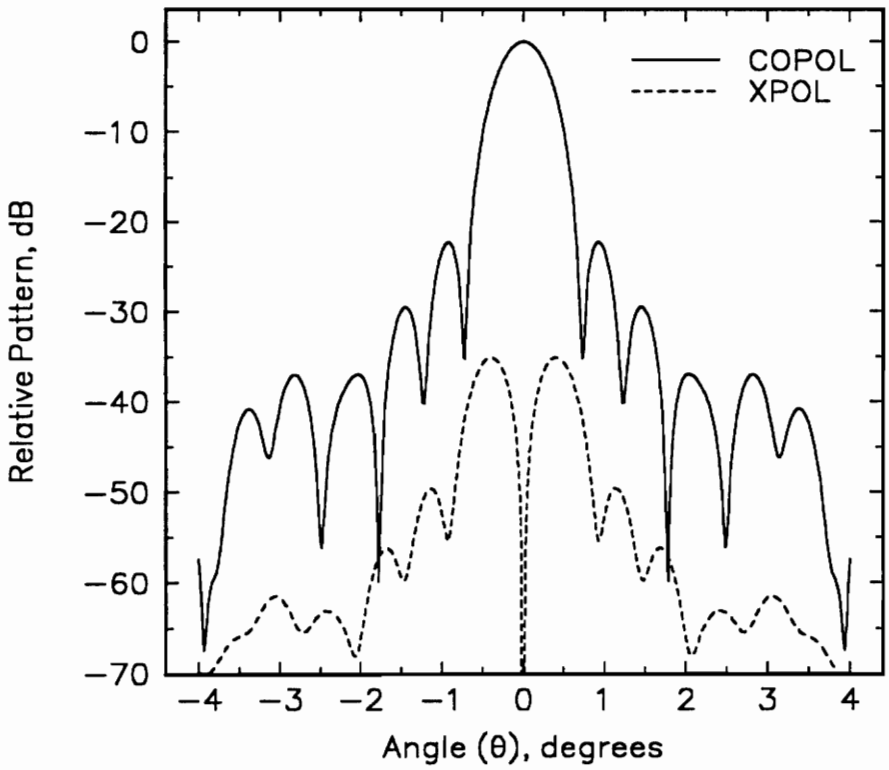

Figure 5.10. Computed co- (solid curve) and cross-polarized (dotted curve) far-field patterns for the configuration of Table 5.2, which employs an ellipsoidal subreflector of eccentricity $e = 0.63$. The patterns were computed in the $\phi = 90°$ plane (i.e., the yz-plane in Fig. 3.2). The XPOL peak is 35.12 dB below the COPOL peak.

Table 5.3.

Geometrical Configuration and Computed Performance Values for the Offset Dual Reflector Antenna Formed by the Sub-Optics Assembly Specified in Table 5.2 With a 1.8-m Diameter Main Reflector.

(a) Main Reflector Configuration	
Shape	Offset paraboloid
Projected diameter (D), λ	85.5
Parent reflector diameter (D_p), λ	171.0
Focal length (F)	0.3048 D_p
Offset of reflector center (H)	$D/2$
(b) Subreflector Configuration	
Shape	Offset ellipsoid
Projected height (D_S''), λ	15.7576
Parameter c'' of ellipse, λ	16.8816
Parameter f_s of ellipse, λ	9.9146
Eccentricity (e'')	0.6300
Angle β'', degrees	10.76
(c) Feed Configuration	
Polarization	Linear (x_f)
Pattern shape	Gaussian
Gain (G_f), dBi	22.30
11-dB beamwidth, degrees	26.76
Angle α'', degrees	13.76
Angle γ', degrees	3.00
Distance d_c, λ	-5.31
(d) System Performance (GRASP)	
Gain (G), dBi	46.98
Cross polarization level (XPOL), dB	-35.04
Side lobe level (SLL), dB	-22.37
Spillover loss, dB	0.94
Aperture efficiency (ϵ_{ap}), %	69.10

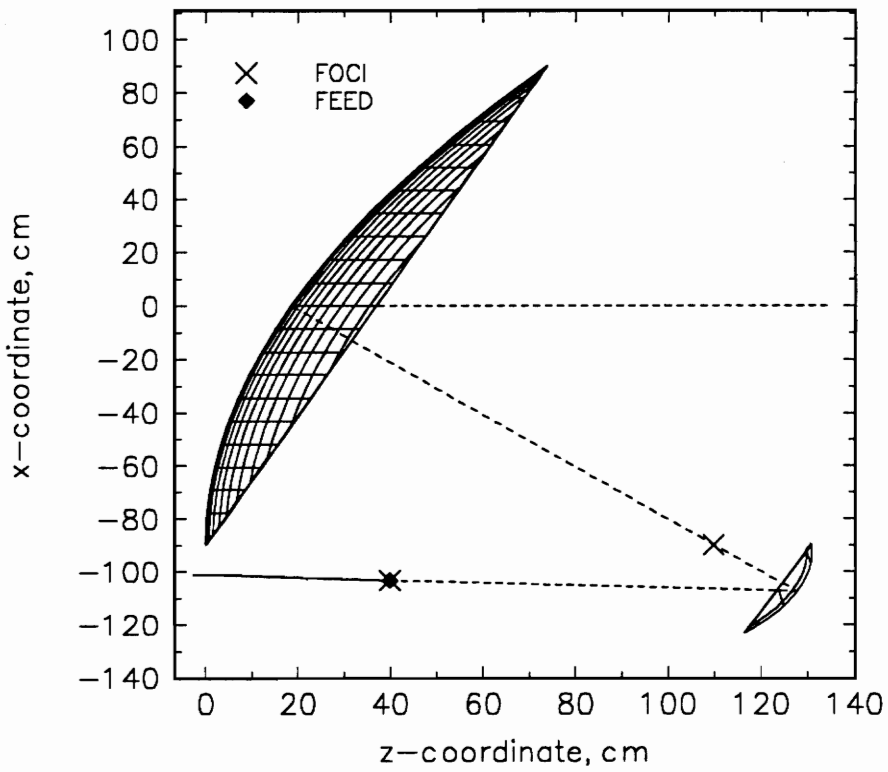

Figure 5.11. Geometry of the dual offset Gregorian reflector antenna specified in Table 5.3 (f = 14.25 GHz). Note the clearance between the bottom of the main reflector and the feed axis.

5.5 The Green Bank Radio Telescope

This section briefly summarizes the results of a computational study performed to evaluate the electrical performance of the Green Bank Telescope reflector antenna [7, 8]. All computed patterns were obtained with the commercial code GRASP7 [15] and with the Virginia Tech code PRAC (Parabolic Reflector Analysis Code). The Green Bank Telescope (GBT) consists of a 100-m diameter offset parabolic reflector that can be operated as a single offset reflector system (prime-focus), or as a dual offset Gregorian reflector system with an ellipsoidal subreflector [7, 8]. The Gregorian configuration allows the main reflector to be used in either mode without the need of removing the subreflector. This is not possible with a Cassegrain configuration [7].

We performed calculations on the dual offset Gregorian configuration to optimize its performance for low cross polarization (XPOL) using the Virginia Tech code DORA, Dual Offset Reflector Antenna Synthesis Package, developed by the author. The geometrical parameters determined with DORA are in very good agreement with the ones published in [7]. New designs can be obtained with DORA if input parameters, such as the subreflector size obtained from [7], are changed.

5.5.1 The GBT Single Offset Configuration

We start by examining the GBT single offset configuration with the characteristics listed in Table 5.4. The symbols are defined in Table 3.1 and are shown in Fig. 3.2. Figure 5.12 shows the computed co- and cross-polarized patterns for the offset parabolic reflector of Table 5.4 in the yz-plane. XPOL is expected to be maximum in this plane [4]. The patterns were computed using both the commercial code GRASP7 [15] and the Virginia Tech code PRAC.

Table 5.4.

Geometrical Parameters and Performance Values for the GBT Single Offset Reflector Configuration

(a) Main Reflector Configuration		
Shape: Offset paraboloid		
Projected diameter (D), m	100.0	
Parent reflector diameter (D_p), m	208.0	
Focal length (F), m	60.0	
Offset of reflector center (H), m	54.0	
(b) Feed Configuration	**PRAC**	**GRASP**
Polarization	Linear (x_f)	Linear (x_f)
Pattern shape	$\cos^{4.58}$	Gaussian
Gain (G_f), dBi	13.08	13.14
10-dB beamwidth, degrees	77.92	77.92
Feed pointing angle (ψ_f), degrees	42.77	42.77
Feed Taper (Lower,Upper), dB	(-10.0,-10.0)	(-10.0,-10.0)
(c) System Performance	**PRAC**	**GRASP**
Gain (G), dBi	82.87	82.79
Cross polarization level (XPOL), dB	-21.54	-21.56
Side lobe level (SLL), dB	-26.72	-27.21
Aperture efficiency (ϵ_{ap}), %	78.48	77.05

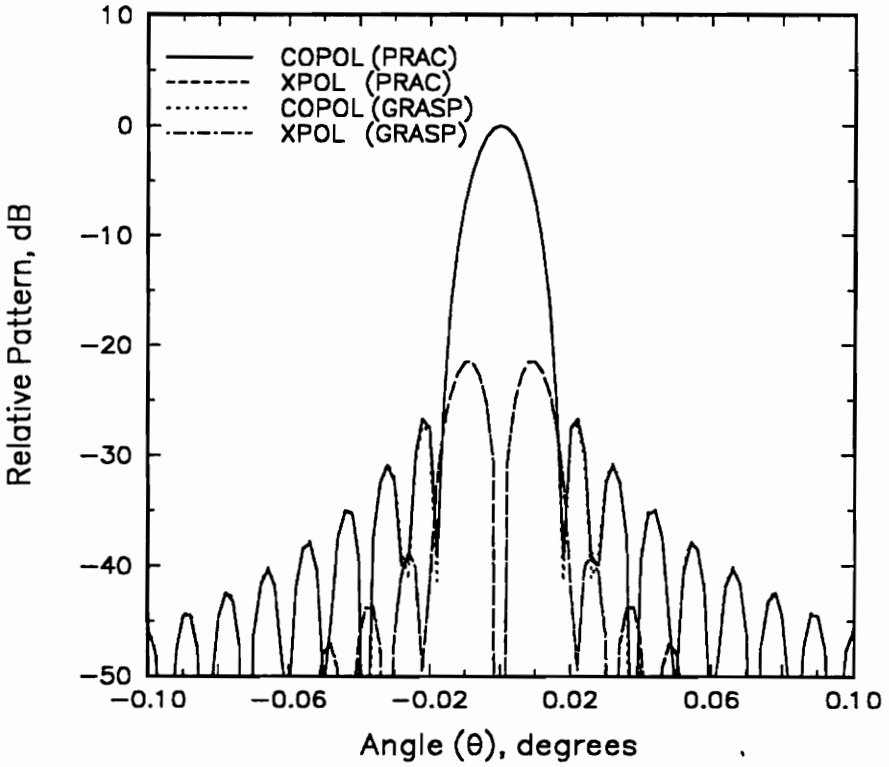

Figure 5.12. Radiation patterns of the GBT single offset reflector configuration specified in Table 5.4 (f = 15 GHz).

PRAC is a user friendly code developed by the author to analyze axisymmetric and offset parabolic reflectors. PRAC evaluates the radiation integral (physical optics surface current integration) with the Jacobi-Bessel method [13, 14], and yields the co- and cross-polarized radiated fields with high accuracy and efficiency; see Appendix B (Chapter 11) for a complete description of PRAC.

We note from Fig. 5.12 that both PRAC and GRASP7 yield almost identical results for this reflector configuration. Table 5.4 also lists the computed performance values. Aperture efficiency (ϵ_{ap}) was computed according to (3.16) [12].

This example is typical of single offset reflectors and shows that single offset paraboloids illuminated by conventional feeds are limited by XPOL performance. A XPOL level of about -22 dB is often unacceptable high. In the next section we add an ellipsoidal subreflector to the GBT offset paraboloid in order to form a low XPOL dual offset Gregorian configuration.

5.5.2 The GBT Dual Offset Gregorian Configuration

Dual offset reflector configurations can be designed for low geometrical optics XPOL when illuminated by a pure linearly polarized feed [16, 31]. Our goal is to study how the GBT of Table 5.4 can be upgraded to a low cross-polarized, dual offset Gregorian reflector antenna. This can be accomplished by adding a concave ellipsoidal subreflector to the original single reflector system, as explained in Chapter 3. The general geometry of a dual offset Gregorian antenna is presented in Fig. 3.2 and the symbols are defined in Table 3.1.

The procedure presented in Chapter 3 is especially useful in upgrading existing single reflector configurations with any degree of offset and is applied to the GBT offset paraboloid of Table 5.4 to determine the corresponding low cross-polarized dual configuration. Design parameters, such as the desired subreflector size, were obtained from [7]. The resulting configuration is listed in Table 5.5 and agrees well with the one published in [7]. Although not performed in this work, new dual configurations for the GBT offset reflector can be obtained with DORA for different design parameters, such as a new subreflector size.

Table 5.5 also presents the performance values at 15 GHz computed with GRASP in the plane normal to the plane of symmetry (i.e., the yz-plane in Fig. 3.2). Figure 5.13 shows the co- and cross-polarized patterns computed by GRASP in this same plane. We note that XPOL is now -43.01 dB, more than 20 dB lower than the XPOL of the single configuration in Table 5.4. However, a feed antenna with high XPOL will likely degrade the total system XPOL performance.

We note from Table 5.5 that the clearance distance d_c, computed according to (5.1), is 5.3468 m. This shows that the feed axis intersects the main reflector of the dual configuration. However, due to the large dimensions of the reflectors it is not necessary to impose the clearance constraint introduced in this chapter. Nevertheless, this case example shows that the feed axis can intersect main reflectors that are not necessarily just fully offset. In general, the problem depends on the degree of offset, H, and on the physical dimensions of the reflectors, as showed by the GBT case example.

Table 5.5.

Geometrical Parameters and Computed Performance Values for the GBT Dual Offset Gregorian Reflector Configuration

(a) Main Reflector Configuration	
Shape	Offset paraboloid
Projected diameter (D), m	100.0
Parent reflector diameter (D_p), m	208.0
Focal length (F), m	60.0
Offset of reflector center (H), m	54.0
(b) Subreflector Configuration	
Shape	Offset ellipsoid
Projected height (D_S), m	7.5500
Parameter c of ellipse, m	5.9855
Parameter f_s of ellipse, m	5.3542
Eccentricity (e)	0.5278
Angle β, degrees	5.58
(c) Feed Configuration	
Polarization	Linear (x_f)
Pattern shape	Gaussian
Gain (G_f), dBi	21.31
10-dB beamwidth, degrees	30.00
Angle α, degrees	17.91
Angle γ, degrees	12.33
Distance d_c, m	5.3468
(d) System Performance (GRASP)	
Gain (G), dBi	82.83
Cross polarization level (XPOL), dB	-43.01
Side lobe level (SLL), dB	-22.56
Aperture efficiency (ϵ_{ap}), %	77.76

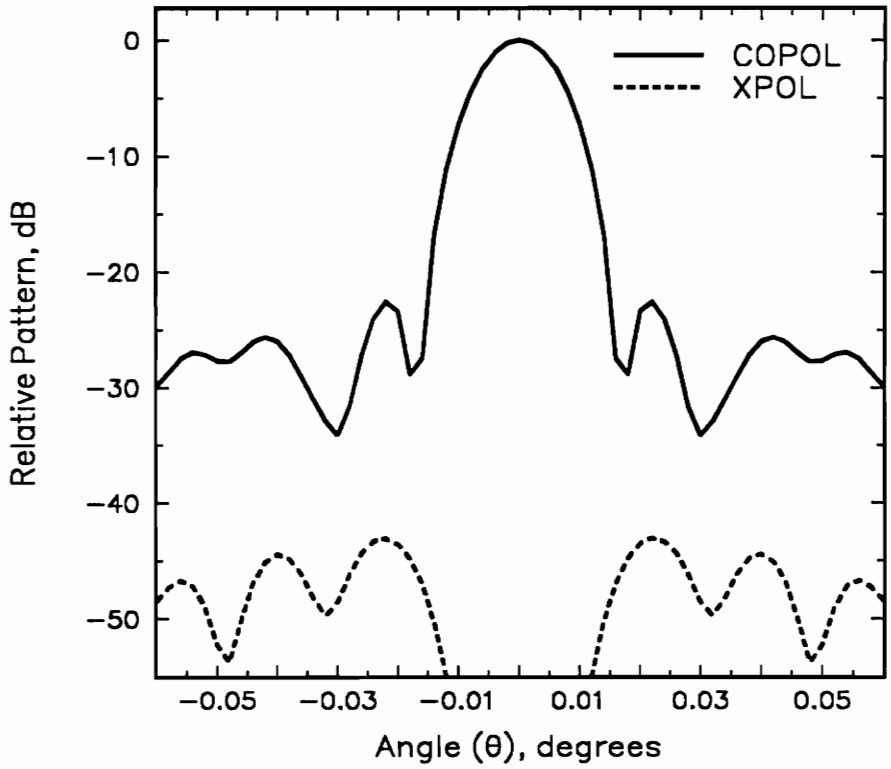

Figure 5.13. Radiation patterns of the GBT dual offset Gregorian reflector configuration specified in Table 5.5 (f = 15 GHz).

5.6 Conclusions

A procedure to rotate the parent ellipsoidal subreflector of a dual offset Gregorian reflector antenna was introduced. This was necessary to achieve clearance between the bottom of the main reflector and the feed axis in our study configuration. Manufacturing costs can be substantially reduced through the enforcement of this condition. However, the rotation of the subreflector introduces substantial XPOL in a system designed to present low XPOL. The proposed solution is to replace the subreflector by one of higher eccentricity, producing a design with the desired XPOL performance and suitable clearance between the main reflector and feed axis. Also, the resultant design presents large operational bandwidth since the feed was relocated to the focal point of the new ellipsoidal subreflector, avoiding the introduction of phase errors. Table 5.6 summarizes all the necessary steps developed in Chapters 3 and 5 for upgrading an existing single offset reflector to a low cross-polarized, dual offset reflector antenna with adequate clearance between the main reflector and feed axis.

In addition, the electrical performance of the Green Bank Telescope (GBT) reflector antenna was evaluated with the commercial code GRASP7 and the Virginia Tech code PRAC (Parabolic Reflector Analysis Code). The Virginia Tech code DORA (Dual Offset Reflector Antenna Synthesis Package) was employed to upgrade the GBT single offset configuration to a low cross-polarized dual offset Gregorian reflector configuration. The geometrical parameters determined with DORA are in very good agreement with the ones published in [7]. New designs can be obtained with DORA if the subreflector size is changed.

Table 5.6.

Steps for Upgrading an Existing Single Offset Reflector to a Low Cross-Polarized, Dual Offset Reflector Antenna With Adequate Clearance Between the Main Reflector and Feed Axis

	Procedures	Selected Eqs.	Figs.	Codes
1:	Single Reflector Upgrading	(3.4) to (3.10)	3.2	
		(3.11) to (3.14)	3.3	OPTIMUM.EXE
2:	Parent Subreflector Rotation	(5.1) and (5.18)	5.1	
		(5.10) to (5.15)	5.3	ROTATION.EXE
3:	Eccentricity Value Alteration	(5.1) and (5.18)	5.1	
		(5.20) to (5.22)	5.7	ECCENTRI.EXE

The computer simulations confirmed a low cross polarization level, XPOL, when the GBT dual configuration is illuminated by a purely polarized feed antenna. A feed antenna with high XPOL will likely degrade the total system XPOL performance. This problem was investigated in Chapter 4 and is re-addressed in the next chapter.

Chapter 6

Shaping of Subreflectors for System XPOL Reduction

6.1 Introduction

The problem of reducing XPOL effects caused by conventional, low-cost feeds was first investigated in Chapter 4 and is re-examined in this chapter. A modified version of the feed model used in Chapter 4 is considered here. The XPOL effects of this feed model cannot be reduced by feed rotation, in contrast to the model used in Chapter 4. In addition, the model considered in this chapter approximates better the theoretical behavior of conical corrugated horns, a class of feed antennas widely employed to illuminate commercial reflector systems [44, 18].

The proposed general solution to minimize feed XPOL effects of this class of feed antennas is to shape the subreflector of the dual offset configuration. The resulting non-conical subreflector (distorted ellipsoid) introduces phase-errors and pattern degradation, in contrast to all procedures discussed in previous chapters. Nevertheless, the resulting configurations are able to meet all EUTELSAT specifications [11], even when illuminated by feed antennas with relatively high XPOL levels. The shaping algorithm, based on the gradient method [41], is described in detail in this chapter.

6.2 Enhanced Feed Model

Corrugated conical horns are widely employed to illuminate commercial reflector configurations [18]. These antennas are well characterized and entire books have already been written on the subject (e.g., [44]). Therefore, we will not completely describe the antenna, but rather will present a model that approximates the electrical behavior. In order to accomplish that we combine the unbalanced feed model of (2.6) with (4.1) and (4.2). The result is [15]

$$\vec{E}_{\text{co}}(\vec{r}_f) = \{[C_{\theta_f}(\theta_f)\cos^2\phi_f + C_{\phi_f}(\theta_f)\sin^2\phi_f] + p_r[C_{\theta_f}(\theta_f) - C_{\phi_f}(\theta_f)]\cos\phi_f\sin\phi_f)\}$$
$$[\hat{\theta}_f\cos\phi_f - \hat{\phi}_f\sin\phi_f]\frac{e^{-j\beta r_f}}{r_f} \tag{6.1}$$

and

$$\vec{E}_{\text{cross}}(\vec{r}_f) = \{p_r[C_{\theta_f}(\theta_f)\sin^2\phi_f + C_{\phi_f}(\theta_f)\cos^2\phi_f] + [C_{\theta_f}(\theta_f) - C_{\phi_f}(\theta_f)]\cos\phi_f\sin\phi_f)\}$$
$$[\hat{\theta}_f\sin\phi_f + \hat{\phi}_f\cos\phi_f]\frac{e^{-j\beta r_f}}{r_f} \tag{6.2}$$

This model is nominally linearly polarized along the x_f-direction. XPOL is introduced with non-zero values of p_r, which is described in Section 4.2 and given by (4.3). It is important to note that (6.1) and (6.2) reduce to (4.1) and (4.2) for $C_{\theta_f}(\theta_f) = C_{\phi_f}(\theta_f)$ (i.e., balanced case). In addition, (6.2) yields the cross-polarized peaks in the 45°-planes, which is consistent with measured data and more sophisticated theoretical models [44].

In this chapter the E- and H-plane patterns, $C_{\theta_f}(\theta_f)$ and $C_{\phi_f}(\theta_f)$, are described by Gaussian models similar to (2.10). The amplitude levels are set to different values in each plane in order to produce the cross-polarized peaks in the 45°-planes. In addition, the peak cross-polarized lobes alternate in phase, which makes the feed

rotation technique of Chapter 4 ineffective. The proposed solution to reduce XPOL effects of this class of feeds is subreflector shaping. This is accomplished using a shaping algorithm based on the gradient method, as explained in the next section.

6.3 The Gradient Method

6.3.1 Theoretical Formulation and Numerical Implementation

The gradient of a scalar function, ∇X, is a vector pointing in the direction of maximum increase of $X(z_{s1}, z_{s2}, \ldots, z_{sn})$. The size of the gradient, $|\nabla X|$, indicates the rate of that variation. Both the gradient direction and size are independent of the chosen coordinate system [45].

Since, in the present case, the analytical form of the function X describing the XPOL behavior of the dual reflector antenna system is unknown, we approximate the unitary vector $\vec{g}$ in the direction of ∇X by (first order approximation)

$$\vec{g} = \frac{\nabla X}{|\nabla X|} \approx \frac{\frac{\Delta X_1}{\Delta z_{s1}}\hat{z}_{s1} + \frac{\Delta X_2}{\Delta z_{s2}}\hat{z}_{s2} + \ldots + \frac{\Delta X_n}{\Delta z_{sn}}\hat{z}_{sn}}{\sqrt{(\frac{\Delta X_1}{\Delta z_{s1}})^2 + (\frac{\Delta X_2}{\Delta z_{s2}})^2 + \ldots + (\frac{\Delta X_n}{\Delta z_{sn}})^2}} \tag{6.3}$$

where ΔX_i is the variation in XPOL due to an incremental perturbation of the ith coordinate z_{si}, with all others kept constant. The index i varies from 1 to n, where n is the dimension of the space defined by the set of orthogonal vectors $\hat{z}_{s1}, \hat{z}_{s2}, \ldots, \hat{z}_{sn}$.

If we specify the subreflector shape as an interpolation of a discrete set of points (x_{si}, y_{si}, z_{si}), with x_{si} and y_{si} constants, for $i = 1, 2, \ldots, n$, we can represent a

new subreflector shape by a new set of z_{si} values. If the initial subreflector shape is specified by the point P_1 in the n-dimensional space, motion in the direction opposite to $\vec{g_1}$ (i.e., the gradient of X at P_1) will lower the value of X, unless P_1 is already a point where X is locally minimum.

Let P_2 be a point where X assumes the first (i.e., closest to P_1) minimum value in the direction $\vec{g_1}$. The distance between the points P_1 and P_2 is known as the optimum step t [42]. It is optimum in the sense that steps larger than t may yield values for X greater than those presented at P_2.

Once P_2 is determined a new unitary gradient vector $\vec{g_2}$ is calculated and the process is repeated. If, at the end of an iteration, the XPOL performance is below the user's requirement (i.e., stop criterion), the process is terminated. The gradient method normally converges independent of the initial conditions [41], and is highly recommended when the analytical form of the function to be optimized is unknown. These properties, combined with its excellent numerical stability, makes the gradient method specially suitable for our subreflector shaping purposes.

In order to determine the optimum step t, one can use any one-dimensional optimization technique (e.g., searching methods). Note that since the step is relatively large, the "descent" process is not the steepest possible one. However, by calculating an optimum step at each iteration, we guarantee that the necessary number of gradient evaluations is the minimum possible one.

We note that X must be evaluated $(n+1)$ times in order to determine $\vec{g}$ at a given point P of the n-dimensional space, one time to calculate the value of X at P, and n times to compute the variations ΔX_i with respect to that initial value, where $i = 1, 2, \ldots, n$. For each ΔX_i, only the coordinate z_{si} varies, while all others are kept constant with values defined by P. The amount of each variation Δz_{si}, see (6.3), is perhaps the most important parameter in the gradient method.

This variation should not be too large or the approximation of the differential by the difference quotient will not be satisfactory. On the other hand, it should not be lower than a certain minimum or roundoff errors will deteriorate the accuracy of the approximation. For the shaping problems discussed herein, the following values were chosen:

$$\Delta z_{s1} = \Delta z_{s2} = \ldots = \Delta z_{sn} = 0.12\lambda \tag{6.4}$$

This value was chosen based on the fact that this amount of surface perturbation yields reasonable variations of XPOL (e.g., 0.3 dB). However, values in the range $0.05\lambda \leq \Delta z_{si} \leq 0.2\lambda$ also proved to give satisfactory results. In order to avoid a surface discontinuity when z_{si} is perturbed, some points around it are also perturbed. The amount of perturbation is proportional to the distance from the considered point to z_{si}. Of course, this is also a critical parameter, and a careful investigation is required. We choose

$$\begin{aligned} \Delta z_{si+} &= 0.6\,\Delta z_{si} \\ \Delta z_{si++} &= 0.2\,\Delta z_{si} \end{aligned} \tag{6.5}$$

where z_{si+} represents the z_s-coordinates of all points with projections onto the $x_s y_s-$ plane located immediately next to the z_{si} projection. z_{si++} are the points immediately next to the z_{si+} points.

A possible implementation of the proposed technique is to first create all the necessary files describing the perturbed subreflector surfaces. Then, the gradient and

step t are computed based on the results of the analysis performed by GRASP7 on each of those files. Based on that information, a new subreflector shape is determined. Finally, GRASP7 is used to analyze the new geometry, computing the new XPOL. The procedure can be repeated for further improvement.

6.3.2 Numerical Results and Comments

In order to illustrate the procedure we employ the dual offset Gregorian reflector antenna specified in Table 3.4 illuminated by a feed antenna described by (6.1) and (6.2). The feed antenna has a 11 dB taper at 13.38° in the E-plane, $C_{\theta_f}(\theta_f)$, and a 8.5 dB taper at 13.38° in the H-plane, $C_{\phi_f}(\theta_f)$. This produces a feed peak XPOL level of -26.60 dB in the 45°-planes. The resulting co- and cross-polarized reflector patterns computed by GRASP7 in the 45°-planes at 14.25 GHz are shown in Fig. 6.1. We note that the patterns are not symmetrical, with XPOL lobes of -32.71 dB at -0.56° and -32.99 dB at 0.68°. Although not shown, system XPOL is very low in the yz-plane (i.e., XPOL < -45 dB) since the reflector configuration has been optimized for low XPOL. Thus, we conclude that the only XPOL present in the system is due to the feed.

In order to reduce feed XPOL effects, we employ the shaping procedure described in the last section. The patterns shown in Fig. 6.2 were obtained after one iteration; i.e., the gradient was computed one time. A step of 0.855 λ was used to determine the new subreflector shape. Although further XPOL reduction was possible with the use of a larger step, the value of 0.8550 λ was chosen to keep pattern deterioration to a minimum. We note from Fig. 6.2 that the XPOL lobe located at -0.58° was lowered to a satisfactory level, -35.20 dB.

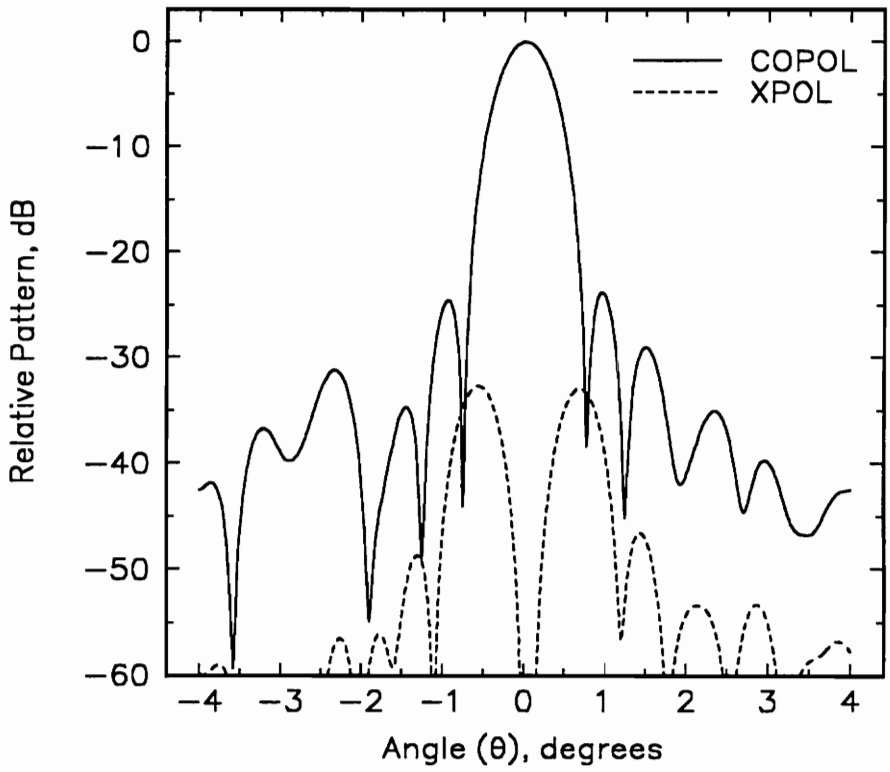

Figure 6.1. Computed co- (solid curve) and cross-polarized (dotted curve) far-field patterns of the dual offset Gregorian configuration specified in Table 3.4 illuminated by a feed with a XPOL level of -26.60 dB. The patterns were computed in the $\phi = 45°$ plane.

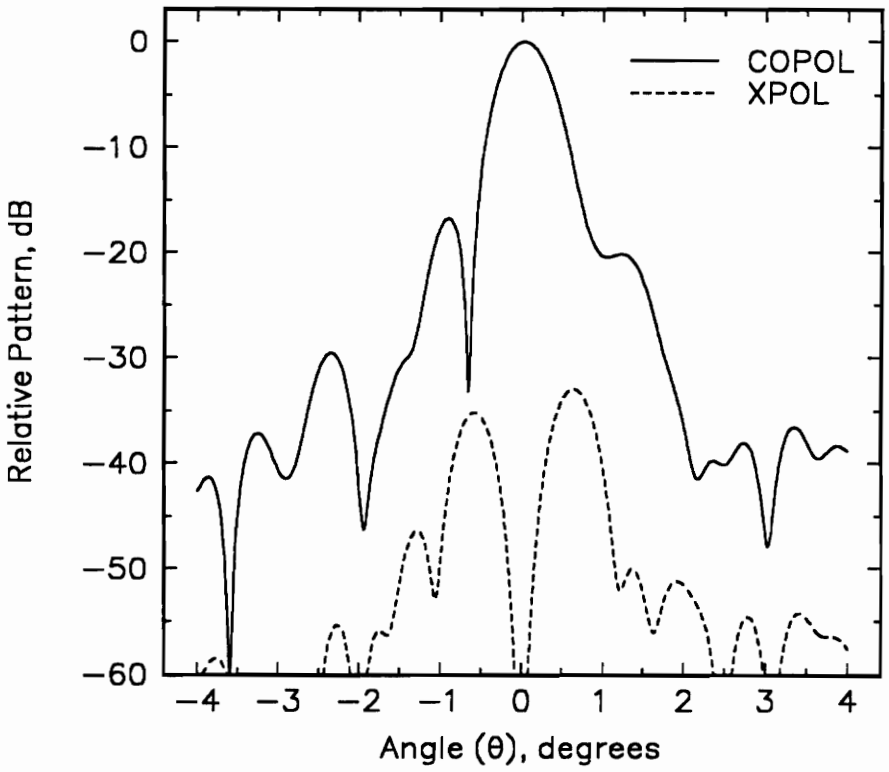

Figure 6.2. Computed co- (solid curve) and cross-polarized (dotted curve) far-field patterns after 1 subreflector shaping iteration; i.e., the gradient was computed one time. The patterns were computed in the $\phi = 45°$ plane.

A second iteration yields the patterns shown in Fig. 6.3. A step of 0.7125 λ was used to determine the final subreflector shape. We note that the patterns are not symmetrical, with XPOL lobes of -35.13 dB at -0.56° and -35.06 dB at 0.62°. As in the first iteration, further XPOL reduction was possible with the use of larger steps. However, it was decided to shape the subreflector just enough to meet the XPOL specifications of -35 dB. Figure 6.4 shows the cross-polarized contour plot computed by GRASP7 for the final configuration. This confirms that XPOL has been reduced to less than -35 dB, at least over the region occupied by the main beam and near-in sidelobes. Each iteration took 6 hours of processing time in a 486 DX2 - 50 MHz. The subreflector was modeled in a grid of 400 points (20x20); see Section 6.3.1 for further information. In order to keep the exposition as clear as possible the details involved with the meshing algorithm and corresponding numerical implementation are not discussed here.

The computed gain of the final configuration is 48.56 dBi, which yields an aperture efficiency of 56.74%. The gain loss is attributed mostly to phase errors, which can be compensated by shaping the main reflector [46]. In this work the shaping of the main reflector is not considered due to the constraint of using an existing main reflector mold; see Chapter 3. The shaped subreflector obtained after the two iterations is shown in Fig. 6.5 and deviates from a perfect ellipsoid as shown in Fig. 6.6. We note that the maximum deviation is approximately 0.5 cm $\approx 0.25\lambda$, which compares well with the amount of deviation obtained in [46]. In addition, the final subreflector is symmetric with respect to the $y_s z_s$-plane (or yz-plane). Due to the relatively small amount of shaping, it was not necessary to constrain the optimization process to yield only continuous and smooth surfaces. This, however, can be accomplished by modeling the subreflector surface with a set of orthogonal expansion functions that guarantee continuity and smoothness [46].

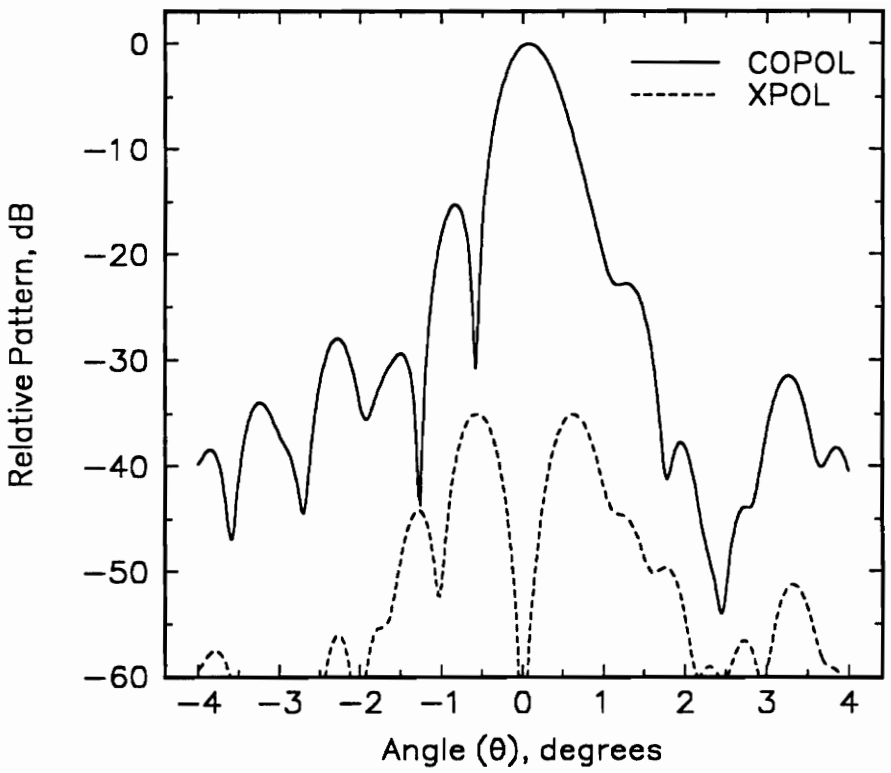

Figure 6.3. Computed co- (solid curve) and cross-polarized (dotted curve) far-field patterns after two subreflector shaping iterations; i.e., the gradient was computed twice. The patterns were computed in the $\phi = 45°$ plane.

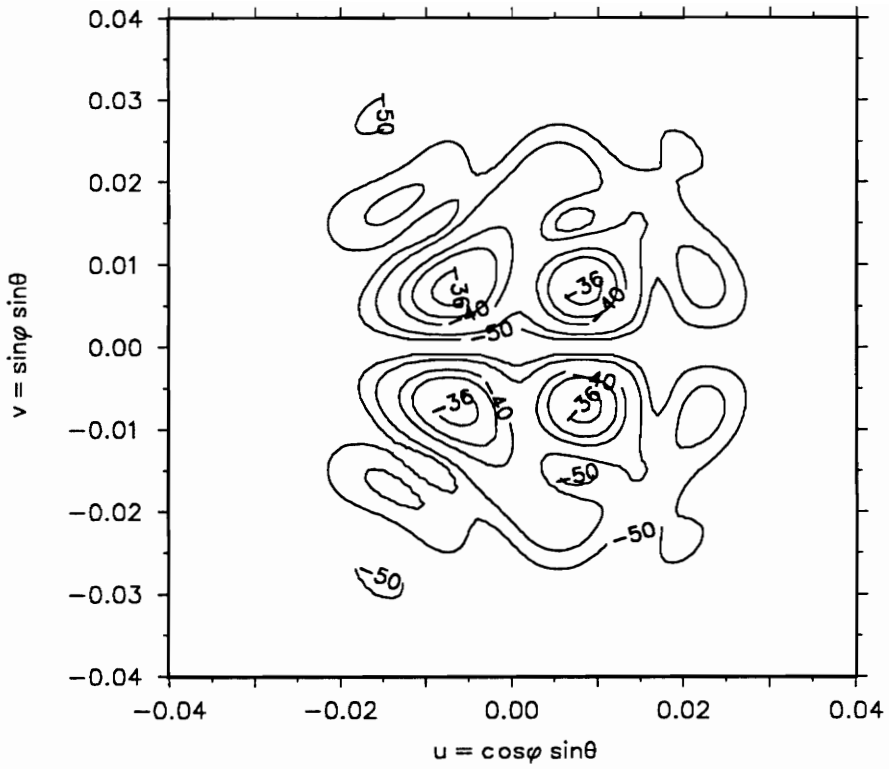

Figure 6.4. Contour plot (dB) of the computed cross-polarized pattern after two subreflector shaping iterations; i.e., the gradient was computed twice.

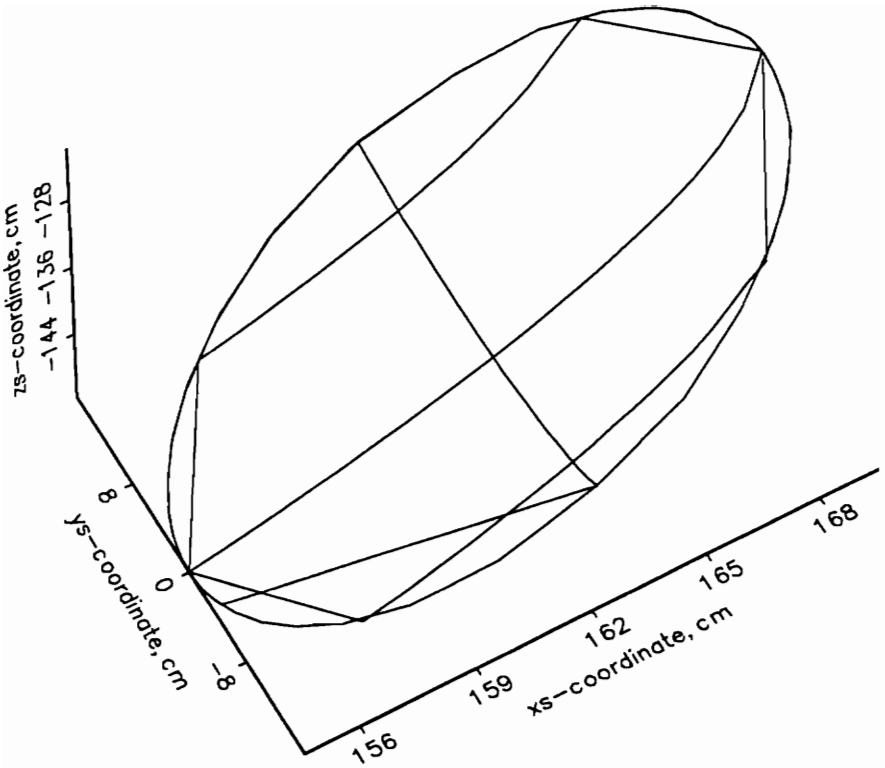

Figure 6.5. 3D view of the shaped subreflector.

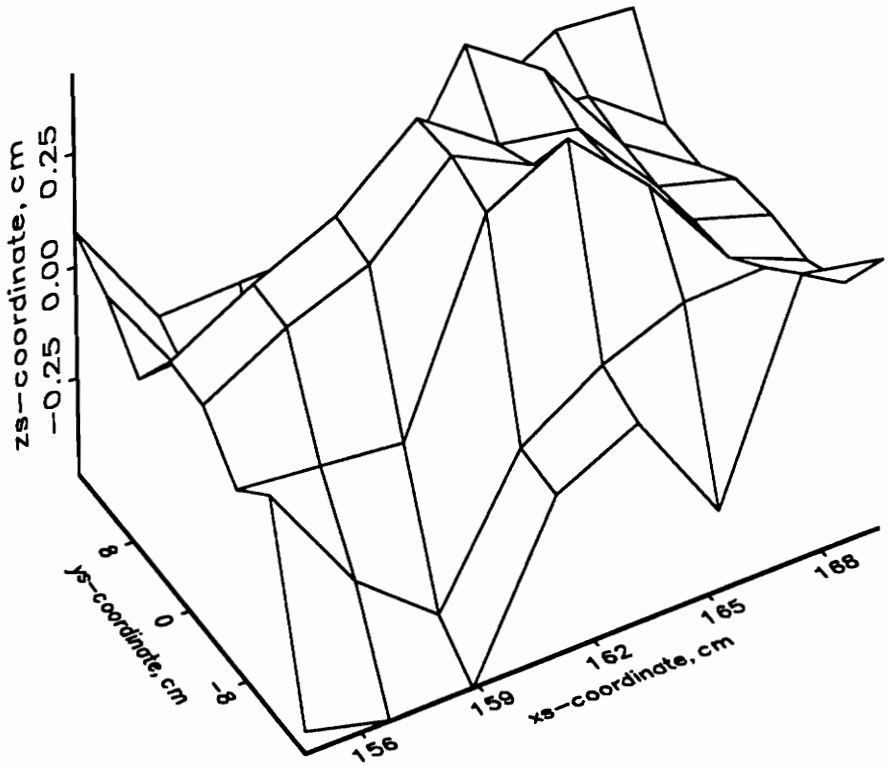

Figure 6.6. Deviation of the shaped subreflector from a perfect ellipsoid.

Although not shown, XPOL remained below -35 dB over the entire transmitting frequency band defined for the EUTELSAT specifications; i.e., from 14.0 GHz to 14.5 GHz [11]. In addition, the resulting configuration also met the -35 dB XPOL specification when illuminated by a purely linearly polarized feed. This shows that the shaping can be based on the frequency where the feed XPOL characteristics are worse.

6.4 Conclusions

In this chapter we investigated the possibility of shaping the subreflector of a dual offset configuration in order to compensate for feed XPOL effects. The employed feed model approximates well the behavior of corrugated conical horns, a class of feed antennas widely used to illuminate reflectors. The shaping algorithm, based on the gradient method, proved to be effective to reduce feed XPOL effects. However, phase errors are introduced by the shaped subreflector, causing gain loss and pattern deterioration. Nevertheless, the resulting configuration was able to meet all EUTELSAT specifications on XPOL and sidelobe levels [11]. Although applied to a specific case example, the shaping algorithm was presented in a generic way and is certainly able to handle other configurations.

It is possible to compensate for a certain amount of feed XPOL through the shaping of both the main reflector and the subreflector [40]. This avoids the pattern deterioration caused by shaping only the subreflector, which might be replaceable by a lens as suggested in [6]. In this work the shaping of the main reflector is not considered due to the constraint of using an existing main reflector mold; see Chapter 3. The problem of shaping only the subreflector of a dual offset reflector system is addressed once more in the next chapter.

Chapter 7

Future Work

7.1 Preliminary Considerations

In this chapter we discuss two original concepts that follow directly from the work performed in this dissertation. One of them, the synthesis technique, is an alternative procedure to the optimization algorithm employed in the last chapter. The other concept is a generalization of the equivalent paraboloid concept described in the Appendix C (Chapter 12). The concepts can form future research topics in the area of reflector antennas.

7.2 The Synthesis Technique

7.2.1 Synthesis Techniques Vs. Optimization Methods

A synthesis technique should yield a solution (i.e., the subreflector shape) directly from the performance specifications. The technique proposed here is a direct closed form process, in contrast to the slower optimization method described in the last section. Also, by using a synthesis technique, it is easier to systematically investigate the domain where solutions possibly exist. This occurs because the behavior of the solutions is described by a known equation or process. Finally, it is always possible to run an optimization algorithm, such as the Gradient Method, once the synthesis process is terminated.

7.2.2 The Physical Optics Formulation

The physical optics approach is completely described in the Appendix A (Chapter 10). Here, only the main results are highlighted. In general, the electric field radiated by a reflector antenna, at a given observation point in the far-field, can be obtained through the solution of the radiation integral [14]

$$\vec{E}(\vec{r}) = -\jmath\frac{\eta_0}{2\lambda}\frac{e^{-\jmath kr}}{r}(\vec{\vec{I}} - \hat{r}\hat{r}) \bullet \int_0^{D/2}\int_0^{2\pi} \vec{J}(\vec{r}\prime) J_\Sigma e^{\jmath k\hat{r}\bullet\vec{r}\prime}\rho\prime\, d\rho\prime\, d\phi\prime \qquad (7.1)$$

where $\hat{r}\hat{r} \bullet \vec{a}$ is shorthand for $\hat{r}(\hat{r} \bullet \vec{a})$, and $(\vec{\vec{I}} - \hat{r}\hat{r})$ is included to remove the radial component (far-field approximation). The vector $\hat{r}$ is given by

$$\hat{r} = \sin\theta\cos\phi\hat{x} + \sin\theta\sin\phi\hat{y} + \cos\theta\hat{z} \qquad (7.2)$$

and $\vec{r\prime} = x\prime\hat{x} + y\prime\hat{y} + z\prime\hat{z}$ represents points over the reflector (primed coordinate system). The quantity $\vec{\vec{I}}$ is referred to as the unit dyad, and is equal to the identity matrix for our purposes. J_Σ is the Jacobian transformation of the surface [13], which simplifies the evaluation of the integral since it now can be performed over a plane instead of the curved surface. $\vec{J}$ is the current distribution over the reflector surface, and is generally obtained using the Physical Optics (P.O.) formulation [12]

$$\vec{J}(\vec{r\prime}) = 2\hat{n} \times \vec{H}_{inc}(\vec{r\prime}) \tag{7.3}$$

where $\vec{H}_{inc}$ is the incident magnetic field on the reflector (from the feed or other source), and $\hat{n}$ is the unit vector normal to the reflector surface.

Thus, once the feed pattern and the dual reflector geometry are known, it is possible to evaluate via (7.1) the far-field of the antenna (co and cross polar components, in magnitude and phase). The process can be performed in two steps. First, we compute the magnetic field radiated by the subreflector based on the information about the feed and subreflector geometry. Then, using that result as the magnetic field incident on the main reflector, (7.1) yields the overall reflector antenna far-field pattern. The computation of the incident magnetic field on the reflectors involves several rotations and translations of coordinate systems, and the Eulerian angles must be employed for generality [47]; see Section 10.3.

7.2.3 Synthesis of Subreflectors in Dual Offset Antennas

We conclude from the last section that it is possible to compute the subreflector physical optics currents once the feed pattern and the subreflector geometry

are described. In this section, we propose a procedure to determine the shape of a subreflector illuminated by a feed with high XPOL, referred to as the shaped case, such that the corresponding radiation pattern is similar to the one produced by a non-shaped subreflector illuminated by a feed free of XPOL, referred to as the canonical case. Our idea is to employ Jacobian transformations in both the canonical and shaped cases such that the two integrals are defined with respect to a polar coordinate system. This polar coordinate system defines a plane on which the subreflector surfaces are mapped. Within this context, we can define equivalent currents on this plane for a canonical case, and then shape the subreflector of the real case in order to produce similar equivalent currents. This leads to the same subreflector radiation patterns in both cases. Therefore, the incident fields on the main reflector are unchanged, yielding the same overall antenna pattern. Since the antenna pattern of the canonical case meets the requirements for XPOL, it is expected that the pattern of the shaped case with the real feed presents similar results.

In addition, instead of enforcing exact equivalent current equality, it is more realistic to allow certain discrepancies. However, these differences must be closely monitored, and therefore a figure of merit is introduced. This figure of merit should indicate how close the equivalent currents from the shaped case are to the currents from the canonical case, therefore giving us control on the amount of XPOL reduction. Also, we may allow the canonical and shaped subreflectors to have slightly different projected apertures, if equality proves to be too restrictive. We note that (7.1) can be modified to handle reflectors with projected apertures other than circular [48]. Different projected apertures are also expected when the Jacobian transformations map the surfaces into planes that are rotated and/or translated with respect to each other. Further studies are necessary to determine the full implication of this approach. In order to investigate the contributions of the different terms in

the kernel of (7.1), it is recommended to separate the terms which are functions of the projected aperture coordinates from the ones dependent on the far-field coordinates. The proposed approach is to employ the Jacobi-Bessel series expansion method [13, 48], used by the author in the development of the Parabolic Reflector Analysis Code (PRAC); see Appendix B (Chapter 11).

7.3 The General Equivalent Reflector System

In this section we suggest a possible generalization of the equivalent reflector theorem discussed in Appendix C (Chapter 12). We first comment on the original formulation of the theorem, which is illustrated in Fig. 7.1(a). The equivalence between the dual offset configuration and the axisymmetric system is obtained only if the dual geometry is illuminated by a balanced feed and is designed according to Mizugutch and Rusch conditions [31]. The main reflector is assumed to have a circular projected aperture. The aperture fields in both systems of Fig. 7.1(a) are equivalent, yielding similar far-field patterns. The dual offset configuration is free of XPOL as discussed in Chapters 2 and 3. Similarly, the axisymmetric system is free of XPOL when illuminated by a balanced feed, as discussed in Chapter 2.

A closer examination of this theorem, however, reveals that the equivalence cannot hold true if the reflectors are shaped. This is because phase errors can only be avoided in the dual system, provided that both the main reflector and subreflector are properly shaped. Shaping of the axisymmetric single reflector will introduce substantial phase errors and, therefore, the shaped systems cannot be equivalent.

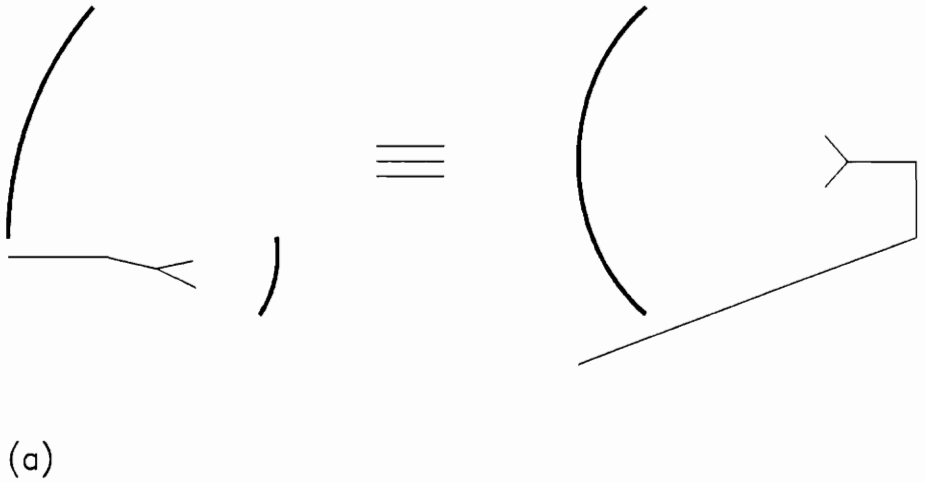

(a)

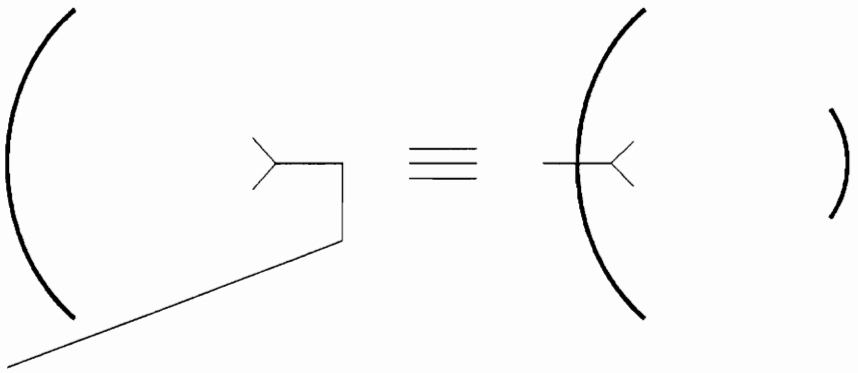

(b)

Figure 7.1. Equivalence between single and dual reflector systems. (a) Equivalence between a dual offset configuration and a single axisymmetric system. (b) Equivalence between a single axisymmetric system and a dual axisymmetric configuration.

A possible generalization of the equivalent reflector theorem is to include the step illustrated in Fig. 7.1(b). As it is well known [12], an axisymmetric reflector is equivalent to a dual axisymmetric system. Thus, we can determine a dual axisymmetric system which is equivalent to the original dual offset configuration, provided that Mizugutch and Rusch conditions are satisfied.

This new formulation suggests the possibility of applying to a dual system the closed form procedures that are only available for shaping dual axisymmetric systems [14, 49, 50]. The numerical procedures available in the literature to shape dual offset systems do not always converge, and research is still being conduct in this area [51, 52]. The basic idea is to shape the subreflector to obtain the desired amplitude distribution across the exit aperture of the main reflector, and then shape the main reflector to recover the uniform phase distribution which was disturbed by shaping the subreflector. It is often desired to obtain a nearly uniform aperture distribution, yielding a high aperture efficiency (e.g., 84.9%) [10].

A possible investigation rationale is to first shape the equivalent dual axisymmetric system with an existing procedure. This is normally accomplished by solving a set of two second-order ordinary differential equations [14]. Once the shaped equivalent axisymmetric system is obtained, the deviation between the shaped reflectors and the original surfaces can be determined. Then, the sum of the main reflector and subreflector deviations can be imposed to be the same in both the equivalent dual axisymmetric system and the original dual offset system. This assures that phase errors are not introduced in the dual offset system. An alternative is to set the main reflector deviation and the subreflector deviation to be individually the same in both systems. The deviations can be determined with respect to the feed axis, the subreflector axis and/or the main reflector axis. A possible contribution of

the proposed equivalent concept is the determination of mapping functions relating shaped axisymmetric and offset systems.

For certain applications, such as the maximization of aperture efficiency, it is sufficient to shape only the subreflector of a dual axisymmetric reflector system. Phase errors can be minimized at one frequency by properly adjusting the distance between the feed phase center and the vertex of the parabolic reflector [53, 54]. This procedure has been successfully implemented in the past to reduce gain loss due to phase errors in Cassegrain systems employing a shaped subreflector for maximum aperture efficiency [53, 54]. However, it may not be as effective for systems designed to present low XPOL, such as the configurations analyzed in the previous chapters. Nevertheless, for applications where gain and aperture efficiency are of main concern, this suggests the possibility of shaping only the subreflector of a dual offset configuration and then relocate the feed to minimize the phase errors. An existing single offset configuration, for example, could be upgraded for maximum aperture efficiency through the addition of a shaped subreflector. This would represent a substantial innovation in the area of reflector antennas. The commercial importance of such approach is enormous, justifying the need for further investigation.

Chapter 8

Conclusions

This chapter summarizes the research reported in this dissertation, emphasizing original contributions. The areas of investigation are highlighted.

Comprehensive Review of XPOL in Reflector Antenna Systems

A comprehensive description of the cross polarization (XPOL) behavior of parabolic reflectors was presented in Chapter 2. Emphasis was given to the offset parabolic reflector illuminated by a balanced circularly polarized (CP) feed. However, both the offset and axisymmetric configurations with linearly polarized (LP) feeds were also considered. The absence of circular XPOL in offset parabolic reflectors larger than 12 λ in diameter and illuminated by CP feeds was explained in Section 2.3.2.

Beam squint and beam deviation (scanning) phenomena were presented in Section 2.4 and the former was examined and explained in detail. Agreement between

computations and predictions using the simple model of (2.24) with measured beam squint values obtained from the literature for the study case was excellent (see Fig. 2.13 and Section 2.4). Although many of the phenomena are known, they were explained in new ways and presented in a single coherent treatment [33].

There are a large number of possible reflector geometries, feed types, locations, and polarizations. Representative configurations were examined to provide specific values as well as general conclusions. The many possible configurations are summarized in Table 2.6 together with XPOL, beam squint, and beam deviation effects [33]. Table 2.6 shows that unbalanced feeds (i.e., the primary radiation pattern is not symmetric) usually generate substantial XPOL independent of the feed polarization or reflector configuration. Also, displacing the feed from the focal point normally generates XPOL and beam deviation. Most of the results presented in Table 2.6 were verified in this work.

Cross polarization can be significantly reduced by using a small feed pointing angle, ψ_f [3, 4]. However, small angles lead to high spillover and gain loss, as shown in Fig. 2.9. Thus, high cross polarization in single offset reflectors illuminated by conventional feeds can be expected if high gain is to be maintained [3, 4]. A XPOL level of about -22 dB, which is typical of single offset paraboloids [4, 33, 36, 37], is often unacceptably high. There are a few procedures available in the literature to reduce XPOL in single offset reflectors [5, 6]. However, they require the design and manufacturing of special feeds [5], lenses [6] and/or shaped reflectors [6]. This can lead to costly design and production, especially for wideband systems. The approach investigated in this dissertation was the addition of a subreflector to the single offset system, as addressed next.

Upgrading Single Reflectors to Low XPOL Dual Reflectors

The suggested cost-effective method to improve the performance of an existing offset prime-focus reflector was to add a subreflector, forming a dual reflector system with very low cross polarization, as discussed in Chapter 3. All requirements and specifications for the upgrading procedure are summarized in Section 3.2. The motivation to use a specified main reflector often arises from a desire to use an existing mold which is usually very expensive. A general procedure was presented in Section 3.4 for upgrading single offset reflectors to dual reflectors to achieve low cross polarization. The problem consists of adding a subreflector to an existing family of offset paraboloids in order to achieve a low level of linear cross polarization (e.g., -35 dB). The synthesis procedure takes into account the XPOL characteristics of conventional, low-cost feeds and, in order to reduce manufacturing costs, produces a design with adequate clearance between the bottom of the main reflector and the feed axis. In addition, the resultant configuration operates with either a LP or a CP feed without the need of being repositioned (no substantial beam squint). These constraints are not taken into account by other design procedures.

Practical examples were presented in Sections 3.6.1 and 3.6.2 to validate the design procedures. The single reflectors correspond to real systems commercialized by a major reflector antenna manufacturer; see Tables 3.2 and 3.4, and Fig. 3.5 [36, 37]. The measured data were provided by the manufacturer, and all computed data were obtained with the Virginia Tech code PRAC and the commercial code GRASP7. The dual configurations designed in Chapter 3 are the results of our efforts to upgrade the existing single reflectors to low cross-polarized dual reflector antennas; see Tables 3.3 and 3.4, and Figs. 3.6, 3.7 and 3.8 [36, 37].

Influence of Feed XPOL and Feed Rotation for XPOL Reduction

It was shown in Chapter 4 that the XPOL of dual offset Gregorian antennas designed for low XPOL is generally limited by the feed XPOL. Equation (4.5) can be used to determine the minimum feed XPOL level necessary to achieve a required specification of system XPOL. Nevertheless, a suitable computer code should be used to validate the electrical performance values.

The possibility of reducing feed XPOL by rotating the feed was investigated in detail in Section 4.4. The procedure was effective for the feed model considered in Section 4.2 and, while it may not be completely realistic, it illustrates that the rotation technique can be useful in some applications.

Enforcement of Practical Manufacturing Constraints

We introduced in Chapter 5 a procedure to rotate the parent ellipsoidal subreflector. This was necessary to achieve clearance between the bottom of the main reflector and the feed axis in our study configuration. Manufacturing costs can be substantially reduced through the enforcement of this condition, which is not addressed in the literature and was brought to our attention by a large scale manufacturer of reflector antennas.

Although effective for achieving suitable clearance in the feed region, rotation of the subreflector introduces substantial XPOL in a system designed to present low XPOL. A possible solution, proposed in Section 5.4, was to replace the subreflector by one of higher eccentricity, producing a design with the desired XPOL performance and adequate clearance between the main reflector and feed axis (see Figs. 5.9, 5.10

and 5.11). Also, the resulting design has large operational bandwidth since the feed was relocated to the focal point of the new ellipsoidal subreflector, avoiding the introduction of phase errors. Table 5.6 summarizes all the necessary steps developed in Chapters 3 and 5 for upgrading an existing single offset reflector to a low cross-polarized, dual offset reflector antenna with adequate clearance between the main reflector and feed axis.

XPOL Reduction by Subreflector Shaping

Reduction of feed XPOL effects by subreflector shaping was examined in Chapter 6 for the feed model of Section 6.2. This model approximates well the behavior of corrugated conical horns, a class of feed antennas widely used to illuminate reflector configurations. The shaping algorithm, based on the gradient method, was explained in Section 6.3.1 and proved to be effective to reduce feed XPOL effects. However, phase errors are introduced by the shaped subreflector, causing gain loss and pattern deterioration (see Fig. 6.3). Nevertheless, the resulting configuration was able to meet all EUTELSAT specifications on XPOL and sidelobe levels [11]. Although applied to a specific case example, the shaping algorithm was presented in a generic way and is certainly able to handle other configurations.

The phase errors introduced by the shaping process can be compensated with the shaping of the main reflector [46]. This was not performed in this work due to the constraint of using an existing main reflector mold; see Chapter 3. Nevertheless, all non-conventional, dual reflector configurations presented in this dissertation can be used as starting points of a dual-reflector shaping process, if further improvements are desired.

Development of Computer Codes

All innovative design algorithms developed in this dissertation were implemented as numerical codes forming the DORA package (Dual Offset Reflector Antenna Synthesis Package). DORA is a complete suite of codes for the synthesis of non-conventional, low-cost dual offset Gregorian reflector antennas with very low cross polarization. Several practical case examples were discussed, including a performance assessment of the largest steerable radio telescope in the world, the Green Bank Radio Telescope located in Green Bank, West Virginia.

The electrical performance of the Green Bank Telescope (GBT) reflector antenna was evaluated in Section 5.5 with the commercial code GRASP7 and the Virginia Tech code PRAC (see Table 5.4 and Fig. 5.12). In addition, the Virginia Tech code DORA was employed to upgrade the GBT single offset configuration to a low cross-polarized dual offset Gregorian reflector configuration (see Table 5.5). The geometrical parameters determined with DORA are in very good agreement with the ones published in [7]. New dual configurations for the GBT offset reflector can be obtained with DORA for different design parameters, such as a new subreflector size. All designs are optimized for low cross polarization. The computer simulations confirmed a low XPOL level when the dual configuration is illuminated by a purely polarized feed antenna, as shown in Table 5.5 and Fig. 5.13. A feed antenna with high XPOL will likely degrade the total system XPOL performance.

A compendium of various methods for the analysis of reflector antennas was presented in a historical fashion in Appendix A (Chapter 10). In particular, the physical optics approximation [12] and the Jacobi-Bessel series expansion method [13, 14] were discussed in detail. These formulations were numerically implemented

by the author in the Parabolic Reflector Analysis Code, PRAC, which is completely described in Appendix B (Chapter 11).

PRAC is a user friendly code developed to analyze parabolic reflector antennas, both axisymmetric and offset. PRAC evaluates the radiation integral (physical optics surface current integration) with the Jacobi-Bessel method and yields the co- and cross-polarized radiated fields with high accuracy and efficiency. The effectiveness of PRAC was confirmed by extensive comparisons with measured data and results available in the literature and/or obtained with the commercial code GRASP7; see Figs. 3.5 and 5.12, and Tables 3.2, 5.4, 11.2, and 11.5 [36, 37].

PRAC permits the analysis of parabolic reflector antennas with any circular projected diameter, any focal length, and any offset distance. The user can specify the reflector geometry in centimeters, meters, inches or feet. The linearly polarized feed can be pointed in any direction. Small feed displacements from the focal point are also allowed. PRAC offers a complete integrated environment with menus of options, data input fields, and an on-line help system available at each step of the program. In addition, a comprehensive user's manual is included in Appendix B (Chapter 11).

Concise Summary of Applications

The results and algorithms developed and presented in this dissertation have a wide range of applications. First, they can be used for the design and production of non-conventional, low-cost commercial reflector antennas. Nevertheless, the same procedures can be employed for the design of large and/or specialized reflector systems, such as the Green Bank Radio Telescope. In any case, low cross polarization was always the principal design parameter, although an effort was made to keep track of other electrical parameters, such as aperture efficiency and sidelobe level.

In addition, educational use was also a main concern while developing the present work. Table 2.6, for example, presents a complete overview of the various depolarization properties of single parabolic reflector antennas. We have also included in Chapter 2 new, simpler ways to interpret and explain the phenomena of cross polarization and beam squint. These results combined with the developed user friendly code, PRAC, represent substantial resources to aid professors to teach reflector antennas at both basic and advanced levels. This is also considered as a relevant contribution of this dissertation since reflector antennas represent a substantial part of the present antenna market, with many jobs being offered specifically to reflector antenna engineers.

Chapter 9
References

[1] A.C. Ludwig, "The Definition of Cross Polarization", *IEEE Trans. Antennas Propagat.*, pp. 116-119, Jan. 1973.

[2] A.H. Rana, J. McCoskey, and W. Check, "VSAT technology, trends, and applications", *Proc. of the IEEE*, vol. 78, no.7, pp. 1087-1095, July 1990.

[3] Y. Rahmat-Samii, "Reflector Antennas" in Y.T. Lo and S.W. Lee (eds.), *Antenna Handbook*, New York, Van Nostrand Reinhold Co., 1988, Chapter 15.

[4] M.A. Terada and W.L. Stutzman "Design of Offset-Parabolic-Reflector Antennas for Low Cross-Pol and Low Sidelobes", *IEEE Antennas and Propagation Magazine*, vol. 35, no. 6, pp, 46-49, Dec. 1993.

[5] A.W. Rudge and N.A. Adatia, "A new primary feed for offset reflector antennas", *Electron. Lett.*, vol. 11, pp. 597-599, Nov. 1975.

[6] E. Lier and S.A. Skyttemyr, "A shaped single reflector offset antenna with low cross-polarization fed by a lens horn", *IEEE Trans. Antennas Propagat.*, vol. 42, no. 4, pp. 478-483, Apr. 1994.

[7] S. Srikanth, "Comparison of Spillover Loss of Offset Gregorian and Cassegrain Antennas", *IEEE Antennas Propagat. Soc. Symp. Dig.* (London, England), pp. 444-447, June 1991.

[8] R. Hall and L.J. King, "The Green Bank Telescope", *IEEE Antennas Propagat. Soc. Symp. Dig.* (Chicago, IL), pp. 862-865, July 1992.

[9] A.W. Love, Editor, *Reflector Antennas*, IEEE Press, New York 1978.

[10] Alan G. Cha, "Preliminary Announcement of an 85 Percent Efficient Reflector Antenna", *IEEE Trans. Antennas Propagat.*, pp. 341-342, vol. AP-31, no. 2, Mar. 1983.

[11] EUTELSAT Standard 3 defined in the SMS Specification BS 7-40, Rev 2E, March 1990.

[12] W.L. Stutzman and G.A. Thiele, *Antenna Theory and Design*, John Willey and Sons, New York, 1981.

[13] Y. Rahmat-Samii and V. Galindo-Israel, "Shaped Reflector Antenna Analysis Using the Jacobi-Bessel Series", *IEEE Trans. Antennas Propagat.*, pp. 425-435, July 1980.

[14] C. Scott, *Modern Methods of Reflector Antenna Design*, Artech House, Boston, 1990.

[15] TICRA Eng., *GRASP7-Single and dual reflector antenna program package*, Copenhagen, Denmark.

[16] Y. Mizugutch, M. Akagawa, and H. Yokoi, "Offset dual reflector antenna", *IEEE Antennas Propagat. Soc. Symp. Dig.* (Amherst, MA), pp. 2-5, Oct. 1976.

[17] W.L. Stutzman, *Polarization in Electromagnetic Systems*, Artech House: Boston, 1993.

[18] Rudge et al., editors, *The Handbook of Antenna Design*, Peter Peregrinus, London, 1982.

[19] Y. Rahmat-Samii, "A Comparison Between GO/Aperture-Field and Physical-Optics Methods for Offset Reflectors", *IEEE Trans. Antennas Propagat.*, vol. AP-32, pp. 301-306, Mar. 1984.

[20] P.H. Pathak, *Techniques for High-Frequency Problems*, Chapter 4 in Y.T. Lo and S.W. Lee (eds.), *Antenna Handbook*, New York, Van Nostrand Reinhold Co., 1988.

[21] N.C. Albertsen and K. Pontoppidan, "Analysis of Subreflectors for Dual Reflector Antennas", *IEE Proc.*, Pt. H, vol. 131, no. 3, pp. 205-213, June 1984.

[22] Y. Rahmat-Samii, P.O. Iversen and D.W. Duan, "GTD, PO, PTD, and Gaussian Beam Diffraction Analysis Techniques Applied to Reflector Antennas", *Applied Computational Electromagnetics Society Journal*, vol. 6, pp. 6-30, Summer 1991.

[23] S. Silver, "Microwave Antenna Theory and Design", M.I.T. Radiation Lab. Series, vol. 12, McGraw-Hill, New York, 1949.

[24] T.S. Chu and R.H. Turrin, "Depolarization Properties of Offset Reflectors Antennas", *IEEE Trans. Antennas and Propagat.*, vol. AP-21, pp. 339-345, May 1973.

[25] A.W. Rudge and N.A. Adatia, "Offset-Parabolic-Reflector Antennas: A Review", *Proceedings of the IEEE*, vol. 66, pp. 1592-1618, Dec. 1978.

[26] J. Dijk, C.T.W. van Dic, E.J. Maanders, and L.F.G. Thurlings, "The polarization losses of offset paraboloid antennas", *IEEE Trans. Antennas and Propagat.*, vol. AP-22, pp. 513-520, July 1974.

[27] D.W. Duan and Y. Rahmat-Samii, "Beam Squint Determination in Conic-Section Reflector Antennas with Circularly Polarized Feeds", *IEEE Trans. Antennas and Propagat.*, vol. 39, pp. 612-619, May 1991.

[28] D. Fiebig and W.V.T. Rusch, et.al., "Beam Squint in Axially Symmetric Reflector Antennas with Laterally Displaced Feeds", *IEEE Trans. Antennas and Propagat.*, vol. 39, pp. 774-779, June 1991.

[29] A.G.P. Boswell and R.W. Ashton, "Beam Squint in a Linearly Polarized Offset Parabolic Reflector", *Electron. Lett.*, vol. 12, pp. 596-597, Oct. 1976.

[30] A.W. Rudge and N.A. Adatia, "Beam Squint in Circularly Polarized Offset-Reflector Antennas", *Electron. Lett.*, vol. 11, pp. 513-515, Oct. 1975.

[31] W.V.T. Rusch, A. Prata, Jr., Y. Rahmat-Samii, and R.A. Shore, "Derivation and application of the equivalent paraboloid for classical offset Cassegrain and Gregorian antennas", *IEEE Trans. Antennas Propagat.*, vol. 38, no. 8, pp. 1141-1149, Aug. 1990.

[32] K.W. Brown, Y.H. Lee, and A. Prata, Jr., "A systematic design procedure for classical offset dual reflector antennas with optimal electrical performance", *IEEE Antennas Propagat. Soc. Symp. Dig.* (Ann Arbor, MI), pp. 772-775, July 1993.

[33] M.A.B Terada and W.L. Stutzman, "Cross polarization and beam squint in single and dual offset reflector antennas", to appear in *Electromagnetics Journal.*

[34] C. Dragone, "Offset Multireflector Antennas with Perfect Pattern Symmetry and Polarization Discrimination", *Bell Syst. Tech. J.*, vol. 57, no. 7, pp. 2663-2684, Sept. 1978.

[35] V. Jamnejad-Dailami and Y. Rahmat-Samii, "Some important geometrical features of conic-section-generated offset reflector antennas", *IEEE Trans. Antennas and Propagat.*, vol. AP-28, no. 6, pp. 952-957, Nov. 1980.

[36] M.A.B. Terada and W.L. Stutzman, "High Performance, Low Cost Reflector Antennas", *IEEE Antennas Propagat. Soc. Symp. Dig.* (Newport Beach, CA), pp. 1672-1675, June 1995.

[37] M.A.B. Terada and W.L. Stutzman, "Computer-Aided Design of Reflector Antennas", to appear in the *Microwave Journal.*

[38] W.V.T. Rusch, "The Current State of the Reflector Antenna Art", *IEEE Trans. Antennas Propagat.*, vol. 32, no. 4, pp. 313-329, Apr. 1984.

[39] A.W. Rudge, T. Pratt, and A. Fer, "Cross-polarized radiation from satellite antennas", *AGARD Conf. Proc.*, no. 139, Munich, Germany, pp. 16.1-16.9, Nov. 1973.

[40] B.S. Westcott and F. Brickell, "Dual offset reflectors shaped for zero cross polarization with asymmetric feed pattern", *IEE Proc.*, Pt. H, vol. 129, no. 6, pp. 307-314, Dec. 1982.

[41] D.E. Kirk, *Optimal Control Theory*, Prentice-Hall, New Jersey, 1970.

[42] F.M. Landstorfer and R.R. Sacher, *Optimization of Wire Antennas*, John Wiley and Sons, London, 1986.

[43] R.A. Shore, "A Simple Derivation of the Basic Design Equation for Offset Dual Reflector Antennas with Rotational Symmetry and Zero Cross Polarization", *IEEE Trans. Antennas Propagat.*, vol. AP-33, no. 1, pp. 114-116, Jan. 1985.

[44] P.J.B. Clarricoats and A.D. Olver, *Corrugated Horns for Microwave Antennas*, Peter Peregrinus Ltd., London, 1984.

[45] E. Kreyszig, *Advanced Engineering Mathematics*, John Wiley and Sons, New York, 1978.

[46] D.W. Duan and Y. Rahmat-Samii, "A Generalized Diffraction Synthesis Technique for High Performance Reflector Antennas", *IEEE Trans. Antennas Propagat.*, vol. 43, no. 1, pp.27-40, Jan. 1995.

[47] Y. Rahmat-Samii, "Useful Coordinate Transformations for Antenna Aplications", *IEEE Trans. Antennas Propagat.*, pp. 571-574, July 1979.

[48] Y. Rahmat-Samii, "Jacobi-Bessel Analysis of Reflector Antennas with Elliptical Apertures", *IEEE Trans. Antennas Propagat.*, pp.1070-1074, Sep. 1987.

[49] V. Galindo-Israel, "Design of Dual-Reflector Antennas with Arbitrary Phase and Amplitude Distributions", *IEEE Trans. Antennas Propagat.*, pp. 403-408, July 1964.

[50] B.S. Westcott, *Shaped Reflector Antenna Design*, John Wiley and Sons, London, 1983.

[51] V. Galindo-Israel, W.A. Imbriale, and R. Mittra, "On the Theory of the Synthesis of Single and Dual Offset Shaped Reflector Antennas", *IEEE Trans. Antennas Propagat.*, pp. 887-896, Aug. 1987.

[52] P.S. Kildal, "Synthesis of Multireflector Antennas by Kinematic and Dynamic Ray Tracing", *IEEE Trans. Antennas Propagat.*, pp. 1587-1599, Oct. 1990.

[53] G.W. Collins, "Shaping of Subreflectors in Cassegrainian Antennas for Maximum Aperture Efficiency", *IEEE Trans. Antennas Propagat.*, pp. 309-313, May 1973.

[54] S. Parekh, "On the Solution of Best Fit Paraboloid as Applied to Shaped Dual Reflector Antennas", *IEEE Trans. Antennas Propagat.*, pp. 560-564, July 1980.

[55] A.C. Ludwig, "Computation of Radiation Patterns Involving Numerical Double Integration", *IEEE Trans. Antennas Propagat.*, pp.767-769, November 1968.

[56] R.J. Pogorzelski, "A New Integration Algorithm and its Application to the Analysis of Symmetrical Cassegrain Microwave Antennas", *IEEE Trans. Antennas Propagat.*, pp.748-755, September 1983.

[57] W.V.T. Rusch and P.D. Potter, *Analysis of Reflector Antennas*, Academic Press, New York, 1970.

[58] O.M. Bucci, et al., "Fast Analysis of Large Antennas - A New Computational Philosophy", *IEEE Trans. Antennas Propagat.*, pp.306-310, May 1980.

[59] Y. Rahmat-Samii and R.L.T. Cheung, "Nonuniform Sampling Techniques for Antenna Applications", *IEEE Trans. Antennas Propagat.*, pp.268-279, March 1987.

[60] V. Galindo-Israel and R. Mittra, "A New Series Representation for the Radiation Integral with Application to Reflector Antennas", *IEEE Trans. Antennas Propagat.*, pp.631-641, September 1977.

[61] R. Mittra, Y. Rahmat-Samii, and V. Galindo-Israel, "An Efficient Technique for the Computation of Vector Secondary Patterns of Offset Paraboloid Reflectors", *IEEE Trans. Antennas Propagat.*, pp.294-304, May 1979.

[62] R. Mittra, W.L. Ko, and M.S. Sheshadri, "A Transform Technique for Computing the Radiation Pattern of Prime-Focal and Cassegrain Reflector Antennas", *IEEE Trans. Antennas Propagat.*, pp.520-524, May 1982.

[63] C.C. Hung and R. Mittra, "Secondary Pattern and Focal Region Distribution of Reflector Antennas under Wide-Angle Scanning", *IEEE Trans. Antennas Propagat.*, pp.756-763, September 1983.

[64] W.L. Stutzman, S.W. Gilmore, and S.H. Stewart, "Numerical Evaluation of Radiation Integrals for Reflector Antenna Analysis Including a New Measure of Accuracy", *IEEE Trans. Antennas Propagat.*, pp.1018-1023, July 1988.

[65] F. Zernike, *Physica*, 1 (1934), p.689.

[66] W.L. Stutzman, S. Stewart, and T. Pratt, *Innovative Design of Satellite Earth Terminal Antennas*, Virginia Tech, Satellite Communications Group Report No. T85-4, November 1985.

[67] H. Goldstein, *Classical Mechanics*, pp. 107-109, Addison-Wesley, MA, 1953.

[68] V. Jamnejad, "A New Integration Scheme for Application to the Analysis of Reflector Antennas", *1984 IEEE Symp. Antennas and Propagation Digest*, pp.380-384, Boston, MA, June 1984.

[69] TriMetrix, Inc., *AXUM: Technical Graphics and Data Analysis*, version 3.0, 1993.

Chapter 10

Appendix A: Analysis of Reflector Antennas

10.1 Preliminary Considerations

This Appendix presents a compendium of various methods for the analysis of reflector antennas. In particular, the physical optics approximation [12] and the Jacobi-Bessel series expansion method [13, 14] are discussed in detail. These formulations were implemented numerically by the author in the Parabolic Reflector Analysis Code, PRAC, which is described in the Appendix B (Chapter 11).

10.2 The Evolution of Reflector Antenna Analysis Methods

There has been a steady and large stream of publications on reflector analysis and design techniques for several decades with no sign of decrease. This is because reflector antennas offer extremely high gain and narrow beamwidth from a simple

electrical feed system. The large electrical aperture has caused the development of sophisticated integration techniques, revolutionizing the way radiation patterns are calculated. We present in this introduction a brief summary of the well known techniques, including a comprehensive overview of the Jacobi-Bessel expansion method which is the main purpose of the present study.

One of the earliest techniques for the numerical evaluation of the radiation integral is the Ludwig method [55]. It is very simple to understand and easy to implement as a computer code, although it is not as nearly efficient or mathematically sophisticated as some of the other methods [14]. However, the generality of the method makes it a very versatile tool for analyzing a wide variety of reflector antennas. Also, the Ludwig method has historical value as the predecessor of other integration techniques, like the quadratic phase method of Pogorzelski [56]. The latter is really a generalization of the former, in the sense that the rapidly varying phase terms are approximated by quadratic functions, instead of the linear functions used in the Ludwig algorithm.

One of the first approaches to an analytical evaluation of the radiation integral was presented by Rusch [57]. In this approach, the feed pattern and the reflector surface are expressed analytically, and the resulting radiation integral is also evaluated analytically. However, it is limited to axisymmetric reflectors.

The so called sampling methods represent a variety of approaches which seek to calculate the radiation pattern by interpolating the radiated field at certain sparsely located points in space [58, 59]. However, these methods do not employ ordinary interpolation techniques, but make use of the Whittaker-Shannon sampling theorem [14].

Finally, we get to the series expansion based methods: The Jacobi-Bessel method [60, 61, 13] and the Fourier-Bessel method [62, 63]. In both cases, the aper-

ture and far-field variables are separated in the radiation integral. First, the slowly varying aperture current distribution is expressed as a sum over a set of orthogonal functions defined on the antenna aperture. Then, each of the basis functions is integrated against the Fourier kernel over the aperture. These integrals are closed-form functions of the far-field coordinates, and therefore the radiation integral can be expressed directly in terms of the far-field angles and the aperture expansion coefficients.

Numerical integration is required only for evaluating the expansion coefficients, which are functions exclusively of the feed and reflector geometry characteristics. Also, standard integration routines may now be used, since the integrand is no longer highly oscillatory [13]. A valuable comparison study between popular numerical integration methods can be found in [64]. Thus, once the aperture expansion coefficients are known, the far-field pattern can be computed at any observation angle without the need for time consuming numerical integrations. This scheme forms the basis of most modern reflector antenna analysis techniques, and is in contrast to the direct evaluation of the radiation integral which has to be computed repeatedly for each observation point.

It is worth noting that there are two main considerations affecting the choice of the aperture basis functions. The choice of a basis set that best represents the aperture current distribution with the least number of functions, and the choice of a basis set that is easily integrable against the Fourier kernel. In this work, the chosen expansion functions are the modified Jacobi polynomials.

The Jacobi-Bessel method is based in part on the work performed much earlier by Zernike [65] in connection with the theory of aberrations in optical systems. Thus, the method actually integrates classical optics with modern antenna theory. In

the present work, the Jacobi-Bessel method is presented through a rigorous analytical description and applied to axisymmetric and offset parabolic configurations.

The Jacobi-Bessel method is perhaps the mathematically most complex method for the analysis of reflector antennas. The other series expansion based method, the Fourier-Bessel method is much simpler mathematically and has the additional advantage of being able to employ existing Fast Fourier Transform (FFT) algorithms. However, the Jacobi-Bessel method has been proved to be more efficient in dealing with shaped reflectors [13]. Although the developed code, PRAC (Parabolic Reflector Analysis Code), deals only with parabolic reflectors, it can be easily upgraded due to its open architecture.

10.3 The Physical Optics Formulation

As already commented in Section 10.1, the Jacobi-Bessel method reduces the time associated with the numerical evaluation of the radiation integral through the expansion of the aperture current distribution into a sum of modified Jacobi polynomials. In fact, we first express the radiation integral in terms of a summation of Fourier transforms and then use the Jacobi-Bessel series to evaluate them. In this process, it is necessary to first compute the aperture current distribution which is defined by the primary feed pattern and the type of reflector surface.

A standard way to obtain the current distribution on the reflector surface is by employing the physical optics approximation [12]. The currents can then be integrated to yield the radiation patterns. However, the use of a Jacobian transformation eases the integration process considerably [13]. In that case, the surface

currents can be integrated over the reflector projected aperture instead of the curved reflector surface. We note that the current is evaluated on the reflector surface, but the integral is performed over the aperture through the Jacobian transformation (physical optics/aperture integration). This is different than the aperture field method where the aperture distribution is obtained from the boundary conditions imposed on the electromagnetic fields over the aperture (geometrical optics/aperture integration) [14].

As already commented, we use the physical optics (P.O.) approximation to obtain the current distribution on the reflector surface. This approximation yields the current as the one that would be induced on an infinite tangent conducting plane, at the point where the scattering by the illumination of an infinite plane wave takes place [12]. Also, the fields over the shadowed region of the surface are assumed to be zero.

The P.O. approach is reportedly more accurate than other methods (e.g., geometrical optics), especially for the determination of the cross-polarized fields [19]. Since these are of main importance for the present study, physical optics was employed by GRASP7 and PRAC in all computer simulations presented in this dissertation. Furthermore, only the main lobe and near-in sidelobes are considered, since the method fails to determine the far-out sidelobes and backlobe region accurately. However, this is acceptable for our study since the far-out pattern region is not of primary interest when analyzing high-gain antennas, such as the reflector antennas considered here. For more accurate evaluation at large off-axis angles, the P.O. currents can be augmented with the appropriate singular edge currents [20, 21, 22, 60]. It is remarkable that despite the simplicity of this approximation, it yields results for the scattered field which are in close agreement with measured results [14], at least

for the main beam region and the near-in side lobes. The physical optics current $\vec{J}$ is given by [12]

$$\vec{J} = 2\hat{n} \times \vec{H}_f(\vec{r}\prime) \tag{10.1}$$

where $\vec{H}_f$ is the incident magnetic field on the reflector (from the feed, subreflector or other source), and $\hat{n}$ is the unit vector normal to the reflector surface. The primed coordinate system is the reflector local coordinate system. The reflector surface is described in rectangular or spherical coordinates, and its projection in polar coordinates; see Fig. 10.1 and Table 2.1 for definition of symbols. Figure 10.1 is similar to Fig. 2.1, Section 2.2.1, and is reprinted here for convenience.

We start by explaining a methodology to obtain the term $\vec{H}_f$ in the right-hand side of (10.1). We assume that $\vec{H}_f$ must be computed only at a discrete number of points over the projected aperture plane; these points are herein referred to as sampling points. This assumption is correct since a numerical integration is to be performed over the aperture plane. Furthermore, the sampling points are determined based on the chosen integration algorithm; see Section 11.2.1 for further details. For a given point $(\rho\prime, \phi\prime)$, the rectangular coordinates $(x\prime, y\prime, z\prime)$ can be computed from the relations

$$x\prime = \rho\prime \cos\phi\prime \tag{10.2}$$

$$y\prime = \rho\prime \sin\phi\prime \tag{10.3}$$

$$z\prime = f(\rho\prime, \phi\prime) \tag{10.4}$$

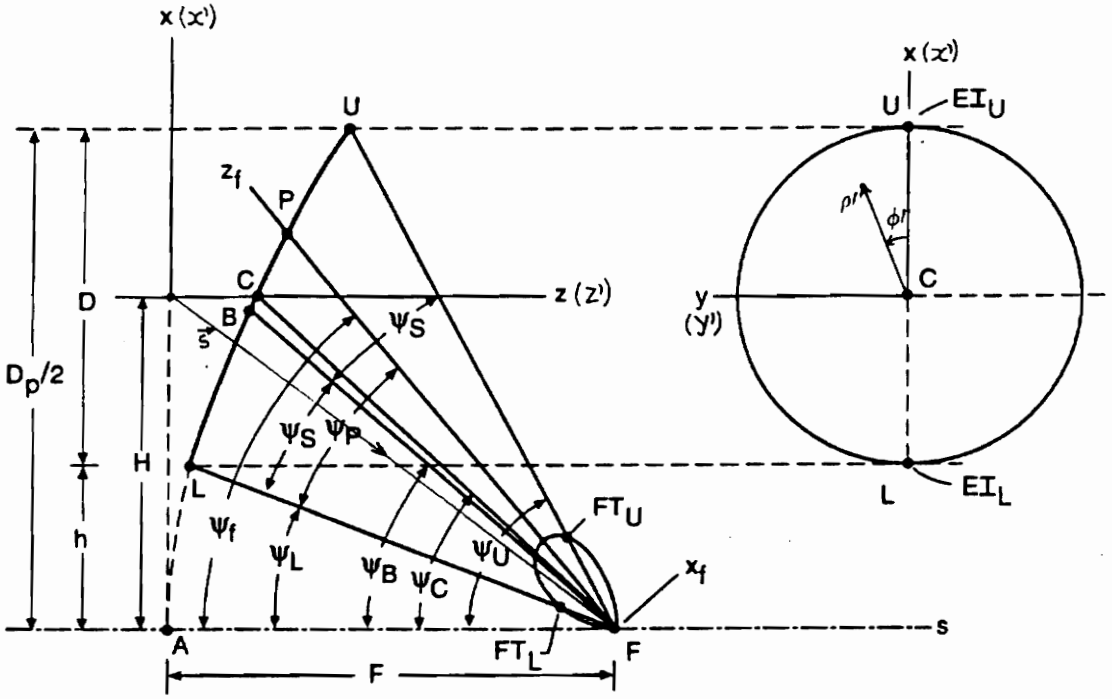

Figure 10.1. Geometry for the offset parabolic reflector. See Table 2.1, Section 2.2, for definitions of parameters.

For a paraboloid, $f(\rho\prime, \phi\prime)$ is given by [13] (see Table 3.1 for definition of symbols)

$$f(\rho\prime, \phi\prime) = z\prime = \frac{\rho\prime^2}{4F} + \frac{H}{2F}\rho\prime\cos\phi\prime + \frac{H^2}{4F} \tag{10.5}$$

The resulting point $(x\prime, y\prime, z\prime)$ can now be expressed in the feed coordinate system with the following transformations (3 rotations and 1 translation) [13, 66]:

$$\begin{bmatrix} x_f \\ y_f \\ z_f \end{bmatrix} = \begin{pmatrix} A_{11} & A_{12} & A_{13} \\ A_{21} & A_{22} & A_{23} \\ A_{31} & A_{32} & A_{33} \end{pmatrix} \begin{bmatrix} x' - s_1 \\ y\prime - s_2 \\ z\prime - s_3 \end{bmatrix} \tag{10.6}$$

where (s_1, s_2, s_3) are the feed rectangular coordinates in the primed coordinate system and

$$\begin{aligned}
A_{11} &= \cos\gamma\cos\alpha - \sin\gamma\cos\beta\sin\alpha \\
A_{12} &= \cos\gamma\sin\alpha + \sin\gamma\cos\beta\cos\alpha \\
A_{13} &= \sin\gamma\sin\beta \\
A_{21} &= -\sin\gamma\cos\alpha - \cos\gamma\cos\beta\sin\alpha \\
A_{22} &= -\sin\gamma\sin\alpha + \cos\gamma\cos\beta\cos\alpha \\
A_{23} &= \cos\gamma\sin\beta \\
A_{31} &= \sin\beta\sin\alpha \\
A_{32} &= -\sin\beta\cos\alpha \\
A_{33} &= \cos\beta
\end{aligned} \tag{10.7}$$

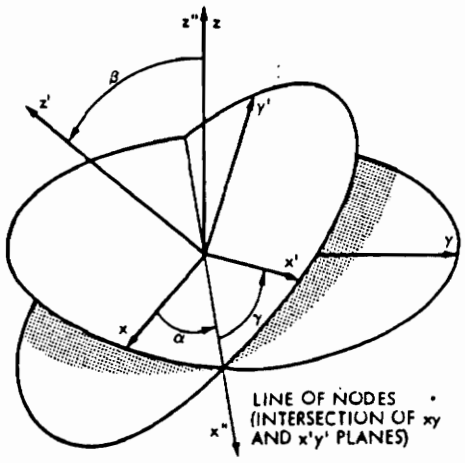

Figure 10.2. Eulerian angles.

The angles $\alpha, \beta,$ and γ are the Eulerian angles defined in Fig. 10.2 [67, 47]. For our study configuration they are given by

$$\begin{aligned} \alpha &= \frac{\pi}{2} \\ \beta &= \pi - \psi_f \\ \gamma &= -\frac{\pi}{2} \end{aligned} \tag{10.8}$$

where ψ_f is the feed tilt angle; see Fig. 10.1.

We now have each aperture sampling point of the form $(\rho\prime, \phi\prime)$ corresponding to a point $(x\prime, y\prime, z\prime)$ on the surface of the reflector and expressed in the feed rectangular coordinate system as (x_f, y_f, z_f). However, the feed pattern is normally

expressed in the feed spherical coordinates (r_f, θ_f, ϕ_f); therefore the following cartesian to spherical transformations are required

$$\begin{aligned} r_f &= \sqrt{x_f^2 + y_f^2 + z_f^2} \\ \theta_f &= \tan^{-1}\left(\frac{\sqrt{x_f^2 + y_f^2}}{z_f}\right) \\ \phi_f &= \tan^{-1}\left(\frac{y_f}{x_f}\right) \end{aligned} \tag{10.9}$$

Once the spherical coordinates are known, the incident field at the reflector surface can be easily computed. Using a $\cos^q(\theta_f)$ model for the feed [13], the feed magnetic field is given by

$$\vec{H}_f(\vec{r}_f) = \frac{1}{\eta_0}\left[-V(\theta_f, \phi_f)\hat{\theta}_f + U(\theta_f, \phi_f)\hat{\phi}_f\right]\frac{e^{-\jmath k r_f}}{4\pi r_f} \tag{10.10}$$

where η_0 is the medium intrinsic impedance, $\frac{e^{-\jmath k r_f}}{4\pi r_f}$ is the propagation factor, and $k = \frac{2\pi}{\lambda}$ is the wave number. For a x_f-polarization, $\mathrm{U}(\theta_f, \phi_f)$ and $\mathrm{V}(\theta_f, \phi_f)$ are given by

$$U(\theta_f, \phi_f) = \cos\phi_f \cos^q(\theta_f) \tag{10.11}$$

$$V(\theta_f, \phi_f) = -\sin\phi_f \cos^q(\theta_f) \tag{10.12}$$

which corresponds to the feed model (2.9) given in Section 2.2.2.

Equation (10.10) yields the spherical components of $\vec{H}_f(\vec{r}_f)$ in the feed local coordinate system. It is necessary to transform that to the antenna primed rectangular system to determine the radiated fields. Thus, another set of rotations and a spherical to cartesian transformation are needed [13]:

$$\begin{bmatrix} H_x(\vec{r}\prime) \\ H_y(\vec{r}\prime) \\ H_z(\vec{r}\prime) \end{bmatrix} = \begin{pmatrix} A_{11} & A_{21} & A_{31} \\ A_{12} & A_{22} & A_{32} \\ A_{13} & A_{23} & A_{33} \end{pmatrix}$$

$$\begin{pmatrix} \sin\theta_f \cos\phi_f & \cos\theta_f \cos\phi_f & -\sin\phi_f \\ \sin\theta_f \sin\phi_f & \cos\theta_f \sin\phi_f & \cos\phi_f \\ \cos\theta_f & -\sin\theta_f & 0 \end{pmatrix} \begin{bmatrix} 0 \\ -V(\theta_f, \phi_f) \\ U(\theta_f, \phi_f) \end{bmatrix} \quad (10.13)$$

This completes the determination of $H_{x,y,z}(\vec{r}\prime)$. The remaining term in (10.1), the unit vector $\hat{n}$, is computed from

$$\hat{n} = \frac{\vec{N}}{|\vec{N}|} \quad (10.14)$$

For a paraboloid reflector, $\vec{N}$ is given by

$$\vec{N} = -\frac{(\rho\prime \cos\phi\prime)}{2F}\hat{x}\prime - \frac{\rho\prime \sin\phi\prime}{2F}\hat{y}\prime + \hat{z}\prime \quad (10.15)$$

Equation (10.1) can now be computed yielding the P.O. surface current components $J_x, J_y,$ and J_z, for each one of the aperture sampling points $(\rho\prime, \phi\prime)$. The surface current components can then be integrated directly on the surface requiring a complicated and time consuming effort. In order to simplify the integration process, a Jacobian transformation [13] is employed. The mapping allows the integration process to be performed over the aperture plane instead of the curved surface and is accomplished with [13]

$$\vec{\tilde{J}} = \vec{J} J_\Sigma = \vec{J} |\vec{N}| \tag{10.16}$$

where J_Σ is the Jacobian transformation; $J_\Sigma = |\vec{N}|$ [13]. From (10.1), (10.14), and (10.16), we obtain

$$\vec{\tilde{J}} = 2\vec{N} \times \vec{H}_f(\vec{r}\prime) \tag{10.17}$$

where $\vec{H}_f(\vec{r}\prime) = H_x(\vec{r}\prime)\,\hat{x} + H_y(\vec{r}\prime)\,\hat{y} + H_z(\vec{r}\prime)\,\hat{z}$, and $\vec{N}$ is given by (10.15).

Finally, we are able to compute the kernel of the radiation integral given below [14]

$$\vec{E}(\vec{r}) = -\jmath \frac{\eta_0}{2\lambda} \frac{e^{-\jmath kr}}{r} (\vec{\tilde{I}} - \hat{r}\hat{r}) \bullet \int_0^{D/2} \int_0^{2\pi} \vec{\tilde{J}}(\vec{r}\prime) e^{\jmath k \hat{r} \bullet \vec{r}\prime} \rho\prime \, d\rho\prime \, d\phi\prime \tag{10.18}$$

where $\hat{r}\hat{r} \bullet \vec{a}$ is shorthand for $\hat{r}(\hat{r} \bullet \vec{a})$, and $(\vec{\tilde{I}} - \hat{r}\hat{r})$ is included to remove the radial component (far-field approximation). The vector $\hat{r}$ is given by

$$\hat{r} = \sin\theta \cos\phi \hat{x} + \sin\theta \sin\phi \hat{y} + \cos\theta \hat{z} \tag{10.19}$$

and $\vec{r}\prime = x\prime\hat{x} + y\prime\hat{y} + z\prime\hat{z}$ is determined from (10.2), (10.3), and (10.4). the quantity $\vec{\vec{I}}$ is referred to as the unit dyad, and is equal to the identity matrix for our purposes.

An evaluation of the total feed power is necessary to determine gain accurately; see Section 11.2.2. Now, our concern is to correctly evaluate (10.18). In order to accomplish that, we use the Jacobi-Bessel series expansion method. However, any other technique can be used since we have only performed general derivations up to this point. The advantage of using the Jacobi-Bessel method is that numerical integration is needed only for evaluating the aperture expansion coefficients, as already commented in Section 10.1. All integrals that are functions of the far-field coordinates are evaluated in closed form, as shown in the next section.

10.4 The Jacobi-Bessel Method

The procedure presented here is similar to the one explained in [13]. However, alterations have been performed to allow the use of special recurrence relations presented by the modified Jacobi polynomials [14]. For the specific case of offset and axisymmetric paraboloids, it will be shown that the higher order coefficients of the series expansion can be computed from the zero order coefficients by using an algebraic recursion relation.

We start by rewriting (10.18) in a form more suitable for the series expansion technique. As in (10.18), the integration is performed with respect to an origin located at the center of the circular projected aperture of the reflector. Using

$$\hat{r} = u\hat{x} + v\hat{y} + w\hat{z} \tag{10.20}$$

with $\vec{r}\prime$ determined from (10.2), (10.3), and (10.4), it is possible to express (10.18) as [14]

$$\vec{E}(\vec{r}) = -\jmath\frac{\eta_0 D^2}{8\lambda}\frac{e^{-\jmath kR}}{R}e^{\jmath kHu}e^{\jmath k\left(\frac{H^2-4F^2}{4F}\right)-w}e^{\jmath k(D^2/16F)w}$$

$$\int_0^1\int_0^{2\pi}\vec{\bar{J}}(s,\phi\prime)e^{\jmath k(D^2/16F)(s^2-1)}e^{\jmath k(D/2)s\left(\frac{H}{2F}\cos\phi\prime\right)}$$

$$e^{\jmath k(D^2/16F)(s^2-1)(w-1)}e^{\jmath k(D/2)s\left\{\left[u-\frac{H}{2F}(w-1)\right]\cos\phi\prime+v\sin\phi\prime\right\}}s\,ds\,d\phi\prime \tag{10.21}$$

where the change of variables $r\prime = (D/2)\,s$, with $0 \leq s \leq 1$, was employed. The integral in (10.21) can now be rewritten as

$$\vec{I} = \int_0^1\int_0^{2\pi}\vec{f}(s,\phi\prime)e^{\jmath k(D^2/16F)(s^2-1)(w-1)}e^{\jmath k(D/2)s(\bar{u}\cos\phi\prime+\bar{v}\sin\phi\prime)}s\,ds\,d\phi\prime \tag{10.22}$$

where $\bar{u} = u - \frac{H}{2F}(w-1)$, $\bar{v} = v$, and the aperture distribution $\vec{f}(s,\phi\prime)$ is given by

$$\vec{f}(s,\phi\prime) = \vec{\bar{J}}e^{\jmath k(D^2/16F)(s^2-1)}e^{\jmath k(D/2)s\left(\frac{H}{2F}\cos\phi\prime\right)} \tag{10.23}$$

It is worth noting that the right hand side of (10.22) is a highly factored form of the original radiation integral (10.18), and (10.23) depends solely on the source

coordinates (s,$\phi\prime$). The second exponential of (10.22) is a Fourier kernel involving the far-field coordinates $(\bar{u}, \bar{v})$; where $\bar{u} = u - \frac{H}{2F}(w-1)$ and $\bar{v} = v$. We will now expand the first exponential of (10.22) into a Taylor series in the complex variable

$$z = \jmath k \frac{D^2}{16F}(s^2-1)(w-1) \tag{10.24}$$

yielding

$$\vec{I} = \sum_{p=0}^{P} \frac{1}{p!}\left(\jmath k \frac{D^2}{16F}\right)^p (w-1)^p \int_0^1 \int_0^{2\pi} (s^2-1)\vec{f}(s,\phi\prime) e^{\jmath k(D/2)s\sin\theta\cos(\phi\prime-\phi)} s\, ds\, d\phi\prime \tag{10.25}$$

We now expand each component of $\vec{f}$ in terms of the modified Jacobi polynomials $F_m^n(s)$, which form a complete set of orthogonal functions defined on the unit disk [14]. A Fourier series is used in the circumferential direction. Thus,

$$f_c(s,\phi\prime) = \sum_{m=0}^{M}\sum_{n=0}^{N} \left[C_m^n \cos(n\phi\prime) + D_m^n \sin(n\phi\prime)\right] F_m^n(s) \tag{10.26}$$

where the subscript c represents the x, y, and z components and

$$\left\{ \begin{array}{c} C_m^n \\ D_m^n \end{array} \right\} = \frac{\epsilon_n}{2\pi} \int_0^1 s\, ds \int_0^{2\pi} d\phi\prime f_c(s,\phi\prime) \left\{ \begin{array}{c} \cos(n\phi\prime) \\ \sin(n\phi\prime) \end{array} \right\} F_m^n(s) \tag{10.27}$$

The Neumann number ϵ_n is defined as [14]

$$\epsilon_n = \left\{ \begin{array}{l} 1;\ \text{if n} = 0 \\ 2;\ \text{if n} \neq 0 \end{array} \right\} \tag{10.28}$$

and the modified Jacobi polynomials are given by

$$F_m^n(s) = \sqrt{2(n+2m+1)}P_m^{(n,0)}(1-2s^2)s^n \tag{10.29}$$

where the Jacobi polynomials $P_m^{(n,0)}(x)$ are computed from

$$P_m^{(n,0)}(x) = \frac{1}{m!}\sum_{i=0}^{m}\frac{m!}{i!(m-1)!}\frac{(n+m+i)!}{2^i(n+i)!}(x-1)^i \tag{10.30}$$

Using the orthogonal expansion (10.26), the integral in (10.25) becomes

$$I_u = \sum_{p=0}^{P}\frac{1}{p!}\left(\jmath k\frac{D^2}{16F}\right)^p(w-1)^p\sum_{m=0}^{M}\sum_{n=0}^{N}\left[C_m^n I_{m,cos}^{p,n} + D_m^n I_{m,sin}^{p,n}\right] \tag{10.31}$$

where [14, 61]

$$I_{m,\sin or\ \cos}^{p=0,n} = 2\pi\jmath^n\left\{\begin{array}{c}\cos(n\phi)\\ \sin(n\phi)\end{array}\right\}\sqrt{2(n+2m+1)}\frac{J_{n+2m+1}[k(D/2)\sin\theta]}{[k(D/2)\sin\theta]} \tag{10.32}$$

and

$$I_{m=0,\sin or\ \cos}^{p,n} = 2\pi\jmath^n\left\{\begin{array}{c}\cos(n\phi)\\ \sin(n\phi)\end{array}\right\}\sqrt{2(n+1)}(-2)^p p!\frac{J_{n+p+1}[k(D/2)\sin\theta]}{[k(D/2)\sin\theta]^{p+1}} \tag{10.33}$$

It is worth noting the following properties of the Bessel functions of first kind and integer order:

$$\frac{J_k(0)}{0^l} = \left\{\begin{array}{c}\frac{1}{2^k k!};\ \text{if } k=l\\ 0;\ \text{if } k>l\end{array}\right\} \tag{10.34}$$

which reduces to

$$\frac{J_k(0)}{0} = \left\{ \begin{array}{c} 1/2;\ \text{if } k = 1 \\ 0;\ \text{if } k > 1 \end{array} \right\} \text{ for } l = 1. \tag{10.35}$$

The coefficients for $p \neq 0$ and $m \neq 0$ can be computed from (10.32), (10.33), and the following recursion relation valid only for paraboloids [14]

$$I^{p,n}_{m,\sin or \cos} = a_{mn} I^{p-1,n}_{m-1,\sin or \cos} + b_{mn} I^{p-1,n}_{m,\sin or \cos} + c_{mn} I^{p-1,n}_{m+1,\sin or \cos} \tag{10.36}$$

where

$$a_{mn} = -\frac{d_m}{d_{m-1}} \left[\frac{m(m+n)}{(n+2m)(n+2m+1)} \right]$$

$$b_{mn} = \frac{n^2 - (n+2m)(n+2m+2)}{2(n+2m)(n+2m+2)} \tag{10.37}$$

$$c_{mn} = -\frac{d_m}{d_{m+1}} \left[\frac{(m+1)(n+m+1)}{(n+2m+1)(n+2m+2)} \right]$$

$$d_m = \sqrt{2(n+2m+1)}$$

Finally, the expression for the electric field (10.21) is given in component form by

$$E_c(\vec{r}) = -\jmath\frac{\eta_0 D^2}{4\lambda}\frac{e^{-\jmath kR}}{4\pi R}e^{\jmath kHu}e^{\jmath k\left(\frac{H^2-4F^2}{4F}\right)w}2\pi e^{\jmath k(D^2/16F)w}$$

$$\sum_{p=0}^{P}\frac{1}{p!}\left(\jmath k\frac{D^2}{16F}\right)^p(w-1)^p\sum_{m=0}^{M}\sum_{n=0}^{N}\left[C_m^n I_{m,cos}^{p,n} + D_m^n I_{m,sin}^{p,n}\right] \quad (10.38)$$

This completes the analysis of the Jacobi-Bessel method. We can now summarize how (10.38) is evaluated. Numerical integration is necessary only for computing the coefficients C and D, which are functions exclusively of the aperture primed coordinates. Once that is performed for all the necessary aperture sampling points determined accordingly to the chosen integration algorithm, each point of the far-field pattern can be determined. Note that the I coefficients are functions exclusively of the far-field coordinates (θ, ϕ) and are determined directly from (10.32), (10.33), and (10.36). Thus, once the coefficients C and D have been determined, the far-field patterns can be computed at any observation angle without performing numerical integrations. This is in contrast to the direct evaluation of the original radiation integral (10.18), which has to be computed repeatedly for each observation point.

Chapter 11

Appendix B: The Parabolic Reflector Analysis Code (PRAC)

11.1 Preliminary Considerations

The Jacobi-Bessel series expansion method was described in detail in the last chapter. Alterations to the basic method were performed in order to use the special algebraic recursion relations (10.36) and (10.37) available for parabolic reflector surfaces. Here, the technique is combined with the Gaussian-Zernike integration scheme [64, 68] to assure a high efficient and accurate numerical implementation.

The user friendly code PRAC, Parabolic Reflector Analysis Code, was developed and allows the user to evaluate the co- and cross-polarized radiation patterns of axisymmetric and offset parabolic reflectors. The effectiveness of PRAC was confirmed by extensive comparisons with measured data and results obtained from canonical models and with the code GRASP7. PRAC permits the analysis of parabolic reflector antennas with any circular projected diameter, any focal length,

and any offset distance. The user can specify the reflector geometry in centimeters, meters, inches or feet. The linearly polarized feed can be pointed in any direction. Small feed displacements from the focal point are also allowed. PRAC offers a complete integrated environment with menus of options, data input fields, and an on-line help system available at each step of the program. In addition, a comprehensive user's manual is included.

11.2 Numerical Implementation

11.2.1 The Numerical Integration

The double integral in (10.27) has to be numerically evaluated by using a suitable integration routine. In order to compare the efficiency and accuracy of different routines, one needs a figure of merit. The results and conclusions presented in this section are based on the work performed in [64].

Pattern accuracy breakdown is caused by phase errors introduced by the discrete sampling of the aperture distribution used in the numerical integration. A figure of merit, the p-factor, was introduced in [64] for measuring the accuracy of several numerical integration schemes used in the evaluation of radiation integrals. The p-factor is proportional to the distance in degrees between boresight and the point of breakdown. Thus, the larger is p, the larger is the region where the pattern is accurately computed; for further details see [64].

Figure 11.1 [64] shows the p-factor behavior of three integration schemes often employed in the evaluation of radiation integrals. We see, from Fig. 11.1, that the Gauss-Zernike method (solid line) yields the best performance according to this particular study. Also, the optimum value for the ratio N_ρ/N_ϕ is 1/4. This corresponds to 32 points in the diameter (16 points in the radius) and 32 points in the half-perimeter (64 points for the full circle). This choice guarantees that the integral (10.27) is evaluated as accurately as possible.

The Gauss-Zernike numerical integration scheme is fully described in the literature [68]. In this approach, the same orthogonal functions used for the aperture distribution expansion (i.e., the Zernike/Jacobi polynomials) are also used for the numerical integration of the aperture expansion coefficients. The Gauss-Zernike method avoids the cluster of sampling points near the end of the integration interval, normally generated by conventional Gaussian integration schemes. In general, the Gauss-Zernike method performs a Gaussian integration across the entire diameter of the reflector, rather than from the center of the dish out to the radius. Also, the Gauss-Zernike method requires a considerable lower number of integration points and is, therefore, more efficient than other methods. The technique consists in approximating the double integral by a weighted double summation [68]

$$\int_0^{2\pi}\int_0^1 g(s,\phi\prime)s\,ds\,d\phi\prime = \sum_{i=1}^{L_1}\sum_{l=1}^{L_2}\frac{\pi w_i}{L_2}g(s_i,\phi_l\prime) \tag{11.1}$$

where $g(s_i,\phi_l\prime)$ is the sampled kernel of (10.27). The parameters $s_i = \rho_i\prime/(D/2)$ and w_i are referred to as the nodal points (i.e., zeros of the Zernike polynomials) and weights, respectively. For $L_1 = L_2 = 32$ (32nd order), the nodal points and weights are given in Table 11.1 [64].

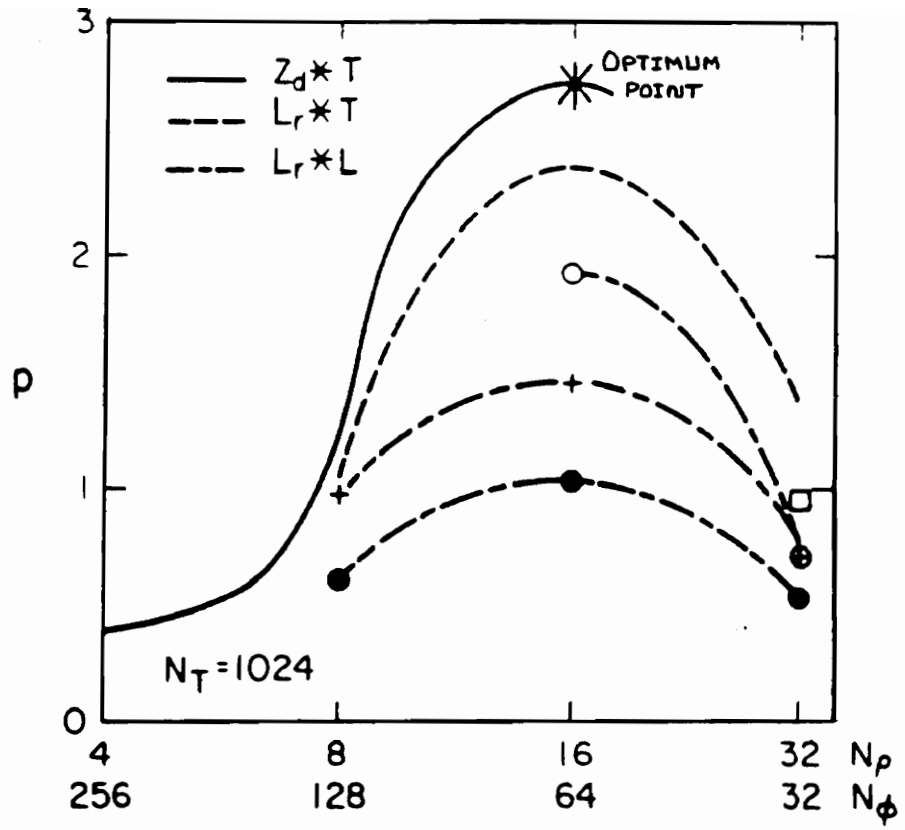

Figure 11.1. p-factor for various integration methods as functions of N_ρ and N_ϕ for fixed total number of integration points. Z_d*T, L_r*T, and L_r*L, represent the Gauss-Zernike, the Gauss-Legendre, and the Composite Gauss-Legendre methods, respectively. From [64].

Table 11.1. **Nodes and Weights for Gauss-Zernike Numerical Integration ($L_1 = L_2 = 32$). From [64].**

Nodes, $\pm s_i$	Weights, w_i
0.0727978880474910	0.0067881148529385
0.1664706834952739	0.0155633809846620
0.2591995347335465	0.0237896279206241
0.3497110175880066	0.0311572428138741
0.4371062545877790	0.0373989972042406
0.5205685460675333	0.0422891298483644
0.5993314815550548	0.0456508537646179
0.6726765521809983	0.0473626526552414
0.7399366601964945	0.0473626521476812
0.8005009384184874	0.0456508857917567
0.8538199186584379	0.0422891196494396
0.8994097969942914	0.0373990250412830
0.9368577436672745	0.0311571808395279
0.9658236528996722	0.0237897186785034
0.9860465143006358	0.0155632597351050
0.9973466740001312	0.0067882162608963

The angular sampling directions, ϕ_l' are given by

$$\phi_l' = l \times \phi_{inc} \tag{11.2}$$

where

$$\phi_{inc} = \frac{\pi}{32} \tag{11.3}$$

Therefore, we can efficiently compute the double integral in (10.27) by using (11.1), (11.2), and (11.3) with the values presented in Table 11.1.

11.2.2 Gain Considerations

The directive gain, D, of the radiated pattern can be calculated from [12]

$$D = \frac{|\vec{E}(\vec{r})|^2}{\frac{1}{4\pi}\int\int |\vec{E}(\vec{r})|^2 \sin\theta \, d\theta \, d\phi} \tag{11.4}$$

where the electric field $\vec{E}(\vec{r})$ is evaluated at the far-field (no radial component). The evaluation can be carried out in terms of co- and cross-polarized components. In the present work an unitary radiation efficiency is assumed [12]; thus, directivity and gain are the same and equal to the maximum value of (11.4). By conservation of energy, the denominator in (11.4) is equal to

$$\frac{1}{4\pi r^2} \times \{\text{Total Power Radiated by the Feed}\} \tag{11.5}$$

For the $\cos^q(\theta_f)$ feed model of (10.11) and (10.12) [14]

$$\{\text{Total Power Radiated by the Feed}\} = \frac{2\pi}{2q+1} \tag{11.6}$$

Finally, using (11.5), (11.6), and (10.38) in (11.4), we obtain

$$D = \frac{\pi^2 \eta_0^2 D^4 (2q+1)}{2\lambda^2} \left| \sum_{p=0}^{P} \frac{1}{p!} \left(\jmath k \frac{D^2}{16F} \right)^p (w-1)^p \sum_{m=0}^{M} \sum_{n=0}^{N} \left[C_m^n I_{m,cos}^{p,n} + D_m^n I_{m,sin}^{p,n} \right] \right|^2 \tag{11.7}$$

where | | denotes the absolute value.

11.3 Numerical Results and Comments

The Parabolic Reflector Analysis Code, PRAC, was implemented based on the material presented in Sections 10.3, 10.4, and 11.2. PRAC offers a complete integrated environment with menus of options, data input fields, and an on-line help system available at each step of the program. It was written in Turbo Pascal 7.0, and requires a hardware compatible with a IBM-PC DOS based computer. A VGA color monitor is recommended. PRAC permits the analysis of parabolic reflector antennas with any circular projected diameter, any focal length, and any offset distance. The user can specify the geometry in centimeters, meters, inches, or feet. The linearly

polarized feed can be pointed in any direction. Small feed displacements from the focal point are also allowed.

The infinite sums in (10.38) and (11.7) were truncated in PRAC with values of P=4 and M=N=7. These values assure a correct convergence of the series for both small and large reflectors [13]. In fact, for parabolic reflectors, it is shown in [13] that P=2 is sufficient for accurate results. However, it was decided to perform the computations up to the 4th order (i.e., P=4) giving the user more reliability. The total processing time is about 1 minute per radiation pattern on a 486 DX2 - 50 MHz system.

As an illustration, we analyze the axisymmetric parabolic reflector specified in Table 11.2. Also in the same table, the results obtained with PRAC are compared with the results obtained from other sources for the same reflector configuration. Note the excellent agreement, indicating the good accuracy of PRAC. Fig. 11.2 shows the radiation pattern computed by PRAC in the yz-plane ($\phi = 90°$). Cross polarization is very low for this configuration due to the fact that the axisymmetric reflector is illuminated by a purely polarized balanced feed; i.e., the primary radiation pattern is symmetric in ϕ_f. An offset paraboloid case example is discussed in section 11.4.3. Other case examples are presented throughout this dissertation.

Table 11.2. **Test Results for an Axisymmetric Reflector**

$\phi = 90°$ (yz-plane)

Diameter $D = D_p = 48\lambda$

(F/D_p) ratio = 1.003

$\cos^q \theta_f$ feed; q=17.0963 (18.5 dB edge taper)

	PRAC	GRASP7 [15]	RAP [66]	Samii [13]
Gain	42.15 dBi	42.12 dBi	NA*	NA*
ϵ_{ap}	72.15%	71.65%	NA*	NA*
HPBW	1.50°	1.52°	1.50°	1.50°
1st Null Position	2.20°	2.22°	2.20°	2.20°
1st SLL Position	2.48°	2.48°	2.40°	2.40°
1st SLL Value	-37.81 dB	-39.54 dB	-37.92 dB	-38.00 dB
2nd Null Position	2.86°	2.82°	2.90°	2.80°
2nd SLL Position	3.40°	3.38°	3.30°	3.40°
2nd SLL Value	-36.19 dB	-35.92 dB	-36.20 dB	-36.00 dB

*Not Available

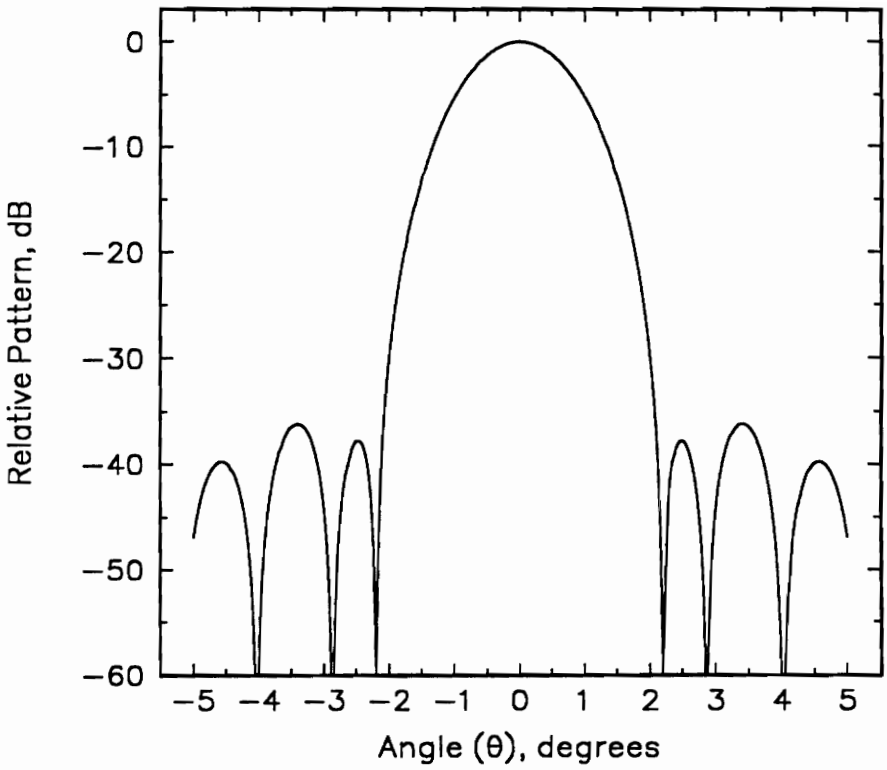

Figure 11.2. Computed co-polarized far-field pattern of the 48 λ axisymmetric paraboloid configuration specified in Table 11.2. The pattern was computed by PRAC in the $\phi = 90°$ plane. Cross polarization is very low due to the fact that the axisymmetric reflector is illuminated by a purely polarized balanced feed; i.e., the primary radiation pattern is symmetric in ϕ_f.

11.4 PRAC User's Manual

11.4.1 Program Overview

The Parabolic Reflector Analysis Code, PRAC, is a user friendly code developed by Marco Terada and Warren Stutzman to analyze axisymmetric and offset parabolic reflector antennas. PRAC evaluates the radiation integral (physical optics surface current integration) with the Jacobi-Bessel series expansion method [13, 14] and yields the co- and cross-polarized radiated fields with high accuracy and efficiency. The effectiveness of PRAC has been confirmed by extensive comparisons with measured data and results obtained from canonical models and with the commercial code GRASP7.

PRAC permits the analysis of parabolic reflector antennas with any circular projected diameter, any focal length, and any offset distance. The user can specify the geometry in centimeters, meters, inches, or feet. The linearly polarized feed can be pointed in any direction. Small feed displacements from the focal point are also allowed.

PRAC offers the user a complete integrated environment with menus of options, data input fields, and a complete on-line help system available at each step of the program. It has been written in Turbo Pascal 7.0, and requires a hardware compatible with a IBM-PC DOS based computer. A VGA color monitor is recommended. Its executable file (version 2.3) has 138 kbytes, after the compilation of more than 5,000 lines of code.

This manual describes all options and commands in order to familiarize the user with the PRAC integrated environment. It also presents a detailed example and some common user errors.

11.4.2 Main Menu: The Commands of PRAC

To start the program type the following from the DOS environment:

PRAC <ENTER>

Once the program is loaded, the user has access to the main menu of PRAC. In order to select any one of the options, the user may either type the first letter of the desired option, or highlight the option (using the arrow keys) and press <ENTER>. Once an option is chosen, a set of sub-options may appear in the form of a vertical menu. The user can press the <ESC> key to go back to a previous menu.

We now present a brief description of the main options and sub-options of PRAC. The key commands are summarized in Table 1.

FILE

This option allows the user to perform manipulations with the data files. The sub-options are:

LOAD

This option loads a previously stored data file from the current drive (i.e., the one from where PRAC was loaded). All input data files used by PRAC have the extension ".INP". The user, however, does not need to type it, since the extension is a default parameter of the system. The file name should have a maximum number of 8 alpha-numerical characters. The user must type the file name followed by <ENTER>.

SAVE

This option stores the reflector system specifications currently available in the memory in the current drive (i.e., the one from where PRAC was loaded). The file name should have a maximum number of 8 alpha-numerical characters, which are arbitrary. After typing the file name, the user should press <ENTER>. The "SAVE" option has effect only if a reflector system has already been completely specified.

EDIT

This option allows the user to input or modify the data that represent the reflector system to be analyzed by PRAC. It presents the sub-options listed bellow:

MODIFY

MODIFY edits the reflector system specifications resident in the computer memory. The user may alter the reflector geometry (sub-option "REFLECTOR"), the feed characteristics (sub-option "FEED"), or the far-field pattern plot specifications (sub-option "PATTERN"). These options are available only after a reflector system has been completely specified through the commands "LOAD" or "NEW" (see section 11.4.2, page 205).

While entering numerical values (edit mode), only the numeric keys, the minus sign (-), and the control keys are active. Pressing of any other key has no effect. It is important to note that the decimal point (.) is already present in the data input field. Thus, it is essential to locate the number correctly in relation to the fixed decimal point. Note that the size of the data input field, and the fixed decimal point, limit the input data to the numerical range allowed by PRAC. An

empty numerical data input field is not considered zero; the user should verify that all fields are filled before pressing Ctrl-End.

NEW

This option deletes the geometry currently in the memory, if there is one, and enters the edit mode in order to allow the user to specify a new reflector antenna. "NEW" has several sub-options, although only the single parabolic geometry is implemented in the present version.

LIST

This option provides the user with a complete list of the specified reflector geometry and feed characteristics. Also, this option shows some additional information, such as the values of the feed pointing angle to the center of the main reflector and to the direction that bisects the main reflector. These values are computed by PRAC based on the data previously entered by the user.

RUN

This option computes the co- and cross-polarized radiated fields generated by the specified reflector configuration. The patterns are stored in a output file ".OUT", and can be viewed with the option "PLOT" or with any graphical package (e.g., AXUM [69]). The file name should have a maximum number of 8 alphanumerical characters, which can be arbitrarily picked by the user. After typing the file name, the user should press <ENTER>. The "RUN" option has an effect only if a reflector system has already been completely specified. The first four lines in the ".OUT" data file are: angle phi (degrees), initial angle theta (degrees), theta

Table 11.3.

Summary of Commands

PRAC <ENTER> To start the code.

<ESC> Return to previous menu.

↓ or <ENTER> Go to the next data input field.

↑ Go back to the previous data input field.

Pg Up Moves the cursor to the first data input field of the current screen.

Pg Dn Moves the cursor to the last data input field of the current screen.

Ins Activate/Deactivate the character insertion mode.

← Delete the previous character.

Del Delete the character above the cursor.

<Tab Key> Switches between available options.

Ctrl-End (both keys should be pressed at the same time). Leaves the current data input screen, and activates the next data input screen, when one is available. Otherwise Ctrl-End finishes the edit mode going back to the main menu.

Ctrl-F1 Calls the help screen (both keys should be pressed at the same time). It is available at any instant in the data edition mode. The help screen contains information sensitive to the actual cursor position and thus varies at each stage of the program. In order to close the help screen, going back to the data edition mode, the user can press any key.

increment (degrees), and number of theta angles. From the left to right, the three columns in the ".OUT" data file are: angle theta (degrees), co-pol. pattern (dBi), and cross-pol. pattern (dBi).

PLOT

This option shows any pattern plot previously computed by "RUN" and stored in a ".OUT" output file. After typing the filename, the user should press <ENTER>.

11.4.3 Using PRAC

Once in the PRAC environment, load the file "OFFSET.INP" (provided with the disk) by choosing the option "FILE", followed by "LOAD"; then type: OFFSET <ENTER>. PRAC will automatically enter the edit mode. This is done in order to inform the user about the content of the file and also to allow the user to perform modifications, if necessary. It is always possible to modify a file later on by choosing the options "EDIT" and "MODIFY".

The first screen to appear is the reflector geometry screen. The user can navigate among the data input fields by using the control keys (see section 11.4.2). It is also interesting to call the help screen from different fields (by pressing Ctrl-F1), since the PRAC help system is case sensitive. The geometry used by PRAC is shown in Figure 11.3 and the symbols are defined in Table 11.4. Further information may be found in the PRAC help screens (Ctrl-F1).

Once the user is done with the first screen, use Ctrl-End to bring the second screen. In this particular example, the second screen is the feed data screen. The $cos^q(\theta_f)$ feed screen appears after pressing Ctrl-End one more time. A summary of all the parameters specified by the user can be obtained through the "LIST" command.

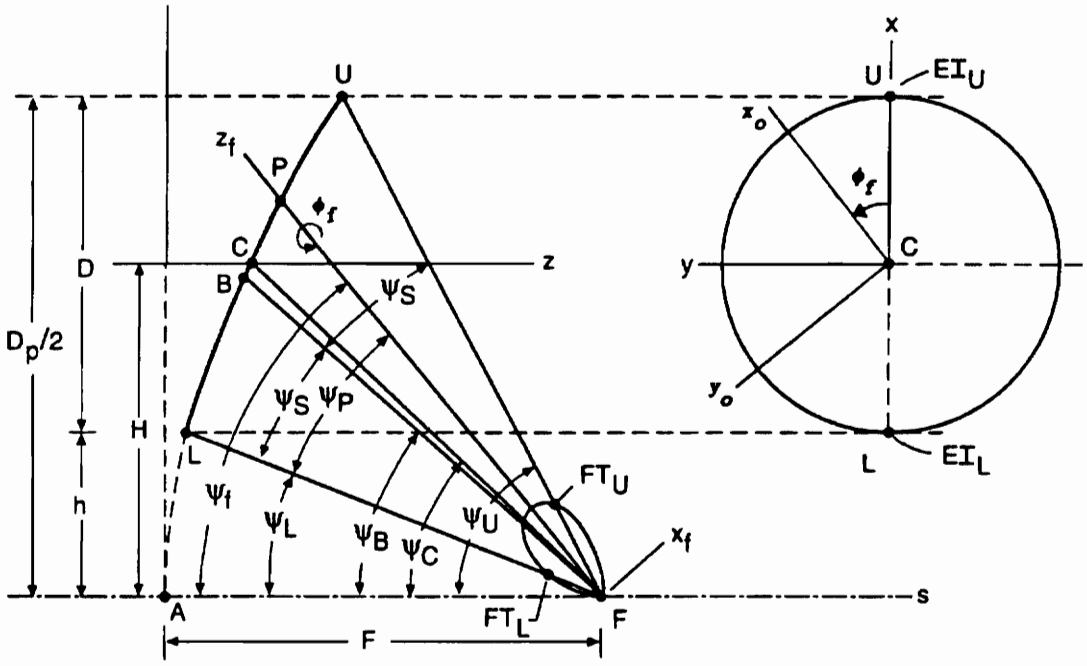

Figure 11.3. Geometry of the offset parabolic reflector. See Table 11.4 for definitions of parameters.

Table 11.4.

Definitions of Parameters

D = Diameter of the projected circular aperture of the parabolic main reflector.

h = Offset distance = Distance from the axis of symmetry (s) to the lower reflector edge.

D_p = Diameter of the projected circular aperture of the parent paraboloid.

H = Offset of reflector center = Distance from axis of symmetry to center of reflector $= D/2 + h$.

F = Focal length.

F/D_p = "F/D" of parent paraboloid.

ψ_f = Angle of feed antenna pattern peak relative to reflector axis of symmetry (s); the feed is directed toward point P.

ψ_B = Value of ψ_f which bisects the reflector subtended angle; i.e. feed is aimed at point B ($\psi_f = \psi_B$) and $\psi_B = \psi_S + \psi_L$.

ψ_C = Value of ψ_f when the feed is aimed at the reflector point C corresponding to the aperture center.

ψ_S = Half of the angle subtended by the reflector as viewed from the focal point.

Point A = Apex of parent reflector.

Point B = Point on main reflector which bisects subtended angle viewed from focal point.

Point C = Point on main reflector which projects to the center of the projected aperture.

Point F = Focal point.

FT = Feed edge taper; FT ≥ 0.

Also, "LIST" shows additional information for the given geometry and feed taper specifications (e.g., the value of "q").

Finally, after pressing Ctrl-End one more time, the far-field pattern screen appears. This is the last screen for data input. The current version of PRAC allows only the evaluation of standard theta-cut patterns (i.e., phi is fixed while theta varies). These are, most of the time, the patterns of interest. In this specific example, the pattern is computed in the yz-plane (i.e., the plane normal to the offset plane); see Figure 11.3. Valuable information about typical range values is provided in the help screen.

The dimensions of the offset reflector in consideration are summarized in Table 11.5; see Fig. 11.3 and Table 11.4 for definition of symbols. Table 11.5 also presents the results computed by PRAC and obtained from other sources, showing its excellent accuracy. The largest difference of 0.70 dB occurs between PRAC and results published in [13] on the side lobe level value (SLL). However, the values listed in the last column of Table 11.5 were read directly from graphs presented in [13] and thus are not very accurate.

Figure 11.4 shows the radiation pattern computed by PRAC in the yz-plane (plane normal to the offset plane). Cross Polarization (XPOL) is expected to be maximum at this plane [17, 4]. PRAC computed a maximum XPOL of -28.05 dB, as shown in Fig. 11.4 or read from Table 11.5. Fig. 11.5 shows the radiation pattern computed by the commercial code GRASP7 [15] in the same $yz-$plane.

Table 11.5. **Test Results for an Offset Reflector**

$\phi = 90°$ (normal to the offset plane)

Diameter $D = 100\lambda$

Offset of reflector center $H = 70\lambda$

(F/D_p) ratio = 0.466

$\cos^q \theta_f$ feed; q=13.0897 (10 dB edge taper)

Feed tilt angle $\psi_f = 34.72° \approx \psi_C$

	PRAC	GRASP7 [15]	RAP [66]	Samii [13]
Gain	49.01 dBi	48.98 dBi	NA*	NA*
ϵ_{ap}	80.67%	80.11%	NA*	NA*
HPBW	0.64°	0.62°	0.50°	0.60°
SLL Position	1.04°	1.04°	1.00°	1.00°
SLL Value	-24.30 dB	-24.41 dB	-24.09 dB	-25.00 dB
XPOL Position	0.44°	0.44°	0.40°	0.40°
XPOL Value	-28.05 dB	-28.05 dB	-28.40 dB	-30.00 dB

*Not Available

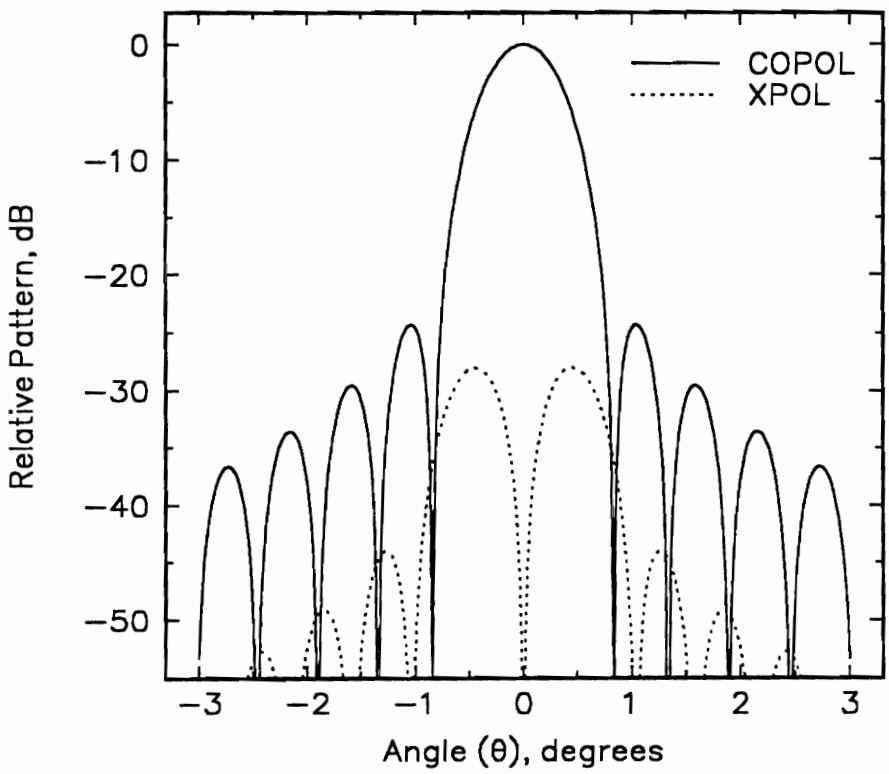

Figure 11.4. The yz-plane co- and cross-polarized radiation patterns computed by PRAC for the 100λ offset parabolic reflector specified in Table 11.5.

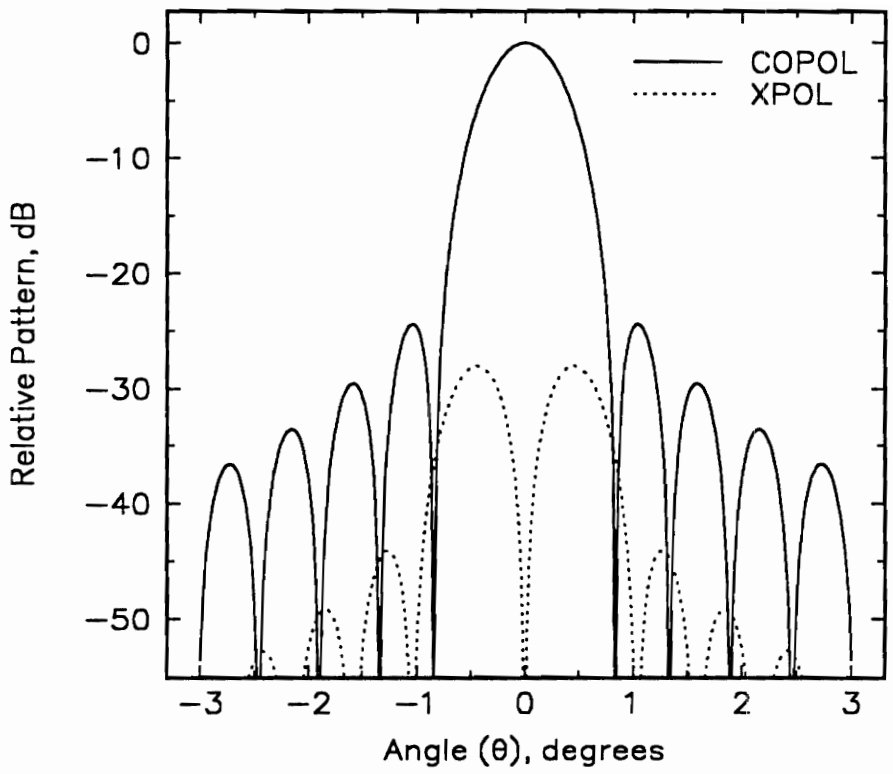

Figure 11.5. The yz-plane co- and cross-polarized radiation patterns computed by GRASP7 for the 100λ offset parabolic reflector specified in Table 11.5.

A comparison between Figs.11.4 and 11.5 shows that the radiation patterns computed by both codes are in very good agreement. The largest difference of 0.11 dB occurs on the sidelobe level (SLL). However, both PRAC and GRASP7 computed the exact same location for the SLL; i.e., at 1.04° off boresight.

As a final note we mention that experimental data were available for the case of $D = 85.5\lambda, H = D/2$ (just fully offset), $F/D_p = 0.3$, and $\psi_f \approx \psi_C$ (FT=10 dB for $\psi_f = \psi_B$) [4]. Measured and computed values (PRAC and GRASP7) of XPOL are -22, -21.9, and -21.7 dB, respectively, confirming the accuracy of the computer simulations.

11.4.4 Summary of Common User's Errors

- No numerical data input field may be left blank. In order to set some variable to zero, just type: 0 <ENTER>.
- The decimal point is already fixed in the numerical data input fields of PRAC: .__025 ≠ 0.25___
- The initial theta angle in the sub-option "PATTERN" must be different than zero.
- Finally, we note that the following options, although present in the PRAC menus, are not yet in operation:

  1. SPHERICAL REFLECTORS
  2. DUAL REFLECTORS

Chapter 12

Appendix C: Derivation of Mizugutch and Dragone Conditions for XPOL Minimization

12.1 Preliminary Considerations

In this appendix we derive and contrast design relations often employed to minimize XPOL in dual offset reflector antennas. Initially, in the next section, we investigate the conditions for XPOL reduction in single offset reflectors, and then we extend the main results to dual configurations through the equivalent paraboloid concept. In subsequent sections, we derive Mizugutch and Dragone equations from these conditions, and a study is performed to compare and contrast the relations. As we will see, both equations represent the same condition and therefore yield identical results.

12.2 Cross Polarization in Single Parabolic Reflectors

We have shown in Chapter 2 that XPOL in single parabolic reflector systems is minimized when the feed antenna axis is coincident with the paraboloid axis of symmetry s [4]; see Fig. 2.1. It is assumed that the feed antenna is free of XPOL and is located at the paraboloid focal point F. In addition, the feed radiation pattern is assumed to be symmetric (i.e., "balanced") with respect to the z_f-axis. Figure 2.9 in Section 2.3.3 shows a typical XPOL behavior of an offset parabolic reflector antenna as a function of feed pointing angle, ψ_f [4]. Note that XPOL decreases with decreasing feed angle, ψ_f, and is expected to be very low (i.e., XPOL < -35 dB) for $\psi_f = 0°$ [3, 4]. This corresponds to a geometry in which the feed axis, z_f, is coincident with the main reflector axis, s. In practice, this is only possible with axisymmetric main reflectors, $H = 0$ in Fig. 2.1, since the feed must be tilted in single offset configurations in order to reduce gain loss. These results can be extended to dual offset geometries through the application of the equivalent paraboloid concept; this is addressed in the next section.

12.3 The Equivalent Paraboloid Concept

In this section we comment on the fact that a dual reflector system employing a parabolic main reflector and an ellipsoidal or hyperboloidal subreflector is equivalent to a single parabolic reflector system. XPOL of the original dual reflector configuration is minimized when the feed antenna axis is oriented according to the

equivalent paraboloid axis, as commented in the last section. Furthermore, if the main reflector presents a circular projected aperture, the equivalent paraboloid is axisymmetric and gain loss is not excessive. Conditions to reduce gain loss while minimizing XPOL can be found elsewhere [31] and are not treated in the present study.

It can be shown that any sequence of confocal reflectors formed by ellipsoids, hyperboloids, and paraboloids, is equivalent to a single reflector which is either an ellipsoid, a hyperboloid, or a paraboloid [34]. In particular, when the sequence is formed by an ellipsoidal subreflector and a parabolic main reflector (referred to as Gregorian configuration), or a hyperboloidal subreflector and a parabolic main reflector (referred to as Cassegrain configuration), the equivalent single reflector is a paraboloid. The proof, based on a conformal mapping argument, is somewhat lengthy and is herein omitted. Figs. 12.1 and 12.2 show the equivalent paraboloid concept applied to Gregorian and Cassegrain dual offset reflector antennas [31]. The equivalent paraboloid in each case, neglecting diffraction and defocusing effects, produces the same aperture fields of the corresponding dual reflector system, and consequently the near-boresight radiated fields are also identical. Therefore, for the purpose of determining the properties of the radiated fields, one may replace the original dual reflector Gregorian or Cassegrain configuration by its corresponding equivalent parabolic system.

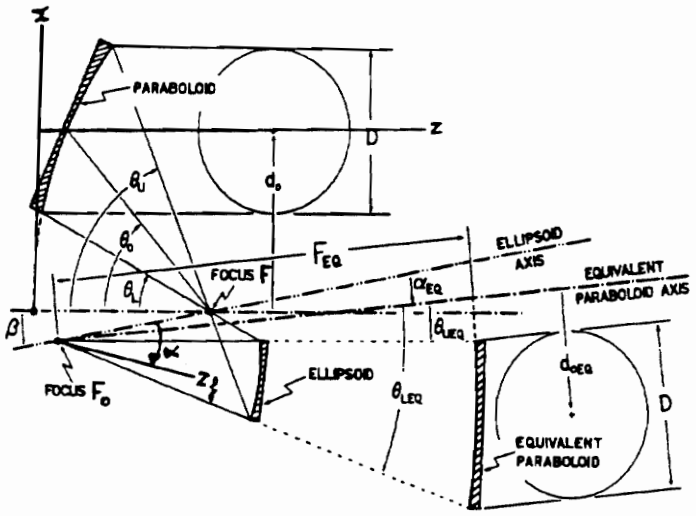

Figure 12.1. Equivalent paraboloid for the dual offset Gregorian configuration. From [31].

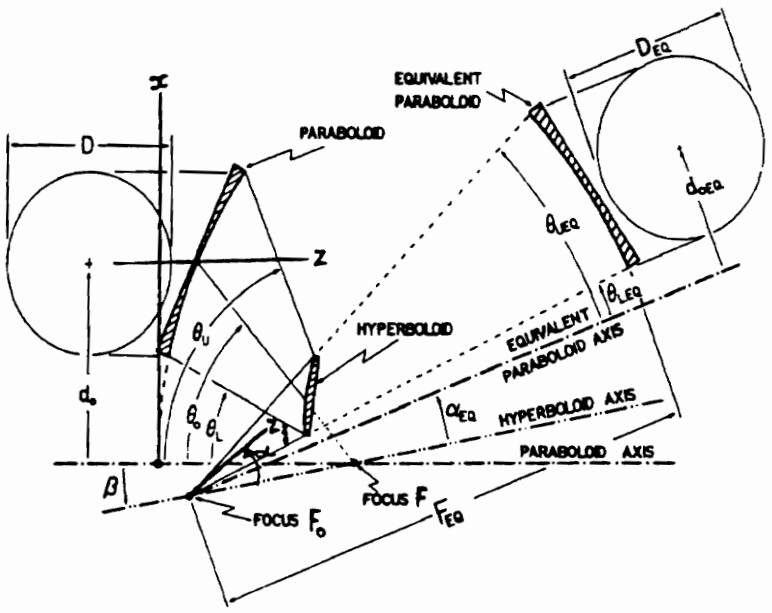

Figure 12.2. Equivalent paraboloid for the dual offset Cassegrain configuration. From [31].

12.4 The Equivalent Paraboloid Axis of Symmetry

Our goal in the present section is to determine the condition for which the feed axis of the original dual reflector system is coincident with the equivalent paraboloid axis. As commented in the last section, XPOL is minimized when this condition is satisfied, and XPOL levels of -35 dB or better are expected. We start by showing how one can determine the axis of symmetry of an ellipsoid. Then we extend the result to a paraboloid since it can be seen as an ellipsoid with one focus at infinity [31].

It is known that any ray coming from one of the focal points of an ellipsoid is reflected towards the other focal point. Suppose that the ellipsoidal surface $\sum_1$ and one of its foci, F_0, are given and it is desired to find the exact location of the axis of symmetry (defined by the two foci). Let a ray from the focal point F_0 be reflected twice by the surface $\sum_1$; see Fig. 12.3 (a) [34]. In addition, let $\vec{s}$ and $\vec{s}''$ be the initial and final directions of the ray. It is easy to see from Fig. 12.3 that both rays coincide with the axis only when

$$\vec{s} = \vec{s}'' \tag{12.1}$$

Thus, the axis can be found by searching for a ray that satisfies this condition. Note from Figs. 12.3 (b) and 12.3 (c) that there are two such rays, with opposite directions. This result is also valid for paraboloids, since they can be seen as ellipsoids with a focal point at infinity. In that case, the second reflection is assumed to occur at infinity and $\vec{s}''$ is always parallel to the axis of symmetry.

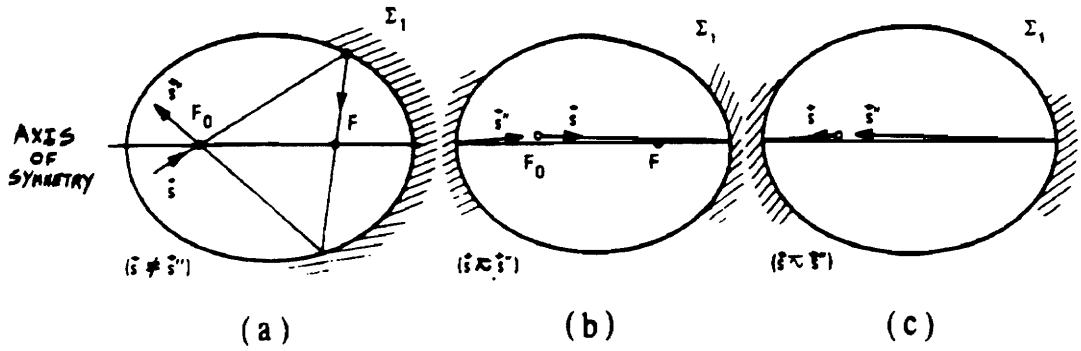

Figure 12.3. The axis of $\sum_1$ is determined by varying $\vec{s}$ until $\vec{s} = \vec{s}''$. From [34].

The feed antenna is located at the ellipsoid focal point F_0 which is coincident with the focal point of the equivalent paraboloid; see Figs 12.1 and 12.2. Therefore, if the direction of the feed antenna axis is given by $\vec{s}$, condition (12.1) assures that the feed axis is coincident with the equivalent paraboloid axis, thus minimizing XPOL.

Notice that two reflections on the equivalent paraboloid imply a total of four reflections in the original configuration [34]. This is easy to see from the fact that the ray returns to F_0 after two reflections on the equivalent paraboloid. Since the focal point F_0 of the equivalent paraboloid is coincident with the focal point of the subreflector in the original system, we conclude that the actual ray must also return to F_0 in the original system; see Figs. 12.4 and 12.5. In order for this to be possible four reflections are required. The first two reflections take place at the actual subreflector (ellipsoid or hyperboloid) and the parabolic main reflector, while the last two occur at infinity (regarding the paraboloid as the limiting case of an ellipsoid with

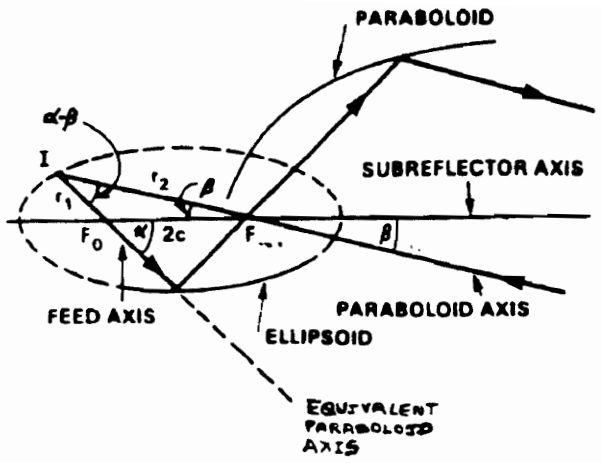

Figure 12.4. Geometry of ellipsoidal system. From [43].

one focus at infinity) and the parent subreflector surface. Most important, the ray path must be closed in order to ensure that (12.1) is satisfied. Figures 12.4 and 12.5 show configurations satisfying this geometrical condition [43]. Figure 12.4 employs an ellipsoidal subreflector and Fig. 12.5 employs a hyperboloidal one. Our analysis is limited to concave ellipsoids, convex hyperboloids, and concave paraboloids, since a focused system is desirable. Convex ellipsoids and concave hyperboloids, as well as spherical reflectors, are normally employed in reflector systems with more than two reflectors [34].

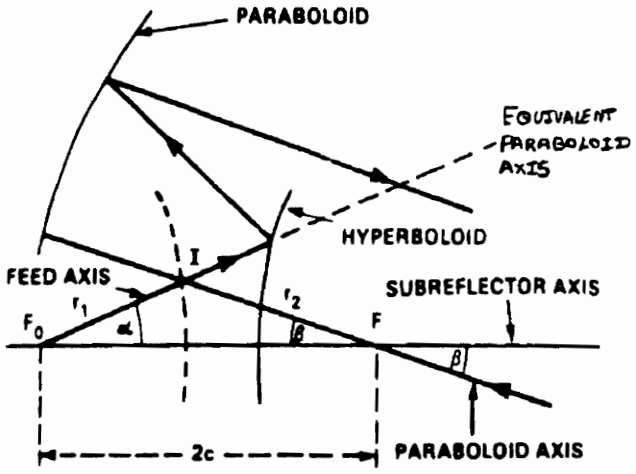

Figure 12.5. Geometry of hyperboloidal system. From [43].

12.5 Design Relations for XPOL Reduction

In this section we derive Dragone and Mizugutch conditions given below

$$\tan\frac{\alpha}{2} = \frac{1}{M}\tan\frac{\beta}{2} \qquad \text{(Dragone Condition)} \qquad (12.2)$$

$$\tan\alpha = \frac{(1-e^2)\sin\beta}{(1+e^2)\cos\beta - 2e} \qquad \text{(Mizugutch Condition)} \qquad (12.3)$$

We will show that both (12.2) and (12.3) express the same condition and therefore yield similar results. We start with the hyperboloidal system of Fig. 12.5. As addressed in the last section, the feed antenna axis is coincident with the equiva-

lent paraboloid axis when the reflected rays form a closed path with the ray coming from the feed antenna (located at F_0). This is a sufficient condition to minimize XPOL in the dual offset reflector system. When that condition is satisfied, parts of the rays form a triangle with vertexes at F_0, F, and I. Therefore, if we enforce the existence of this triangle, the reflector configuration presents optimum XPOL performance. The law of sines applied to the triangle $F_0 F I$ yields

$$\frac{\sin\alpha}{r_2} = \frac{\sin[\pi - (\alpha+\beta)]}{2c} = \frac{\sin\beta}{r_1} \tag{12.4}$$

where α is the feed pointing angle measured relative to the hyperboloidal subreflector axis of symmetry (F_0F), and β is the angle between the hyperboloid axis and the paraboloid axis of symmetry; see Fig. 12.5 for further details. In addition, the distances r_1 and r_2 are given by [43]

$$r_1 = \frac{(c/e)|e^2-1|}{e\cos\alpha + 1} \tag{12.5}$$

$$r_2 = \frac{(c/e)(e^2-1)}{e\cos\beta - 1} \tag{12.6}$$

where c is half of the interfocal distance, and e is the subreflector eccentricity ($e > 1$ for a hyperboloid and $0 < e < 1$ for an ellipsoid). The first equality of (12.4) yields

$$(2\,e\sin\alpha)(e\cos\beta - 1) = e^2\sin(\alpha+\beta) - \sin(\alpha+\beta) \tag{12.7}$$

which can be rewritten as

$$2\,e\sin\alpha - \sin(\alpha+\beta) - e^2\sin(\alpha-\beta) = 0 \tag{12.8}$$

where the following relation was used twice

$$\sin(\alpha \pm \beta) = \sin\alpha\cos\beta \pm \cos\alpha\sin\beta \tag{12.9}$$

Equation (12.8) can be straightforwardly transformed to

$$\tan\alpha = \frac{(1-e^2)\sin\beta}{(1+e^2)\cos\beta - 2e} \tag{12.10}$$

which is Mizugutch condition (12.3) [16]. Now, if we add and subtract $\sin(\alpha+\beta)$ from (12.8), we obtain

$$2\,e\sin\alpha - 2\sin\alpha\cos\beta - 2\cos\alpha\sin\beta - e^2\sin(\alpha-\beta) + \sin(\alpha+\beta) = 0 \tag{12.11}$$

which can be rewritten as

$$2\,e\sin\beta + \sin(\alpha+\beta) - e^2\sin(\alpha-\beta) = 0 \tag{12.12}$$

where we used the relation

$$e = \frac{\sin\alpha + \sin\beta}{\sin(\alpha - \beta)} \tag{12.13}$$

obtained from the equality of the first and last terms of (12.4); i.e., $r_1 \sin\alpha = r_2 \sin\beta$. It is interesting to note that (12.12) can also be derived from the second equality of (12.4). This is because any triangle is completely defined by two sides and two angles, and therefore (12.8), (12.12), and (12.13) represent the exact same condition, although in different mathematical forms. We now show that (12.2) is just a linear combination of (12.8) and (12.12). Adding (12.8) and (12.12) gives

$$\sin\alpha + \sin\beta - e\sin(\alpha - \beta) = 0 \tag{12.14}$$

And subtracting (12.8) and (12.12) yields

$$e[\sin\alpha - \sin\beta] - \sin(\alpha + \beta) = 0 \tag{12.15}$$

Finally, by taking the difference of (12.14) and (12.15) one arrives at

$$\tan\frac{\alpha}{2} = \frac{e+1}{e-1}\tan\frac{\beta}{2} \tag{12.16}$$

which is generally referred to as Dragone condition [34] and is in the format of (12.2). Note that the term $(e+1)/(e-1)$ is normally referred to as the subreflector magnification, M.

For the ellipsoidal system of Fig. 12.4, the same procedure employed for the hyperboloidal system yields the same set of equations. It is worth noting that in this

case, (12.10) and (12.16) yield negative values for α since for an ellipsoid $0 < e < 1$. However, this can be avoided if we define α as in Figs. 12.4 and 12.5. In that case, (12.10) and (12.16) are written as

$$\tan\alpha = \frac{|1-e^2|\sin\beta}{(1+e^2)\cos\beta - 2e} \tag{12.17}$$

and

$$\tan\frac{\alpha}{2} = \frac{e+1}{|e-1|}\tan\frac{\beta}{2} \tag{12.18}$$

where the absolute values were introduced to account for the different orientations of α in the ellipsoidal and hyperboloidal systems of Figs. 12.4 and 12.5. Equations (12.17) and (12.18) represent the same condition for XPOL minimization in dual offset reflector systems, and therefore yield similar results. Sometimes, (12.18) is preferable over (12.17), since it is more compact and allows the direct computation of β as a function of α.

We investigated the solutions of (12.17) and (12.18) for various values of the subreflector eccentricity e. In fact the results obtained from both equations were identical for angles in the first quadrant (i.e., $0 \leq \alpha, \beta \leq 90°$). This is an expected result since both equations contain a quadrant ambiguity. However, this does not represent a problem since angles outside the first quadrant have no practical meaning in our study configuration and can therefore be neglected. Figure 5.2 in Section 5.2 shows the behavior of α as a function of β for various values of e, such that (12.17) or (12.18) is satisfied (condition for XPOL minimization). Practical applications of (12.17) or (12.18) can be found throughout this dissertation.

VITA

Marco Antonio Brasil Terada was born in São Paulo, Brazil, on November 27, 1966. He received the B.S. and M.S. degrees in electrical engineering from the University of Brasília, Brazil, in 1989 and 1991, respectively, and the Ph.D. degree in electrical engineering from Virginia Polytechnic Institute and State University (Virginia Tech), Blacksburg, in 1995. Dr. Terada has been a consultant for industry and has authored or coauthored about 10 journal articles and symposium papers in the areas of wire and reflector antennas. His research interests include electromagnetic theory and applications, with special emphasis on antennas.

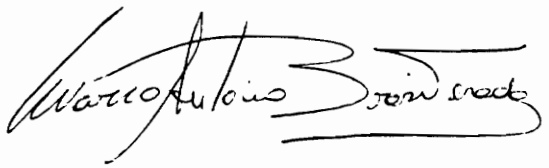

June 1995